Technische Universität München
Institut für Energietechnik

Lehrstuhl für Thermodynamik

Combustion Model for the Computation of Flame Propagation in Lean Hydrogen-Air Mixtures at Low Turbulence

Peter Katzy

Vollständiger Abdruck der von der Fakultät für Maschinenwesen der Technischen Universität München zur Erlangung des akademischen Grades eines

DOKTOR – INGENIEURS

genehmigten Dissertation.

Vorsitzender:
Prof. Dr.-Ing. Wolfgang A. Wall
Prüfer der Dissertation:
Prof. Dr.-Ing. Thomas Sattelmayer
Prof. Dr.-Ing. Marco K. Koch

Die Dissertation wurde am 26.08.2020 bei der Technischen Universität München eingereicht und durch die Fakultät für Maschinenwesen am 23.12.2020 angenommen.

Vorwort

Die vorliegende Arbeit entstand am Lehrstuhl für Thermodynamik der Technischen Universität München während meiner Tätigkeit als wissenschaftlicher Mitarbeiter. Sie wurde durch das Bundesministerium für Wirtschaft und Energie über die Gesellschaft für Anlagen- und Reaktorsicherheit gefördert.

Zu aller erst möchte ich Prof. Dr.-Ing. Thomas Sattelmayer für das Vertrauen der letzten Jahre und die gewährten Freiheiten bei der Bearbeitung des Projekts danken. Bei Prof. Dr.-Ing. Marco K. Koch bedanke ich mich für die Übernahme des Koreferats und aller damit verbundenen Pflichten und Prof. Dr.-Ing. Wolfgang A. Wall danke ich für die freundliche Übernahme des Prüfungsvorsitzes.

Ich möchte ich mich bei allen ehemaligen Kollegen und Vorgängern für die hilfreichen Tipps und Hinweise während der letzten Jahre bedanken. Insbesondere möchte ich mich jedoch bei Dr.-Ing. Josef Haßlberger für die vielen Diskussionen, Anregungen, Verbesserungsvorschläge und vor allem für die immer kritischen Paperkorrekturen bedanken.

Nach zwei zerstörten Festplatten und dem mittlerweile dritten PC muss ich auch den ehemaligen und aktuellen Admins des Lehrstuhls danken. Sie haben meine IT Probleme unermüdlich und vorallem immer erfolgreich gelöst. Der mechanischen und der elektrischen Werkstatt danke ich für die stets angenehme Zusammenarbeit und die eine oder andere kreative Problemlösung. Ebenso möchte ich mich bei Helga Bassett und Sigrid Schulz-Reichwald für die immer freundliche Hilfe in administrativen Angelegenheiten bedanken.

Meinen ehemaligen Studenten gebührt besonderer Dank, denn ohne sie wäre diese Arbeit nicht möglich gewesen. Dafür möchte ich mich bei allen meinen ehemaligen Studenten bedanken. Besonders hervorheben möchte ich Pascal Druck und Andreas Ewald. Beide haben mit unermüdlichem Einsatz, eigenen Ideen und vor allem Kreativität, numerische und experimentelle Arbeiten erfolgreich durchgeführt und einen großen Beitrag zum Erfolg der Arbeit beigetragen.

Bei meinen Eltern möchte ich mich für die Unterstützung während meiner gesamten Ausbildungszeit und das immer dagewesene Vertrauen bedanken. Meiner Schwester Dr. Elisabeth Katzy danke ich für die Inspiration während meiner gesamten Schul- und Studienzeit. Es war deine Inspiration die mich schlussendlich hierher geführt hat.

Finally, I would like to thank you, Becca, for your love and unconditional support. With your help and positivity by my side everything seems possible. I dedicate this work to you and to our daughters, Olivia and Emilia, which remind us everyday what is truly important.

München, im Januar 2021

Peter Katzy

Kurzfassung

In dieser Arbeit wird eine neue Modellierungsstrategie für Simulationen von mageren Wasserstoff-Luft-Gemischen entwickelt und validiert. Ziel ist die Entwicklung einer neuen semi-empirischen Korrelation, die die experimentell beobachtete Flammenbeschleunigung unter Berücksichtigung der identifizierten Einflussfaktoren reproduziert. Basierend auf Experimenten, bei denen optische und konventionelle Messtechniken zum Einsatz kamen, soll die Flammenausbreitung in der Anfangsphase qualitativ und quantitativ evaluiert werden. Zusätzlich ergänzt die Auswertung von hochaufgelösten Simulationen den experimentellen Datensatz.

Bei Kühlmittelverlustszenarien (engl.: LOCA) in Kernkraftwerken kann die Reaktion der Zirkonium-Brennstabhülle mit dem umgebenden Wasser zur Freisetzung großer Mengen Wasserstoff führen. Aufgrund der weiten Zünd- und Explosionsgrenzen von Wasserstoff-Luft-Gemischen ist die Bildung einer zündfähigen Gemischwolke möglich. Die numerische Modellierung der Flammenausbreitung in solchen Szenarien ist für magere Wasserstoff-Luft-Gemische besonders anspruchsvoll und für deterministische Sicherheitsanalysen bisher nicht ausreichend fortgeschritten.

Insbesondere in der frühen Phase der Flammenausbreitung in vorgemischten mageren Wasserstoff-Luft-Gemischen können beschleunigende Effekte wie Flammenfrontinstabilitäten auftreten. Diese Effekte können auf den Rechengittern, die in URANS-Simulationen (Unsteady Reynolds-Averaged Navier-Stokes) verwendet werden, aufgrund unzureichender Rechenleistung nicht aufgelöst werden. Diese Instabilitätseffekte müssen modelliert werden, da sonst die Ausbreitungsgeschwindigkeit der Flammenfront und die damit verbundenen Drucklasten systematisch unterschätzt werden.

Die kleinskalige Faltung der Flammenfront aufgrund intrinsischer Instabilitäten geht mit einer Vergrößerung der Flammenfläche einher. Mit zunehmendem Druck nimmt die charakteristische Skala der lokalen Flammenfaltung ab, während die Flammenfrontfläche selbst zunimmt.

Lokal ist die Flammenfront zum Frischgas hin konvex gekrümmt, was zu einer erhöhten laminaren Brenngeschwindigkeit in diesen Zonen der Flammenfront führt. Aufgrund der für diese Arbeit gewählten mathematischen Struktur der neuen Formulierung ist eine realistische Vorhersage der Brenngeschwindigkeit auch im Fall des Nichtvorhandenseins eines einzelnen Effekts gewährleistet. Die Validierung des neuen Modellierungskonzepts in dieser Arbeit basiert auf experimentellen Daten des Autors und auf bereits vorhandenen Daten aus einschlägiger Literatur.

Abstract

In this thesis a new modeling strategy for simulations of lean hydrogen-air mixtures is developed and validated. The goal is the development of a new semi-empirical correlation, reproducing the experimentally observed flame acceleration under consideration of the identified influencing factors. Based on experiments, which utilized optical and conventional measurement techniques, the flame propagation in the initial phase will be evaluated qualitatively and quantitatively. Additionally, the evaluation of highly-resolved simulations supplements the experimental data.

During loss of coolant accident (LOCA) scenarios in nuclear power plants, the reaction of the zirconium fuel rod cladding with the surrounding water can lead to the release of large amounts of hydrogen. Due to the wide ignition and explosion limits of hydrogen-air mixtures, the formation of an ignitable mixture cloud is possible. The numerical modeling of flame propagation in such scenarios is particularly challenging for lean hydrogen-air mixtures and so far, not sufficiently advanced for deterministic safety analyses.

Especially in the early phase of flame propagation in premixed lean hydrogen-air mixtures, accelerating effects such as flame front instabilities can occur. These effects cannot be resolved on the computational grids used in URANS-simulations (Unsteady Reynolds-Averaged Navier-Stokes) due to insufficient computational power. These instability effects must be modeled, otherwise the propagation velocity of the combustion wave and the associated pressure loads are systematically underestimated.

Small-scale flame front wrinkling due to intrinsic instabilities is accompanied by an increase in flame area. With increasing pressure, the scale of the cellular structure decreases while the flame front area itself increases. Locally, the flame front is convex towards the fresh gas, which leads to an increased laminar burning velocity in these zones of the flame front. Due to the mathematical structure of the new formulation selected for this thesis, a realistic prediction of the burning velocity is ensured even

in the absence of a single effect. The validation of the new modeling concept in this thesis is based on experimental data of the author and on pre-existing data from relevant literature.

Contents

List of Figures

List of Tables

Nomenclature

Latin letters

A	Area, m^2
a	Thermal diffusivity, m^2/s
c	Polynomial coefficient
$\tilde{c}$	Favre averaged reaction progress variable, 0...1
c_p	Specific heat capacity at constant pressure, J/(kg K)
d_h	Hydraulic diameter, m
D	Diameter, m
D	Diffusion coefficient, m^2/s
E	Global activation energy, kcal/mol
k	Specific turbulent kinetic energy, m^2/s^2
K	Karlovitz stretch factor, 1/s
l	Length, m
l_t	Integral turbulent length scale, m
L	Length, m
$\mathscr{L}$	Markstein length, m
n	Number
n_{oxidzer}	Moles of fuel
n_{fuel}	Moles of oxidizer
p	Pressure, bar
P	Perimeter, m
R	Specific gas constant, J/(kg K)
R_0	Ideal gas constant, $R_0 = 8.3144598$ J/(molK)
r	Radius, m
s	Burning velocity, m/s
s	Cell parameter, 0...1

s	Flame front parameter
T	Temperature, K
t	Time, s
t	Cell parameter, 0...1
t_{wait}	Waiting time after injection, s
u_F	Flame speed in a stationary reference system, m/s
u	Velocity, m/s
X	Mole fraction
Y	Mass fraction

Greek letters

α	Temperature dependency coefficient
β	Pressure dependency coefficient
σ	Density ratio of burned and unburned gases
δ	Flame thickness, m
ρ	Density, kg/m^3
Ξ	Wrinkling factor
ν	Kinematic viscosity, m^2/s
κ	Geometrical curvature, 1/m
λ	Thermal diffusivity, m^2/s
μ	Dynamic viscosity, kg/(ms)
μ_t	Eddy viscosity, kg/(ms)
∇	Nabla operator
Φ	Equivalence ratio
ϕ	General variable
$\dot{\omega}_c$	Source term of transport equation for $\tilde{c}$, kg/(m^{3}s)
η	Kolmogorov length scale, m
τ	Time scale, s

Superscripts

$(\bullet)^{+}$	Positive value
$(\bullet)^{0}$	Initial value
$(\bullet)'$	Fluctuating value (Reynolds)
$(\bullet)''$	Fluctuating value (Favre)
$\widetilde{(\bullet)}$	Favre averaged
$\dot{(\bullet)}$	First derivative
$\ddot{(\bullet)}$	Second derivative
$\overrightarrow{(\bullet)}$	Vector

Subscripts

2D	Two dimensional
3D	Three dimensional
ad	Adiabatic
b	Burned
B	Blint
c	Curvature
c	Reaction progress variable
cr	Critical
cross	Cross-sectional
d	Displacement
D	Deficient species
Δ	Grid
E	Excessive species
eff	Effective
F	Flame
gas	Gas property
H_2	Hydrogen
inj	Injection
l	Laminar
k	Species
LD	Landau-Darrieus

l,0	Laminar and unstretched
l,s	Laminar and stretched
m	Mean value
max	Maximum value
η	Kolmogorov
p	Pressure
R	Reaction zone
ref	Reference
s	Strain
smooth	Smooth
sp	Spherical
st	Stoichiometric
t	Turbulent
T	Temperature
TD	Thermal-diffusive
theo	Theoretical
u	Unburned
wrink	Wrinkled
Z	Zeldovich
$\perp$	Perpendicular
$\parallel$	Parallel

Dimensionless Numbers

Ka	Karlovitz number
Le	Lewis number
Ma	Markstein number
Pe	Peclet number
Re	Reynolds number
Sc	Schmidt number
Ze	Zeldovich number

Abbreviations

$AICC$	Adiabatic Isochoric Complete Combustion
BWR	Boiling Water Reactor
CFD	Computational Fluid Dynamics
CJ	Chapman-Jouguet
$CMOS$	Complementary metal oxide semiconductor
DDT	Deflagration-to-Detonation Transition
DR	Dimension Ratio
DNS	Direct Numerical Simulation
exp	Experimental
LES	Large Eddy Simulations
LD	Landau-Darrieus
$LOCA$	Loss of Coolant Accident
$MCCI$	Molten Core Concrete Interaction
$PLIF$	Planar Laser-induced Fluorescence
PDF	Probability Density Function
$PISO$	Pressure-Implicit with Splitting of Operators
PWR	Pressurized Water Reactor
SHG	Second Harmonics Generator
sim	Simulational
$SIMPLE$	Semi-Implicit Method for Pressure Linked Equations
SST	Shear Stress Transport
sym	Symmetry
TFC	Turbulent Flame Speed Closure
TD	Thermal-diffusive
$URANS$	Unsteady Reynolds-Averaged Navier-Stokes
UV	Ultra-violet

1 Introduction

1.1 Motivation and problem description

At the end of 2018, 450 nuclear reactors were in operation around the world providing a total electrical power of 396.4 GW [55]. The International Atomic Energy Agency assumes that by 2030 the power capacity provided by nuclear power plants could increase by 30% and even double by 2050 [55]. Globally, 89% of the electricity generated by nuclear power plants is generated by light-water reactors, with water acting as coolant and moderator. Examples of this design are Pressurized Water Reactors (PWR) and Boiling Water Reactors (BWR) which are the most common types of nuclear power plant design based on the number of reactors that exist today. By the end of 2018, 66% of the 450 reactors have been in service longer than 30 years.

Loss of coolant accidents (LOCA) in nuclear power plants of the PWR and BWR type can be accompanied by the production of large amounts of hydrogen. Compared to gaseous hydrocarbons, hydrogen exhibits significant differences in some of the critical safety relevant physical and chemical properties [20]. Wider flammability limits and by an order of magnitude lower ignition energy indicate the high potential of a hydrogen-air mixture to ignite after an accidental release. The higher specific heat of combustion of hydrogen leads to an increased amount of released energy during the combustion process. This leads to higher temperatures and pressure loads during accident scenarios. Additionally, hydrogen exhibits a higher sensitivity for a deflagration-to-detonation transition (DDT) compared to hydrocarbons.

The release of hydrogen in accident scenarios can follow different production mechanisms. During the In-Vessel phase of an accident where the integrity of the reactor's containment is not yet compromised, the

reaction of water vapor with zirconium, which is used in the fuel rod cladding is most likely to occur. The temperature in the containment can rise above 900°C and the zircalloy of the fuel rods reacts with the surrounding water according to the following global reaction [36]:

$$Zr + 2\,H_2O \longrightarrow ZrO_2 + 2H_2 \tag{1.1}$$

If the temperatures in the containment are further increasing and eventually rising above approximately 1000°C the chrome and the iron of the containment begin to oxidize and produce additional amounts of hydrogen:

$$2\,Cr + 3\,H_2O \longrightarrow Cr_2O_3 + 3H_2 \tag{1.2}$$

$$3\,Fe + 4\,H_2O \longrightarrow Fe_3O_4 + 4H_2 \tag{1.3}$$

Eventually, the containment can lose its integrity and a leak can occur. This phase is referred to as the Ex-Vessel phase. The molten core starts to interact with the concrete below the containment. This Molten-Corium-Concrete Interaction (MCCI) leads to additional production of carbon monoxide and additional amounts of hydrogen. During both phases (In- and Ex-Vessel) several hundred kilograms of hydrogen can be produced and pose an imminent risk of a severe accident if the hydrogen mixes with the oxygen containing atmosphere of the plant forming a combustible mixture cloud [43].

The Fukushima-Daiichi accident in 2011 is the most recent example of devastating consequences that can result from a hydrogen release during an upset and the unintentional ignition of the combustible mixture [101]. This demonstrates the importance of gaining knowledge about governing processes leading to an accident in such complex facilities. Experiments investigating flame acceleration processes are not feasible in such complex and hazardous environments such as a nuclear reactor containment and so are typically conducted on smaller scales. Regardless of the small scale, the results are critical because they are used as the basis for

Computational Fluid Dynamics (CFD) modeling. The numerical investigation and simulation of the processes that occur during an accident scenario represent a safe and efficient method to assess safety concepts and develop mitigation measures.

Due to limited computational power, direct numerical simulations (DNS) are not feasible in the foreseeable future for safety analyses on large scales. Instead, the less computationally expensive (Unsteady) Reynolds-Averaged Navier-Stokes simulations (URANS) are the state-of-the-art approach used by the industry for large-scale applications. The quality of the results obtained with this approach depends mostly on the quality of the implemented models in the CFD code.

1.2 Goal of this work

In the early stage of flame propagation, assuming the turbulence level is low, the main driver for flame acceleration is enlargement of the flame surface area. This enlargement can be traced back to the macroscopic enlargement of the flame surface due to flame propagation and additionally in lean hydrogen-air mixtures to small-scale flame front wrinkling caused by flame front instabilities. These instabilities are primarily the hydrodynamic or Landau-Darrieus instability [68] and the thermal-diffusive instability [74].

In Fig. 1.1 the effect of small-scale flame front wrinkling due to instabilities is visualized. Shadowgraphy recordings showing the second spatial derivative of the density of a lean (13 %) and a nearly stoichiometric (30 %) hydrogen-air flames are compared with each other. Both images are obtained through the GraVent test facility that was used throughout this work. In both cases a homogeneous mixture with negligible initial turbulence is ignited by a spark plug at the left border of the picture. After ignition, the flame front propagates hemispherically until it reaches the channel top and bottom walls. Finally, the flame front propagates from left to right through the channel, passing the optically accessible area of the GraVent facility.

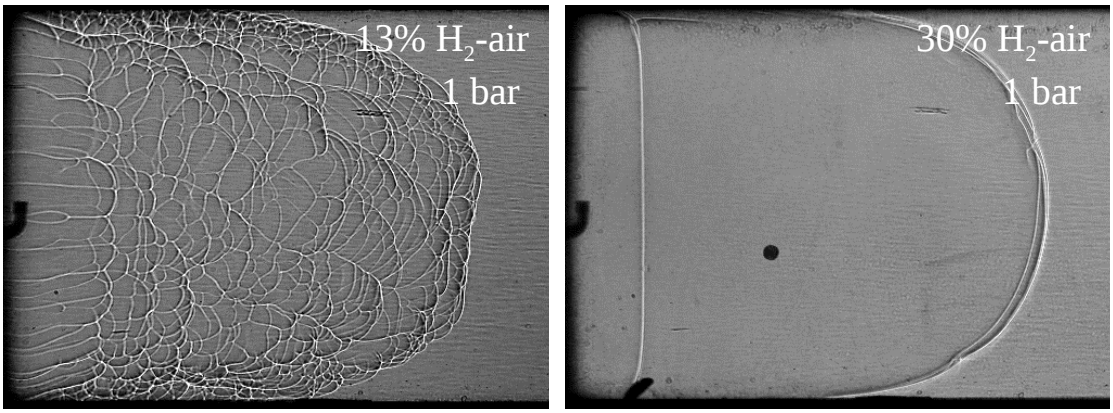

Figure 1.1: Shadowgraphy images of hydrogen-air flames at an initial pressure level of 1 bar with different stoichiometries propagating from left to right in the GraVent facility. Left: flame front with cellular structure due to instability mechanisms; right: smooth flame front.

Unsteady flame propagation of hydrogen-air flames has been investigated extensively in the past. Gostintsev et al. [47] experimentally investigated self-similar propagation of freely propagating unconfined flames of several fuel types on large-scale. A power law dependence of the observed flame front velocity and the flame radius was formulated. Molkov et al. [83] and Tolias et al. [105] investigated large-scale hydrogen-air deflagrations with Large Eddy Simulations (LES). Stoichiometric mixtures at an ambient initial pressure level were investigated numerically. The combustion modeling used in this work was based on Yakhot's equation for premixed turbulent combustion [116]. The authors extended the original formulation by the additional accelerating effects in the investigated case. Tolias et al. [104] investigated flame propagation of near stoichiometric hydrogen-air flames in a large-scale tunnel, comparing an empty with an obstructed tunnel. Experimental investigations of propagating flame fronts were also extensively conducted by Bauwens et al. [6]. Based on the fractal concept of Gostintsev et al. [47] a new fractal exponent has been evaluated for propagating lean hydrogen-air flames.

The approach in this project is to better understand the flame wrinkling processes utilizing an entirely closed small-scale explosion chan-

nel with optical accessibility in the initial phase of flame propagation. Since such small-scale effects as shown in Fig. 1.1 cannot be resolved on coarse grids used in URANS simulations, the present work aims to isolate the effect of flame front instabilities on flame velocity from experimental data and formulate a subgrid-model for CFD simulations including this effect. For this purpose, highly time-resolved optical measurement techniques are employed to qualitatively and quantitatively investigate the occurring flame acceleration mechanisms. Additionally, the experiments are supported by highly resolved simulations. The focus in this project is the investigation of the initial phase of flame propagation of quasi-laminar lean hydrogen-air flames at atmospheric pressure. Based on the results of the experiments and the highly resolved simulations a new URANS modeling concept for hydrogen-air combustion simulations is developed and validated with experimental data. Even though the focus of the work is on flames in initially quasi-laminar mixtures, the influence of turbulence on flame propagation must be included in the model. This way the applicability range of the model can be extended significantly. The developed new modeling concept is based on an algebraic equation incorporating experimental results following the approach of Turbulent Flame Speed Closure (TFC) [118].

1.3 Thesis outline

Now that the motivation for this thesis and the description of the problem has been described, this thesis continues with an introduction of basic principles of premixed hydrogen-air combustion in Ch. 2 where only the relevant basics in the context of unsteady lean flames are discussed. In Ch. 3.1 the test facility and the applied conventional and optical measurement techniques are presented. The experimental data is used for model development and model validation, respectively. Additionally, highly resolved two-dimensional simulations are conducted to support the experimental investigations and are presented in Ch. 4. After the data basis for model development is established in the two previous chapters, Ch. 5 discusses the data evaluation strategy utilized for the experimental and numerical raw data. Based on the findings in the eval-

uated experimental and numerical data, the newly developed modeling concept is introduced and discussed in Ch. 6. The identified accelerating effects are incorporated in the model formulation. After this, Ch. 7 compares results of simulations utilizing the developed model with experimentally obtained validation data. Finally, Ch. 8 summarizes the results of this work.

2 Fundamentals

Two extreme scenarios of flame configurations can be defined based on the temporal order of the processes of mixing and reaction. In non-premixed flames mixing and reaction occur simultaneously, whereas in premixed flames mixing is completed before the reaction. Furthermore, partially premixed flames can be seen as a blend between these two extreme scenarios, exhibiting both types of flames locally. Non-premixed combustion is the basis of diesel engines or conventional gas turbines. The combustion process takes place in the vicinity of the stoichiometric zone where the reactivity exhibits highest values. This leads to high combustion temperatures and therefore to high emissivity levels and has potential to form soot.

In contrast to non-premixed flames, premixed flames exhibit more possibilities to customize the combustion process. The stoichiometry at which the combustion process takes place can be adjusted to the desired fuel-to-air ratio. The non-dimensional and mixture independent equivalence ratio can be defined, indicating lean ($\Phi < 1$), stoichiometric ($\Phi = 1$) or rich ($\Phi > 1$) combustion:

$$\Phi = \frac{n_{\text{fuel}} / n_{\text{oxidizer}}}{(n_{\text{fuel}} / n_{\text{oxidizer}})_{\text{st}}} \tag{2.1}$$

In premixed flames the mixing process of the fuel and the oxidizer is completed prior to combustion and therefore entirely decoupled from it. Premixed flames occur e.g. in spark-ignited internal combustion engines. Gas and air are mixed before the mixture is routed to the combustion chamber where it is ignited by a spark plug.

By adjusting the combustion process to the desired stoichiometry or equivalence ratio, combustion temperatures and therefore emissions can be controlled. The prevention of soot formation can be ensured

by excessive air in the combustion process (i.e. in the lean regime). However, premixed flames are more susceptible to accidents than non-premixed flames. The presence of the combustible mixture poses a serious hazard because it can ignite unintentionally. In accidental explosions a combustible mixture is formed and most likely ignited by an electrical spark or, for example, a hot surface. In this initial stage the propagating flame front is of laminar nature but can undergo significant acceleration under certain conditions. This acceleration is accompanied by increasing pressure leading to serious damage of equipment or the environment [109]. Premixed flames can also exhibit mixture inhomogeneities which can lead to considerable changes in the flame propagation behavior, as investigated through Boeck [11] and Hasslberger [51]. Additionally, premixed flames are prone to flame instabilities which can lead to flame acceleration.

Since premixed combustion can occur at different stoichiometries, premixed flames exhibit varying burning velocities and flame thicknesses and a sensitivity to stretch and flame instabilities with varying fuel concentrations. These characteristics are discussed in the subsequent sections.

2.1 Flame acceleration behavior

Premixed flames can accelerate. The processes responsible for flame acceleration are highly dependent on the initial and boundary conditions of the investigated problem. Initial conditions that influence the acceleration behavior are pressure, temperature or the initial turbulence level. Boundary conditions like congestion, mixture inhomogenity, the degree of confinement or the presence of turbulence generating obstacles are major influencers of flame acceleration behavior. Overviews of the governing processes of flame acceleration in accidental scenarios can be found in Ciccarelli and Dorofeev [25], Dorofeev [32], Breitung et al. [21] or in the report of the Nuclear Energy Agency [1].

Based on the processes responsible for acceleration, the flame acceleration process can be divided into different stages. Fig. 2.1 shows subse-

quent processes, that can occur in an accident scenario. The first step is the formation of a combustible mixture cloud.

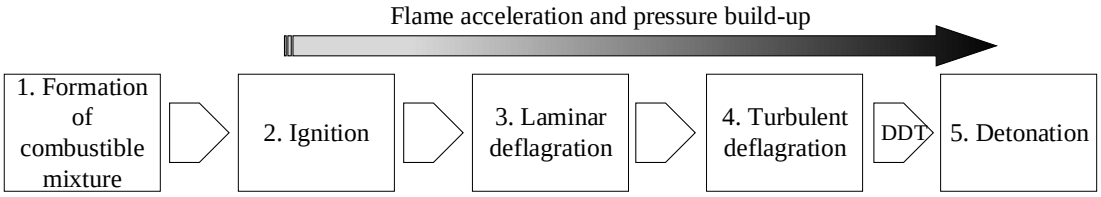

Figure 2.1: Possible propagation stages of an accelerating flame front.

The formation of a flammable mixture cloud in accident scenarios is highly probable because of the wide ignition limits of hydrogen-air mixtures. Usually an ignition of the mixture can occur within the concentration range of 4 - 76%. These limits depend on the direction of flame propagation. Additionally, hydrogen exhibits high diffusivity and high burning velocity compared to hydrocarbons [44]. The ignition energy for the most ignitable mixture is one magnitude lower than for hydrocarbons. This leads to the assumption that the flammable mixture is very likely to ignite. Possible ignition sources like hot surfaces or sparks at electrical installations are typically assumed in safety analyses. These ignition mechanisms are weak ignitions where the flame front initially propagates in the deflagrative regime. A strong ignition leads to a flame propagation in the detonative regime immediately and requires a high energy input, e.g. initiated through a solid explosive material or a laser. This high energy input leads to formation of a shock wave which is strong enough to initiate auto ignition. However, the case of a strong ignition is not probable in the scenarios investigated in the present work, which is why mild ignition is always assumed.

After ignition, the flame propagates as a laminar deflagration wave away from the ignition position. A laminar deflagration can be seen as an exothermic reaction propagating at subsonic velocity into the unburned mixture. At this initial stage flame propagation is dominated by diffusive heat and mass transport processes. Heat is transported from the hot combustion products to the cold, fresh gas. Reactants are consumed, leading to a lower concentration of reactants in the reaction zone. The concentration gradient across the flame zone leads to mass transfer of re-

actants to the reaction zone. The macroscopic flame area growth results in an increase of the overall reaction rate, which leads to higher flame velocities. The propagation speed for an external observer does not exceed the speed of sound of the reactants and the developing overpressure is in the range of zero to approximately 1 bar. Since the expanding flame front is intrinsically unstable, flame front instabilities like the Landau-Darrieus [68] and the thermal-diffusive instability [74] can occur in this stage and increase the flame surface area locally and further enhance the burning velocity. Stretch effects can have significant influence on the acceleration process and can especially accelerate mixtures with negative Markstein lengths and simultaneously positive stretch rates. Additionally, acoustic instabilities can occur in explosions in closed vessels and enhance flame surface enlargement and further accelerate the flame front.

If the flame is further accelerating the propagation velocity exceeds the speed of sound of the reactants and can reach the speed of sound of the products of up to 1000 m/s. The overpressure in this regime can reach values up to 10 bar [11]. In this stage the governing effects are of turbulent nature. Turbulent heat and mass transport processes are faster than laminar processes, which is why the flame propagates at a higher velocity. Additionally, the turbulence itself is increasing the flame surface area and therefore the burning velocity. Turbulence is generated through the propagating flame front itself by accelerating the unburned gases ahead of the flame towards obstacles or in unobstructed channels in the wall boundary layer. The developing shear layer behind obstacles creates a significant amount of turbulence in the fresh gases ahead of the flame. In addition to turbulence, powerful instability mechanisms like the Kelvin-Helmholtz, Rayleigh-Taylor or Richtmeyer-Meshkov instabilities can occur and increase flame surface area and further accelerate the flame.

Following the turbulent deflagration regime, transition to a detonative propagation regime can occur. The fundamentals of DDT and detonations are only briefly addressed since these processes are not in the focus of the present work. Strong flame acceleration is necessary for the transition from the deflagrative to the detonative regime. Based on the empiric correlation in Eq. 2.2, the mixture must exhibit a certain density ratio σ

across the flame front:

$$\sigma = \frac{\rho_u}{\rho_b} > \sigma_{cr} \tag{2.2}$$

For hydrogen-air flames at atmospheric pressures, the critical value is $\sigma_{cr} = 3.75$ according to [34].

This formulation neglects mixture inhomogenities or partially confined flames. Kuznetsov et al. [66] and Friedrich et al. [41] suggest a modified expression for the critical expansion ratio σ_{cr} with facility specific constants. The second required criterion for a possible DDT is depicted in Eq. 2.3. The characteristic geometric length scale L of the facility must be at least seven times greater than the detonation cell width λ [33]:

$$L = 7\lambda \tag{2.3}$$

In order to account for mixture inhomogenities and partial confinement Kuznetsov et al. [66] and Friedrich et al. [41] suggest a modified criterion.

When both requirements are fulfilled DDT can be triggered through different mechanisms. According to Klein et al. [62] two trigger mechanisms can be identified on a macroscopic level. The first mechanism, also referred to as "mode A", is based on shock reflection on walls or shock focusing in edges of the facility. The second mechanism or "mode B" is the result of shock-flame interactions, local explosions of unburned mixture pockets enclosed in the burned mixture or shock-boundary layer interactions. The transition from the deflagrative to the detonative regime is characterized by a sudden jump of the propagation velocity.

The flame propagation in the detonation regime is governed by three-dimensional gas-dynamical processes. Longitudinal and transversal shocks interact with each other and precondition the unburned mixture. Due to the preconditioning, the reaction zone is coupled with the leading pressure wave. Auto-ignition occurs due to the significantly shortened auto-ignition times because of the elevated pressure level behind the leading shock wave. A stable detonation travels with what is known as the Chapman-Jouguet velocity (CJ) [23] [56] and can reach up to 2000

m/s in hydrogen-air mixtures. The pressure can significantly exceed 10 bar. A detailed discussion of the governing processes can be found in Lee [70].

The focus of the present work is the investigation of the early acceleration after ignition. The following sections focus on the involved processes and their characteristics observed in the experimental test facility.

2.2 Laminar deflagrations in premixed H_2-air flames

A hydrogen-air flame is characterized by multi-species chemistry with many intermediate steps [57]. Intermediate species are formed and consumed throughout the reaction process. The reaction of hydrogen and oxygen can be expressed utilizing 8 species and 38 intermediate reactions [111], leading to a very complex mechanism. An often-made simplification is the stoichiometric one-step overall reaction of hydrogen and oxygen. It can be formulated as follows:

$$2H_2 + O_2 \rightarrow 2H_2O + \text{Energy} \tag{2.4}$$

The stoichiometric mixture is at 29.6% of hydrogen in air and the visible light during reaction corresponds to the radiation of water steam at approximately 585 nm. The hydroxyl radical (OH) which only appears as an intermediate species during the reaction, emits light at a wavelength of approximately 307 nm. Later in this work, this characteristic of hydrogen flames will be used to visualize the small-scale flame wrinkling process.

Laminar combustion plays a secondary role in industrial applications and accidental investigations. Due to relatively slow flame propagation and the resulting low pressure rise, the consequences of solely laminar flame propagations are not critical in most of the cases. However, the significance is located in the use of laminar flames as the basis for turbulent modeling. Laminar flames are the basis of many (turbulent) combustion models where, for example, the chemical timescale is significantly faster than the turbulence timescale [76]. This assumption results in a model of the turbulent flame surface composed of laminar flame elements, called

flamelets. This way the chemistry and the turbulence processes are decoupled and can be calculated separately from each other.

2.2.1 Laminar burning velocity

The unstretched laminar burning velocity is a characteristic intrinsic quantity of premixed flames. A possibility to determine this quantity is an analytical approach, where the laminar burning velocity is calculated from chemical and thermodynamic properties [89]. Another approach is based on one-dimensional calculations of flames with a chemical-kinetics software such as CANTERA [46]. Here, the laminar burning velocity is determined as the inlet flow velocity of fresh gases occurring in the final stationary solution. The quality of the solution in this approach is primarily based on the chemical reaction mechanism used. Many reaction mechanisms for hydrogen-air combustion can be found in literature, such as Konnov [65], Kathrotia et al. [57] or Ó Conaire et al. [84]. An overview and analysis of certain mechanisms is summarized in Olm et al. [85]. However, especially in the lean stoichiometry range below 20% of hydrogen in air, discrepancies occur in burning velocities calculated with one-dimensional chemical-kinetics programs.

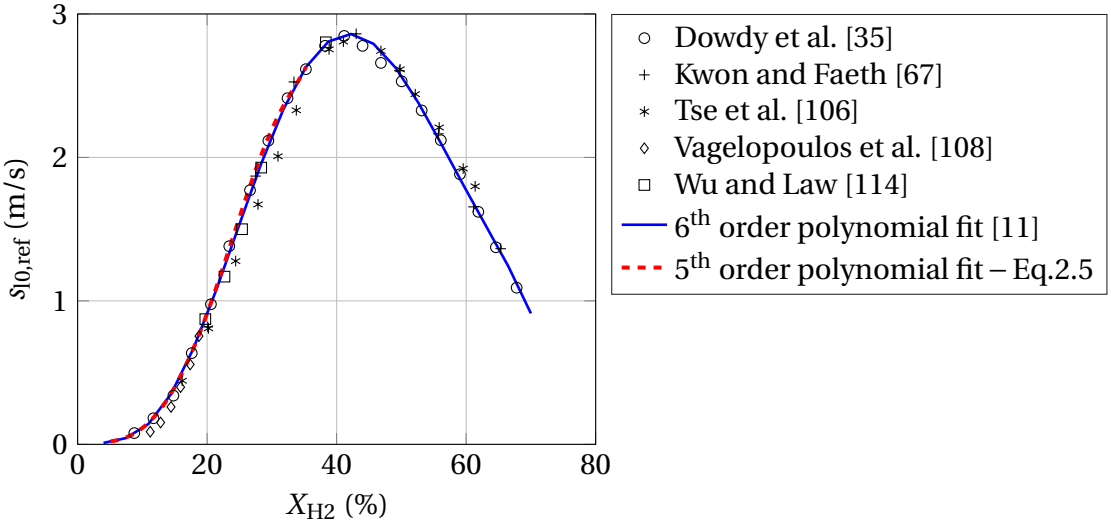

Figure 2.2: Experimentally determined unstretched laminar burning velocities for varying hydrogen mole fraction at reference conditions. Additionally, two fits are plotted.

To overcome this shortcoming and uncertainty of the aforementioned approach, the unstretched laminar burning velocity at reference conditions $s_{l,0,ref}$ is determined based on experimental data. Fig. 2.2 summarizes experimentally determined burning velocities at reference conditions reported by multiple authors. A 5^{th}-order polynomial fit is plotted in 2.2 and is defined as a function of the equivalence ratio[1]:

$$s_{l,0,ref} = \left[c_5\Phi^5 + c_4\Phi^4 + c_3\Phi^3 + c_2\Phi^2 + c_1\Phi + c_0\right] \mathrm{m/s} \tag{2.5}$$

with polynomial coefficients shown in Tab. 2.1:

Table 2.1: Coefficients for Eq. 2.5

c_5	c_4	c_3	c_2	c_1	c_0
4.248	-13.6	12.34	-0.833	-0.02239	-0.003956

Eq. 2.5 covers the lean range of hydrogen-air combustion and is valid in the range of Φ =0.1 to Φ =1.28 which corresponds to approximately 4% to 35%. A greater range is not necessary and is out of scope for this work. The polynomial fit in Eq. 2.5 is the basis of the developed modeling concept and will be used throughout this work. A 5^{th}-order polynomial fit is used because of the software requirements. The 6^{th}-order polynomial fit is depicted to show continuity in the formulation of the laminar burning velocity with previous projects. The laminar burning velocities modeled by Eq. 2.5 are determined for reference conditions (T_{ref} =293 K and p_{ref} =1 bar). In order to use the defined correlation for other thermodynamic conditions than the reference conditions, the following extension can be formulated, following Metghalchi and Keck [82]:

$$s_{l,0} = s_{l,0,ref}\left(\frac{T_u}{T_{ref}}\right)^{\alpha}\left(\frac{p}{p_{ref}}\right)^{\beta} \tag{2.6}$$

The exponentials α and β can be determined as a function of stoichiometry, according to Gelfand et al. [44].

[1] Throughout this work all polynomial fits are formulated as a function of the equivalence ratio due to input requirements of the used software

2.2.2 Laminar flame thickness

Figure 2.3 compares different flame thickness definitions in the range of lean to stoichiometric mixtures. Within this range the flame thickness is generally decreasing with increasing equivalence ratio.

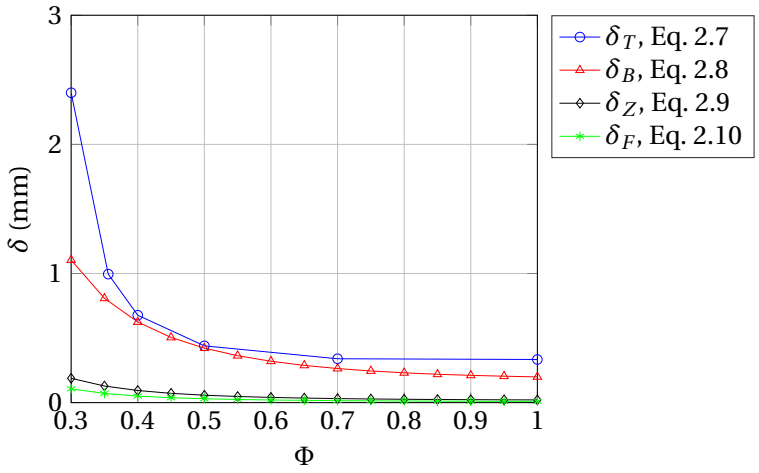

Figure 2.3: Comparison of flame thickness definitions under varying hydrogen concentration.

Formulations based on the temperature profile (Eq. 2.7 and Eq. 2.8) exhibit higher flame thickness values than formulations based on thermal diffusivity (Eq. 2.9) or kinematic viscosity (2.10). These discrepancies originate most likely from the different implied assumptions, like the $Le = 1$ assumption in Eq. 2.9 and Eq. 2.10.

Flame thickness formulation based on the temperature profile assumes a linear temperature increase and reads as follows [89] [107]:

$$\delta_T = \frac{T_b - T_u}{\max(\frac{dT}{dx})} \tag{2.7}$$

The flame thickness according to this formulation is calculated with a one-dimensional chemical-kinetics program [46]. It can be seen in Fig. 2.3 that this definition predicts the largest flame thickness. Following Poinsot and Veynante [89], the flame thickness according to Blint [10],

$$\delta_B = 2\,\delta_Z \left(\frac{T_b}{T_u}\right)^{0.7} \tag{2.8}$$

is known for its useful a-priori predictions. This formulation is able to reproduce the flame thickness δ_T, which is based on the temperature gradient, without calculating the temperature profiles. Variable δ_Z denotes the Zeldovich or diffusion thickness, comparing the thermal diffusivity of the unburned mixture a_u with the laminar burning velocity s_l. This definition underestimates the actual flame thickness by a factor of 5 [89] which can be observed over a wide range of stoichiometries in Fig. 2.3.

$$\delta_Z = \frac{a_u}{s_{\mathrm{l},0}} = \frac{\lambda_u}{\rho_u c_{\mathrm{p,u}} s_{\mathrm{l},0}} \tag{2.9}$$

Other definitions of the laminar flame thickness can be found e.g. in Ciccarelli and Dorofeev [25]. The authors define the laminar flame thickness based on the kinematic viscosity of the unburned gas and the laminar burning velocity:

$$\delta_F = \frac{\nu_u}{s_{\mathrm{l},0}} \tag{2.10}$$

2.3 Flame front instabilities

In Fig. 1.1 the effect of flame front wrinkling due to instabilities is visualized. Shadowgraphy recordings of a lean (13 %) and a nearly stoichiometric (30 %) hydrogen-air flames at an initial pressure level of 1 bar are compared with each other. These images were obtained through the GraVent facility used in the present work. In both cases, a homogeneous mixture with negligible initial turbulence is ignited by a weak spark at the left border of the picture. After spark ignition, the flame front propagates hemispherically until it reaches the channel top and bottom walls. Finally, the flame front propagates from left to right through the channel, passing the optically accessible area of the GraVent facility.

Depending on the initial and boundary conditions of the investigated problem, different flame instabilities can develop and alter the flame front surface. A possible categorization of the instability mechanisms is to separate the instability mechanisms based on whether they are of intrinsic nature or mainly caused by external effects.

- Flame instabilities developing due to intrinsic effects and not external forces:
  - Landau-Darrieus/hydrodynamic instability: disturbances of the flame front are amplified due to thermal expansion across the flame front.
  - Thermal-diffusive instability: caused by imbalances of species and heat diffusion.
- Flame instabilities developing due to effects of external forces like pressure waves, buoyancy or turbulence:
  - Rayleigh-Taylor instability: appears in accelerating fluids with different densities, for example in gravity.
  - Richtmeyer-Meshkov instability: caused by shock waves propagating across the interface separating fluids with different densities.
  - Kelvin-Helmholtz instability: the instability develops in the shear layer of fluids propagating with different velocities.
  - Acoustic instability: reflected acoustic waves lead to pressure oscillations which are coherent with the heat release in the flame.

Since the focus of this work is on the initial phase of flame propagation in unobstructed channels in quasi-laminar conditions, the hydrodynamic and thermal-diffusive instability mechanisms were identified as the most influential and will be discussed in more detail in the subsequent sections.

2.3.1 Landau-Darrieus instability

Propagating flame fronts which can be seen as waves of density discontinuities, are intrinsically unstable for perturbations of all wavelengths due to the omnipresent thermal expansion across the flame front [77] [78] [16]. If a flame front element is slightly curved convex towards the

fresh gas, as depicted in Fig. 2.4 the streamlines are diverging while approaching the flame front. Due to mass conservation the gas velocity decreases, while the local laminar burning velocity remains constant. That way wrinkling is further amplified. The second effect contributing to wrinkling of the flame front is the convergence of streamlines behind the flame front due to the density jump, as depicted in the close-up view in Fig. 2.4. This is a self-sustained fuel type independent instability mechanism and is solely caused by the propagating density discontinuity.

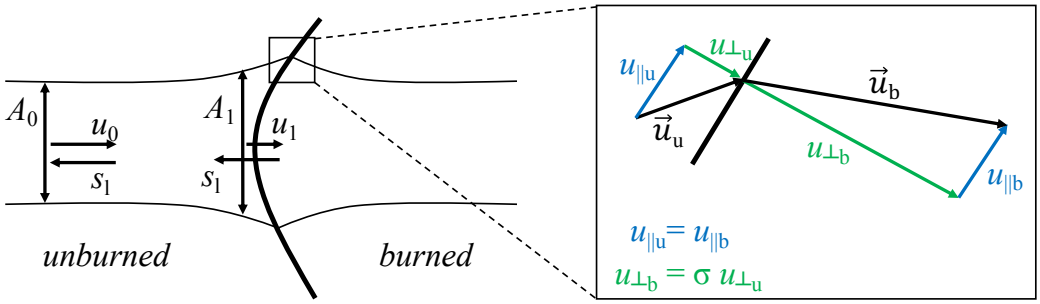

Figure 2.4: Depiction of the hydrodynamic instability effects on the flame front.

Depending on the stoichiometry of the mixture, this instability mechanism can be damped by thermal-diffusive effects [8] [16] [75]. This leads to the development of flame front wrinkling only after a certain run-up distance. With increased hydrogen content in the mixture the flame front becomes more stable. When the mixture approaches stoichiometry no flame front wrinkling can be observed in the initial propagation phase. In spherical flame propagation this run-up distance is expressed by the Peclet number, defined as follows:

$$\mathrm{Pe} = \frac{r}{\delta} \tag{2.11}$$

This dimensionless number compares the run-up distance of the flame front after ignition r to the flame front thickness δ. Only after the critical Peclet number $\mathrm{Pe}_{\mathrm{cr}}$ is exceeded, development of flame front wrinkling can be observed. Bradley [16] reports a critical Peclet number $Pe_{cr} = 1782$ for a rich hydrogen-air mixture of 36.4%. The leaner the mixture, the

earlier flame wrinkling can be observed, resulting in smaller Pe_{cr} values than in the 36.4% case.

2.3.2 Thermal-diffusive instability

Lean hydrogen-air mixtures have effective Lewis numbers below unity, which are considered an indication of thermal-diffusive instabilities. The lower the hydrogen concentration of the lean mixture, the stronger the flame front augmentation because of local small-scale wrinkling caused by these instabilities. These instabilities are caused by hydrogen accumulation in the convex shaped parts of the flame front due to preferential diffusion of the deficient species in the mixture (hydrogen in lean hydrogen-air mixtures) as shown in Fig. 3.6, [74].

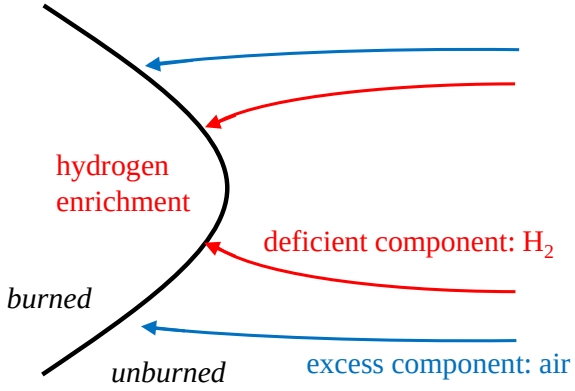

Figure 2.5: Depiction of the preferential diffusion effect for mixtures with high differences of the diffusion coefficients of the components.

The Lewis number is defined in Eq. 2.12. It compares the thermal diffusivity of the mixture to the diffusivity of the deficient species, which is hydrogen in the investigated case:

$$\mathrm{Le} = \frac{a}{D} \tag{2.12}$$

A deviation of the Lewis number from the value of 1, denotes an imbalance of thermal and species diffusivities. Fig. 2.6 shows the influence

of the Lewis number on stabilizing or destabilizing a flame front. If the counteracting effect of thermal diffusion in the mixture is sufficiently weak, these hydrogen accumulations cause increased temperatures and thus higher reaction rates, which lead to flame acceleration in these convex flame sections and the exact inverse process occurs when the counteracting effect of thermal diffusion is sufficiently strong.

This mechanism promotes or damps small perturbations and wrinkles the front progressively, which intensifies or abates the prior effect of hydrogen accumulation. The flame front becomes more or less convex and a self-supporting instability mechanism is amplified or damped.

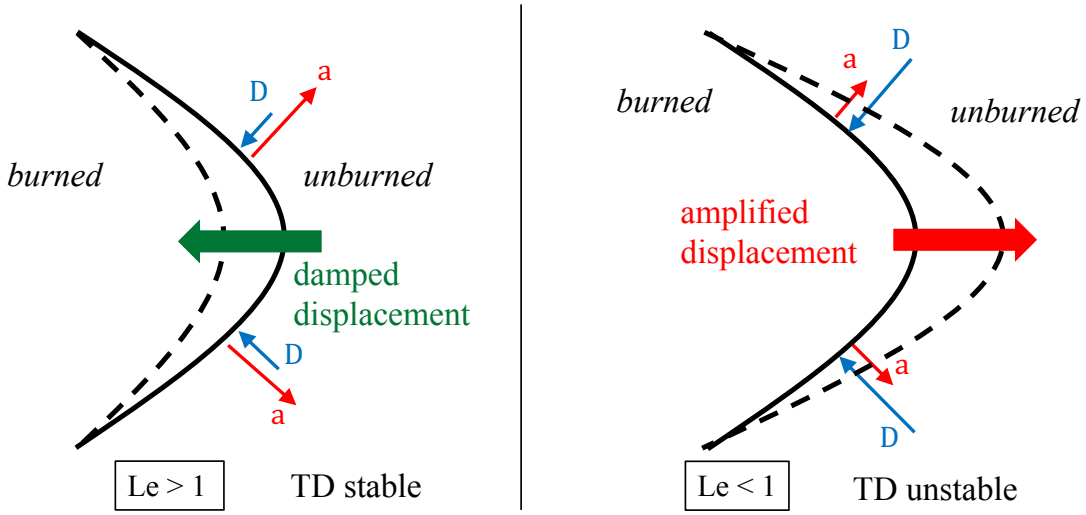

Figure 2.6: Depiction of the thermal-diffusive instability on flame fronts exhibiting different effective Lewis numbers.

2.3.3 Combined LD and TD instability

Flame front stability analyses in the sense of the determination of growth rates of harmonic perturbations have been developed for the hydrodynamic and thermal-diffusive instability mechanisms [77]. Additionally, the stabilizing effect of stretch has been identified and included by Zeldovich et al. [117]. Bechtold and Matalon [8] combined all three effects for stability analyses in spherically expanding flames. A further discussion with some corrections is presented by Bradley [16]. A summary and

overview can be found in Keppeler and Pfitzner [61]. In the present work the investigated flame configuration corresponds in the initial phase after ignition to hemispherical flame propagation. The effects of the hydrodynamic and thermal-diffusive instabilities and especially the influence of stretch play a significant role in these flames.

For spherically expanding flame fronts a spherical wavenumber can be defined:

$$n = \frac{2\pi \mathrm{Pe}}{\Lambda / \delta_T} \tag{2.13}$$

with the harmonic perturbation of the flame front Λ and the non-dimensionalized radius expressed in the form of the Peclet number, defined in Eq. 2.11. It is emphasized that the Peclet number is pressure dependent due to the formulation based on the laminar flame thickness.

The dimensionless amplitude of the perturbation relative to the flame front is defined as:

$$a = a_0 \left(\frac{r}{r_0} \right)^{\sigma_{\mathrm{LD,sp}} (1 + \Omega / Pe_r \ln(r/r_0))} \tag{2.14}$$

with the initial dimensionless amplitude a_0 of the perturbation. The logarithmic growth rate of the amplitude of the perturbation ω_{sp} dependent on the Peclet number is defined as follows:

$$\omega_{\mathrm{sp}} = \frac{d\ln(a/a_0)}{d\ln(\mathrm{Pe})} = \underbrace{\omega_{\mathrm{LD,sp}}}_{\text{LD instability}} - \underbrace{\omega_{\mathrm{LD,sp}} \frac{\Omega}{\mathrm{Pe}}}_{\text{TD instability + stretch}} \tag{2.15}$$

The respective contributions through LD-, TD- and stretch-effects to the overall growth rate are additionally indicated.

Depending on the stoichiometry and the Peclet number three different cases are discussed. Fig. 2.7 shows the case of a lean flame with an equivalence ratio of $\Phi = 0.35$ after a non-dimensional run-up distance of $\mathrm{Pe} = 500$. The overall growth rate is depicted on varying wave number.

A positive growth rate means that the instability is undamped and that it is developing. The plot shows the growth rates of the LD and the TD instability, which are both positive. The superposition of both instability mechanisms is therefore also positive which means that the flame front develops wrinkling due to this instability mechanisms.

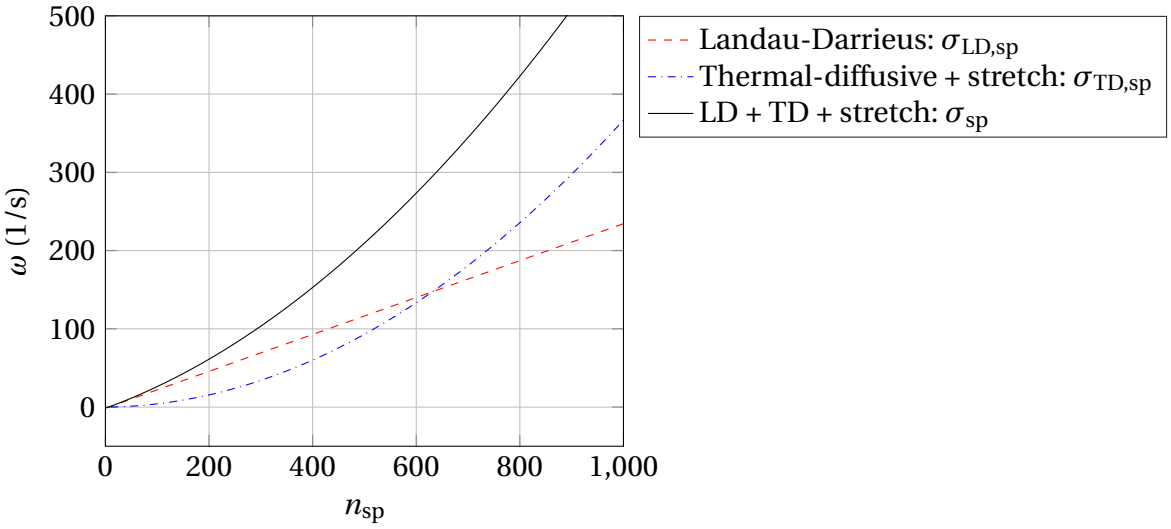

Figure 2.7: Overall growth rate of instability over varying spherical wave number for a mixture with $\Phi = 0.35$ at a non-dimensional run-up distance of Pe = 500.

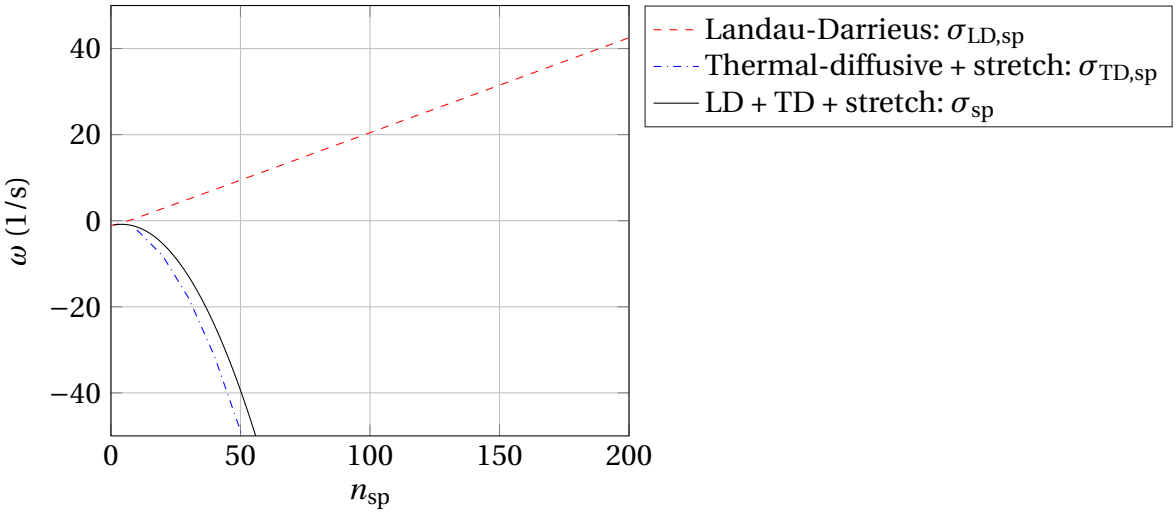

Figure 2.8: Overall growth rate of instability over varying spherical wave number for a mixture with $\Phi = 0.9$ at a non-dimensional run-up distance of Pe = 50.

Figure 2.8 shows the same variables but at an equivalence ratio of $\Phi = 0.9$ and a non-dimensional run-up distance of Pe = 50. It can be observed that the growth rate of the LD instability is positive. However, the growth rate of the TD instability is negative. The superimposed growth rate is negative which means that no flame front wrinkling can be observed on the flame surface. Figure 2.9 shows the growth rates at the same equivalence ratio of $\Phi = 0.9$ but at a larger distance corresponding to a Peclet number of Pe = 500. The growth rate of the LD instability is unchanged positive. The growth rate of the TD instability is also still negative but exhibits higher values so that the superimposed growth rate is positive in a certain wave number range. The highest (n_s) wave number limiting this range corresponds to the smallest length scale and the lowest (n_l) wave number corresponds to the largest length scale of the developing flame front wrinkling. The wave number (n_m) corresponding to the highest growth rate, indicates the length scale of the instability that is developing predominantly.

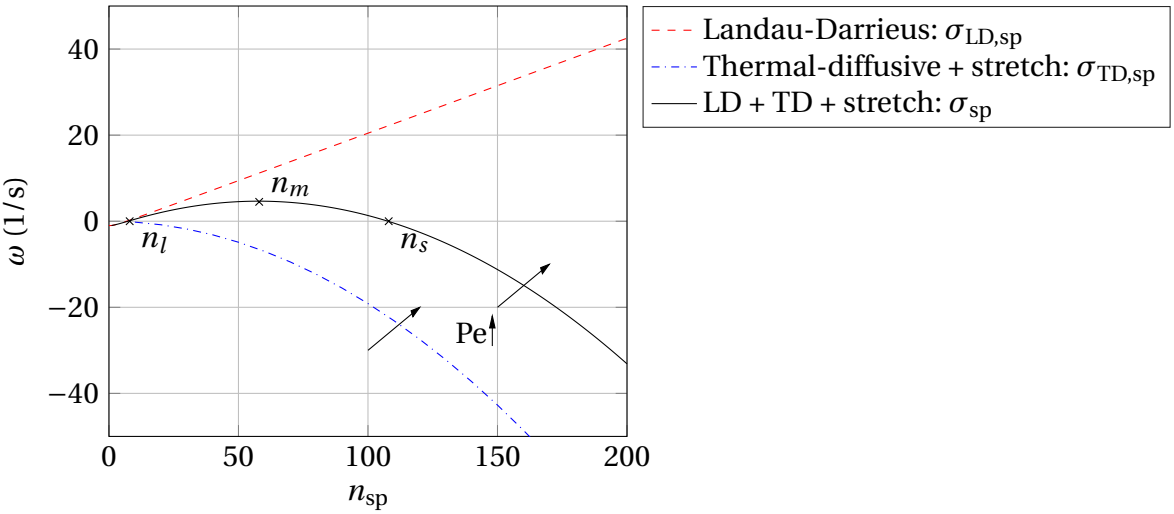

Figure 2.9: Overall growth rate of instability over varying spherical wave number for a mixture with $\Phi = 0.9$ at a non-dimensional run-up distance of Pe = 500. Additionally, characteristic wave numbers are depicted.

As can be seen in Figs. 2.7, 2.8 and 2.9 the LD instability is omnipresent in flames across the entire stoichiometry range and cannot be decoupled from the TD instability. Depending on the stoichiometry, the TD instability is damping or amplifying the effect of flame front wrinkling.

The observed effect of flame front wrinkling discussed in the present work is caused by a combination of LD and TD instability mechanisms under influence of stretch. The effects cannot be decoupled from each other and therefore small-scale wrinkling observed in the present work is considered as the result of the superposition of all three effects.

2.4 Flame Stretch

Flame front wrinkling due to intrinsic instability mechanisms is not only increasing the flame surface area but also altering the local laminar flame speed along the flame front due to stretch effects. The laminar burning velocity equals the unstretched value only in the one-dimensional case [107].

In the investigated case of lean hydrogen-air mixtures with Lewis numbers below unity, positive stretch effects lead to an increase of the local laminar burning velocity. Flame stretch is defined as the normalized rate of change of a flame surface area element and can be described with the Karlovitz stretch factor [69]:

$$K = \frac{1}{A}\frac{dA}{dt} \tag{2.16}$$

The overall flame stretch K is usually composed of two parts, strain and curvature:

$$K = K_s + K_c \tag{2.17}$$

Strain is the outcome of non-uniform flow ahead of the flame front in form of tangential velocity gradients. Curvature is caused by the propagating curved flame front itself. Due to the low propagation velocities of the flame front and therefore low flow velocities of the fresh gases ahead of the flame and the quasi-laminar nature of the problem, strain is expected to play a minor role in the investigated cases and will be neglected. This assumption is in accordance with observations in literature, according to Markstein et al. [79] and Peters [88].

In this work stretch is assumed to be mainly caused by flame front curvature:

$$K = K_c \tag{2.18}$$

The most commonly used relationship between stretch and burning velocity for moderate stretch rates is of linear nature and reads as follows [26] [49] [103]:

$$s_{l,s} = s_{l,0} - \mathscr{L} K \tag{2.19}$$

Equation 6.16 exhibits the variable $\mathscr{L}$, known as the Markstein length. The Markstein length can be understood as a factor for the influence of stretch on the laminar burning velocity. In spherically outward expanding flames, the convex curvature of the flame front towards the fresh gas is defined as positive. This results in a positive stretch factor K. Accordingly the concave part is defined as negative. Lean hydrogen-air mixtures exhibit negative Markstein lengths. Following Eq. 6.16 it can be concluded that outwardly propagating spherical flames in lean hydrogen-air mixtures exhibit higher burning velocities compared to the unstretched case. Often the Markstein length $\mathscr{L}$ is non-dimensionalized with the laminar flame thickness resulting in the so-called Markstein number [79]:

$$\mathrm{Ma} = \frac{\mathscr{L}}{\delta} \tag{2.20}$$

According to this, flame stretch can be connected to the Karlovitz number:

$$\mathrm{Ka} = \frac{K\delta}{s_{l,0}} \tag{2.21}$$

The Markstein lengths used throughout this work are always defined with reference to the unburned gas.

2.5 Unsteady laminar flame fronts

Since flame propagation velocities play a central role in this work, important relationships must be introduced. The investigated problem exhibits unsteady flame front propagation in a closed channel. For this reason the observed flame velocity in the laboratory reference system is not identical to the burning velocity specified in Sec. 2.2.1, which is a chemical property of the specific mixture under specific thermodynamic conditions.

The flame front is propagating with the velocity s_u in respect to the unburned fresh gas ahead of the flame. The fresh gas itself is moving with the velocity u due to the piston-like effect of the moving flame front. The sum of both velocities is the observed propagation velocity u_F in the laboratory reference system:

$$u_F = u + s_u \tag{2.22}$$

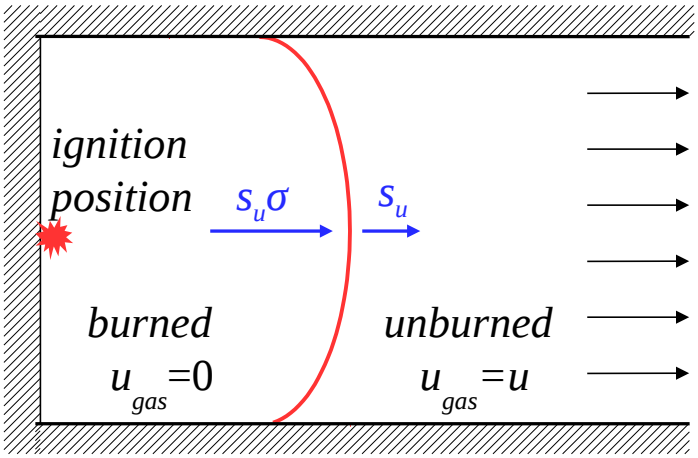

Figure 2.10: Side view of a propagating smooth flame front in a channel geometry with a closed end at the ignition position. The variable u_{gas} denotes the local gas velocity in the burned and unburned gas respectively.

With respect to the propagating flame front, the products behind the flame front are moving with the velocity σs_u. The density ratio σ is de-

fined according to Eq. 2.2.

The closed channel wall at the left side (see Fig. 2.10) imposes a zero velocity boundary condition behind the flame front with respect to the external observer. In order to satisfy this boundary condition the flame front velocity u_F must be identical to the propagation velocity the products σs_u, only in the opposite direction. This leads to the formulation:

$$\sigma s_u = u_{\text{gas}} + s_u \tag{2.23}$$

Finally, the variable s_u can be substituted with an appropriate flame speed definition depending on the investigated case. Is the flame propagating in quiescent mixture at atmospheric conditions and with negligence of stretch influence, s_u can be represented by the unstretched laminar burning velocity $s_{\text{l},0}$ stated in Eq. 2.5.

2.6 Turbulent burning characteristics

Turbulence plays a significant role in combustion as it can accelerate flame fronts to velocities where they can undergo a deflagration-to-detonation transition with devastating effects on the environment. Additional to laminar heat and mass transfer, turbulent transfer of heat and mass takes place in turbulent flows. This turbulent diffusion can exceed the laminar counterpart by orders of magnitude.

Turbulent flows exhibit a wide range of length and timescales. Based on these scales Kolmogorov [64] describes turbulence as a cascade process with an energy containing range (largest eddies), an universal range and an dissipation range (smallest eddies). The energy of the turbulent flow is contained in the eddies of the size of the integral length scale l_t. The integral length scale denotes the mean size of the largest turbulent eddies contained by the flow. The turbulent kinetic energy k transported to the smaller eddies is defined as follows:

$$k = \frac{1}{2} u_i'^2 = \frac{3}{2} u'^2 \tag{2.24}$$

with u_i' as the root mean square value of the turbulent velocity fluctuation and with $i = 1,2,3$ representing the three spatial directions. The often made simplification of isotropic turbulence assumes identical velocity fluctuations u' in all three spatial directions. The energy k is constantly transported at the rate of dissipation ϵ:

$$\epsilon = \frac{u'^3}{l_t} \tag{2.25}$$

to smaller size eddies until the energy is dissipated in the smallest eddies, where the inertial forces cannot overcome the viscous forces. The length scale of the smallest eddies in the fully developed turbulent flow are defined as follows:

$$\eta = \left(\frac{\nu^3}{\epsilon}\right)^{0.25} \tag{2.26}$$

A more detailed description of turbulent flows and turbulent processes can be found in the literature, e.g. Pope [91].

Flows can be categorized as laminar or turbulent by the means of the non-dimensional Reynolds number. This variable compares momentum and viscous forces and is defined as follows:

$$\mathrm{Re} = \frac{ul}{\nu} \tag{2.27}$$

with flow velocity u and a length scale l, e.g. tube diameter. The transition of an initially laminar flow to the turbulent state occurs when a case specific critical Reynolds number is exceeded.

Substituting the velocity and length scale in Eq. 2.27 with turbulent values like the turbulent fluctuation velocity u' and the turbulent length scale l_t the turbulent Reynolds number Re_t can be defined in the following way:

$$\mathrm{Re}_t = \frac{u' l_t}{\nu} = \frac{u' l_t}{s_{\mathrm{l},0}\delta_F} \tag{2.28}$$

with $\delta_F = \nu / s_{l,0}$ (Eq. 2.10). The turbulent Reynolds number allows for an easier classification of the flow regime since the transition of laminar to turbulent occurs at the value of unity. The higher the turbulent Reynolds number Re_t, the more important are turbulent exchange processes.

To compare turbulent and chemical scales and to determine how turbulence is affecting chemistry, Borghi [14] [15] suggested a diagram comparing the ratios of velocity and length scales. Fig. 2.11 shows the Borghi diagram with extensions to the original formulation by Peters [88]. Different non-dimensional numbers are depicted in the diagram, indicating flame regimes based on the turbulence-chemistry interaction. The already introduced turbulent Reynolds number Re_t is plotted in Fig. 2.11 for the value of 1, separating the laminar and turbulent regimes of the diagram.

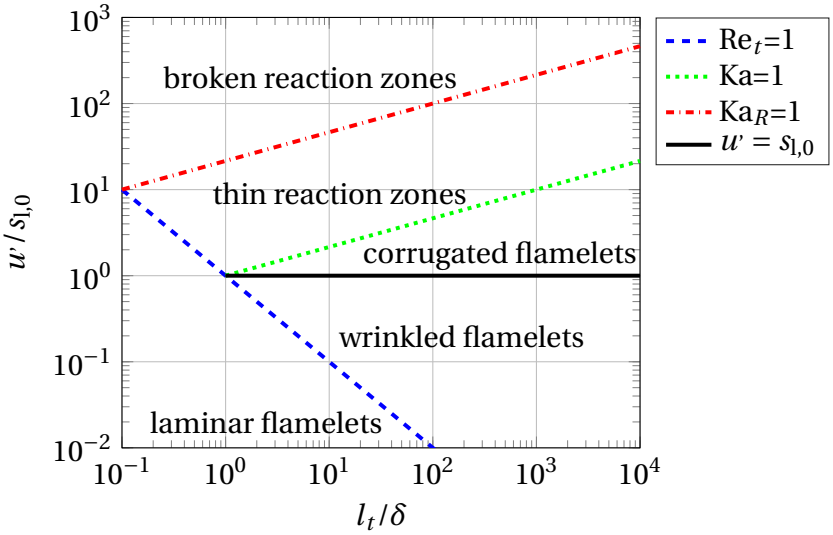

Figure 2.11: Borghi combustion diagram [14] [15] with modifications by Peters [88].

The Karlovitz number compares the chemical timescale τ_F corresponding to the entire flame thickness to the Kolmogorov timescale (as the smallest scale) τ_η and is defined as follows:

$$\mathrm{Ka} = \frac{\tau_F}{\tau_\eta} = \left(\frac{\delta_F}{\eta}\right)^2 \tag{2.29}$$

The Karlovitz number for a value of 1 is depicted in Fig. 2.11, separating

the flamelet regime and the thin reaction zones regime. In the flamelet regime Ka < 1 the smallest turbulent eddies are still larger than the laminar flame thickness and therefore cannot penetrate and alter the inner flame structure. Turbulence can only wrinkle and corrugate the flame front kinematically. The flamelet regime itself can be divided by the condition $u'/s_{l,0} = 1$ into a wrinkled flamelets regime $u'/s_{l,0} < 1$ and a corrugated flamelets regime $u'/s_{l,0} > 1$.

The second Karlovitz number Ka_R compares the chemical timescale corresponding to the reaction zone thickness τ_R with the Kolmogorov timescale or reaction zone thickness δ_R to the Kolmogorov thickness:

$$\mathrm{Ka}_R = \frac{\tau_R}{\tau_\eta} = \left(\frac{\delta_R}{\eta}\right)^2 \approx 0.01\mathrm{Ka} \tag{2.30}$$

with the assumption of $\delta_R = 0.1\delta_F$ [88]. The area confined between the two Karlovitz numbers (Ka > 1 and Ka_R < 1) is called the thin-reaction zone regime. In this thin-reaction zone regime the smallest turbulent eddies are able to penetrate the inner flame structure and enhance the mixing of heat and species in the preheat zone but not in the smaller reaction zone.

In the broken reaction zones regime $\mathrm{Ka}_R > 1$ the turbulent eddies are small enough to enter even the reaction zone. Turbulent quenching occurs in this regime as turbulent eddies can transport cold reactants in the reaction zone. No compact flame structure can be identified in this regime.

Figure 2.12 shows an OH-PLIF image (Planar Laser-induced Fluorescence image of the OH-radical) of a propagating flame front experimentally obtained in this work. The flame front corresponds to a mixture of 13% and an initial pressure level of 1 bar and is propagating from left to right. The colors correspond to the detected intensity of the OH-PLIF signal, with red as high intensity and blue as low intensity. As expected, the highest intensity values can be found in the vicinity of the flame front. Despite the wrinkling of the flame front is not caused by turbulence, the flamelet assumption holds for the observed phase of flame propagation since no broken reaction zones can be identified. This observation has

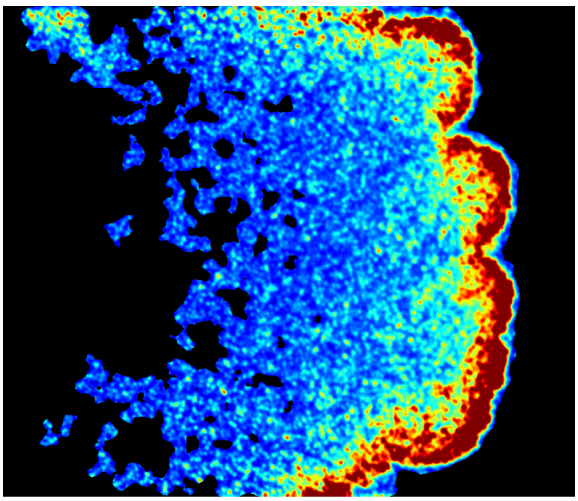

Figure 2.12: A planar laser-induced fluorescence image of the OH-radical (OH-PLIF) showing a flame front propagating from left to right for a concentration of 13% and an initial pressure level of 1 bar.

been made for flame fronts in the entire concentration range investigated in the present work.

Based on this observation the computation of chemistry and turbulence in CFD-simulations can be separated. The flame front is assumed to be an ensemble of small flamelets with one-dimensional inner flame structure. These flamelets can be calculated prior to the simulation and saved in so-called flamelet tables. This approach saves computational time and increases the robustness of the calculation.

2.7 Premixed combustion modeling

Numerous approaches for turbulent combustion modeling can be found in literature. Extensive discussions can be found in Poinsot and Veynante [89], Gerlinger [45] or Ferziger and Perić [39]. The goal of this chapter is not to reproduce and discuss well known turbulent combustion modeling approaches that can be found in the literature given above. Instead, the goal is to briefly outline the most important relations generally utilized in premixed URANS combustion modeling and to show the point at which the outcome of this work is considered in the holistic modeling

concept. Instantaneous conservation equations for mass, momentum, energy and species are the starting point for numerical fluid simulations. A summary of the set of these partial differential equations can be found in Poinsot and Veynante [89]. The influence of turbulence on these equations requires an averaging process to decrease computational costs.

Turbulent flows are characterized by unsteady three-dimensional fluctuations of the variables. The generic turbulence affected variable ϕ can be decomposed in an average value and a fluctuating value:

$$\phi = \overline{\phi} + \phi' \tag{2.31}$$

This procedure is called Reynolds decomposition [94]. In unsteady flows the determination of the mean value $\overline{\phi}$ is defined as the ensemble average:

$$\overline{\phi} = \frac{1}{N} \sum_{k=1}^{N} \phi_k \tag{2.32}$$

with N denoting the amount of data points to average. Averaging of the fluctuating variable results in:

$$\overline{\phi'} = 0 \tag{2.33}$$

This averaging procedure is mainly applied to inert flows. However, in reactive flows, the large density change across the flame front results in correlations between the flow variables and the density fluctuations, which are generally not negligible. This way the conservation equations become very complex by solely utilizing Reynolds-averaging [45]. To overcome this downside, the density-weighted Favre-averaged variables can be used. This averaging procedure is based on the decomposition of the variables defined as follows:

$$\phi = \widetilde{\phi} + \phi'' \tag{2.34}$$

with the averaged variable $\widetilde{\phi}$ and the fluctuating variable ϕ''. The averaged variable can be expressed in the following way:

$$\widetilde{\phi} = \frac{\overline{\rho\phi}}{\overline{\rho}} \tag{2.35}$$

An important definition of the Favre-averaging process is that the following definition holds:

$$\overline{\rho\phi''} = 0 \tag{2.36}$$

Due to the modified averaging process introduced in Eq. 2.35, the averaged conservation equations maintain their usual structure. For this reason, pressure and density in conservation equations are usually Reynolds-averaged and all other variables are usually Favre-averaged.

In premixed combustion simulations the compressible transport equation of the Favre-averaged reaction progress variable $\widetilde{c}$, depicted in Eq. 2.38, is solved. This quantity is bound to values from 0 (reactants) to 1 (products), passing through all intermediate values in the flame front. The main idea behind this strategy is to save computational power by reducing the system of partial differential equations by linking the tabulated species mass fractions to the reaction progress variable $\widetilde{c}$. Instead of computing the transport equations for every species involved, only the transport equation for the reaction progress variable is solved. Afterwards, the species mass fractions can be computed from distribution of the reaction progress variable, which is defined as follows:

$$\widetilde{c} = \frac{\widetilde{T} - T_u}{T_b - T_u} \tag{2.37}$$

The transport equation reads as follows:

$$\frac{\partial}{\partial t}(\overline{\rho}\widetilde{c}) + \frac{\partial}{\partial x_k}(\overline{\rho}\widetilde{u}_k\widetilde{c}) = \frac{\partial}{\partial x_k}\left[\left(\overline{\rho}D + \frac{\mu_t}{\mathrm{Sc_t}}\right)\frac{\partial\widetilde{c}}{\partial x_k}\right] + \overline{\dot{\omega}}_c \tag{2.38}$$

Due to the averaging process, Eq. 2.38 is not closed and therefore cannot

be solved without modeling the unknown source term $\overline{\dot{\omega}}_c$. One possibility to close this term, is the closure suggested by Zimont [119]:

$$\overline{\dot{\omega}}_c = \overline{\rho}_u s_t |\nabla \tilde{c}| \tag{2.39}$$

The main advantage of this closure is the formulation of the mean reaction rate dependent on the gradient of the Favre-averaged reaction progress variable. This strategy results in an integral reaction rate independent from the grid resolution. That means that the integral reaction rate is not affected by the spatial resolution of the flame brush [29].

Another advantage of this closure is the possibility to incorporate experimental results through the formulation of so-called turbulent flame speed correlations. A large number of flame speed correlations can be found in the literature. Especially in Lipatnikov and Chomiak [76] a detailed overview and discussion of flame speed models with focus on turbulence driven acceleration can be found. The strategy pursued in the present work is to formulate a new correlation for the turbulent flame speed incorporating identified flame accelerating effects and to close Eq. 2.39.

2.8 Damköhler's approach

Damköhler originally introduced the relationship of the ratio of the wrinkled and smooth flame surface area to the ratio of a turbulent and laminar burning velocity. Moreover, he identified a small-scale and a large-scale turbulence regime and developed expressions for resulting burning velocities for both cases [28]. The circumstance that flame surface areas and flame propagation velocities are proportional to each other is also reported through Driscoll [37].

However, Damköhler investigated flame front enlargement due to the influence of turbulence. In the present work, this concept of an accelerating flame due to flame front enlargement is applied to flame front enlargement caused by flame instabilities. The continuity of mass across

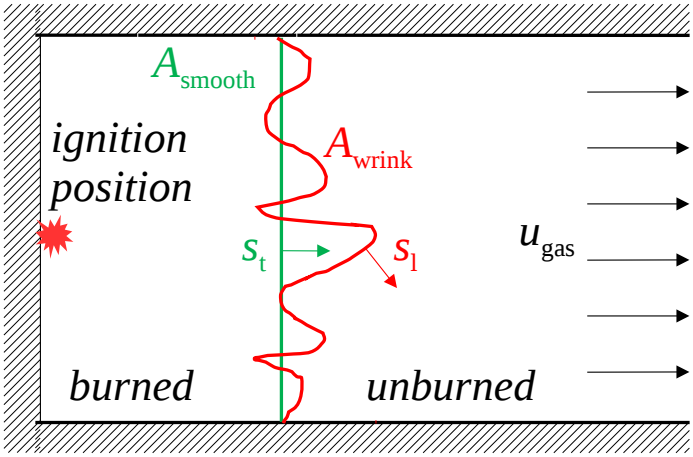

Figure 2.13: Propagating wrinkled flame front in a channel geometry with a closed end at the ignition position. Additionally, a theoretical smooth flame front is depicted.

the flame front can be formulated as follows:

$$\dot{m} = \rho_u A_{\text{wrink}} s_l = \rho_u A_{\text{smooth}} s_t = \text{const.} \tag{2.40}$$

Based on this, the corresponding burning velocity s_t can be defined:

$$s_t = \Xi \cdot s_l \approx \frac{A_{\text{wrink}}}{A_{\text{smooth}}} \cdot s_l \tag{2.41}$$

Figure 2.13 shows a wrinkled flame front A_{wrink}. Additionally, the corresponding theoretical smooth flame front A_{smooth} is shown. The flame front propagates from left to right, away from the ignition position at the left end wall. The wrinkled flame front propagates in this case locally with the laminar burning velocity s_l. On the basis of the formulation in Eq. 2.41, factor Ξ can be calculated by comparing the wrinkled flame front to the corresponding smooth flame front without small-scale wrinkling.

3 Test facility and measurement techniques

3.1 Small-scale explosion channel - GraVent

The experimental setup used in this work was originally developed in a previous project by Vollmer [110]. It is an unobstructed explosion channel with a rectangular cross-section. As depicted in Fig 3.1, the channel height is 0.06 m and the channel width is 0.3 m. The channel length is 1.3 m, as shown in the top view in Fig. 3.2. The GraVent test facility is built in a modular way with two different types of segments. In this work a standard segment was combined with an optical segment, the latter allowing optical access to the explosion channel through lateral quartz-glass windows. The ignition position and the optically accessible area are highlighted in Fig. 3.2. The hydrogen-air mixture is generated inside the channel using the partial pressure method. After this, the mixture is ignited through a spark plug (NGK BKR6EIX-LPG). Both channel ends are closed with plates. One of them has a quartz glass window, allowing a laser beam to enter the channel volume along the center line permitting OH-PLIF measurements.

Fig. 3.3 shows values of the hydrogen mole fraction over injection time. The values were calculated with the partial pressure method comparing injected partial pressure into the channel to ambient pressure prior to the injection. Highlighted through the red dashed line is the detected linear correlation between the hydrogen mole fraction and the injection time. The experimentally determined values show only small deviations, hence a high reproducibility of the hydrogen concentration in the channel can be assumed. The determination of the hydrogen mole fraction after the injection is carried out prior to every single experimental run.

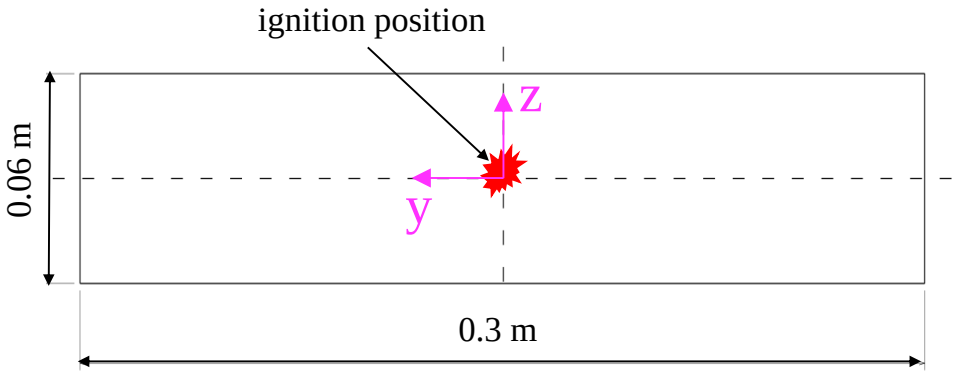

Figure 3.1: Channel cross section showing the height (z-direction) and the width (y-direction) of the GraVent facility.

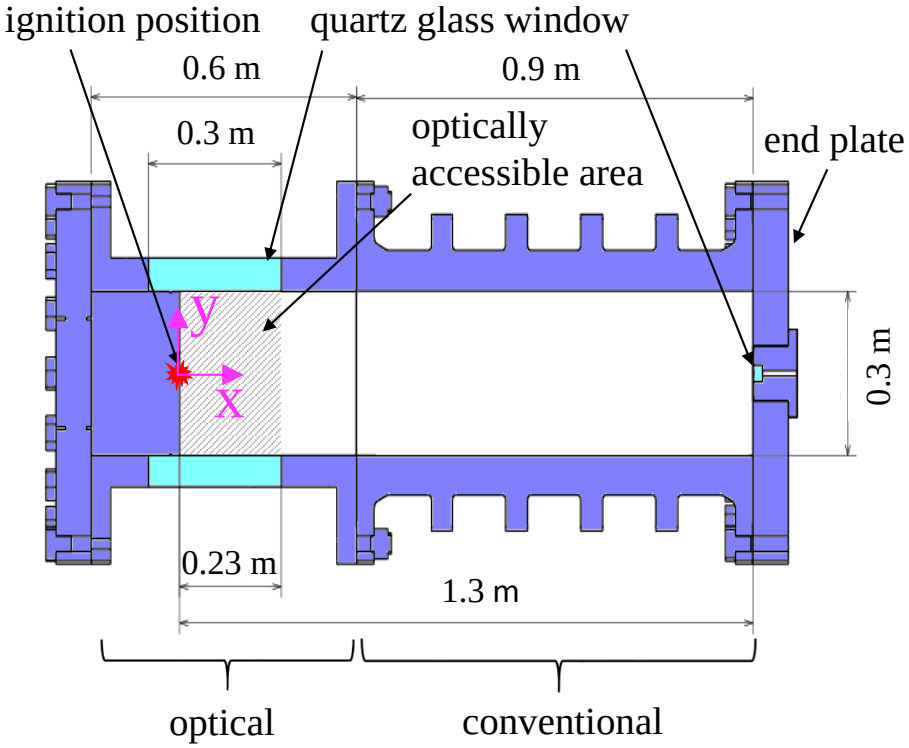

Figure 3.2: Sectional top view of the GraVent facility. The flame propagates mainly in x-direction.

To verify the assumption of a homogeneous distribution of the injected hydrogen in the explosion channel, experiments and simulations were conducted. Simulated profiles of the hydrogen mole fraction for different waiting times after injection are depicted in Fig. 3.4. Shortly after injection a non homogenous distribution along the channel height is observed. For longer waiting times the concentration gradient degrades

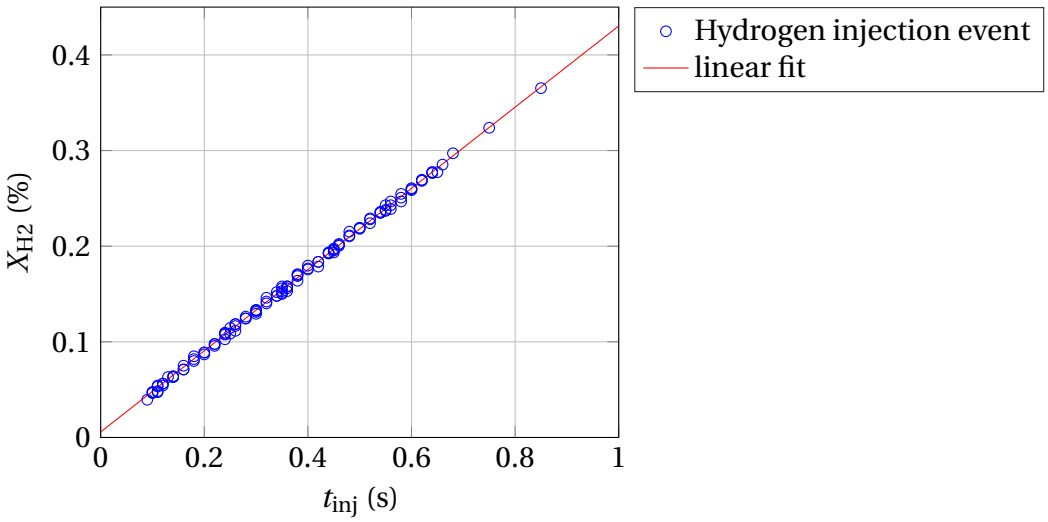

Figure 3.3: Calculated hydrogen concentrations plotted over injection time. The hydrogen concentrations are calculated from experimentally measured partial pressures of the injected hydrogen.

and the distribution becomes more homogenous throughout the channel height. After a waiting time of 30 s the distribution can be assumed as homogenous. Furthermore, it can be seen that after 60 s no decomposition of the mixture can be observed. Vollmer [110] investigated this process experimentally. Due to the hazardous properties of hydrogen, helium was used in these experiments. The binary diffusion coefficients of hydrogen and helium in air are similar which qualifies helium as an appropriate substitution for hydrogen [81]. During the experiment gas probes at various heights and at various waiting times were taken and analyzed gaschromatographically validating the assumptions and simulational results.

Since the focus of this work is to isolate the effect of laminar flame front instabilities, a low initial turbulence level has to be ensured. Therefore, the waiting time in the experiment was chosen to 60 s. This waiting time was assumed as sufficient for the initial turbulence to decay to negligible levels. Furthermore, the facility is equipped with temperature sensors indicating the desired initial temperature before every run. This way it can be confirmed that the facility reaches steady state between runs.

The GraVent facility allows a high repetition rate of experiments and a

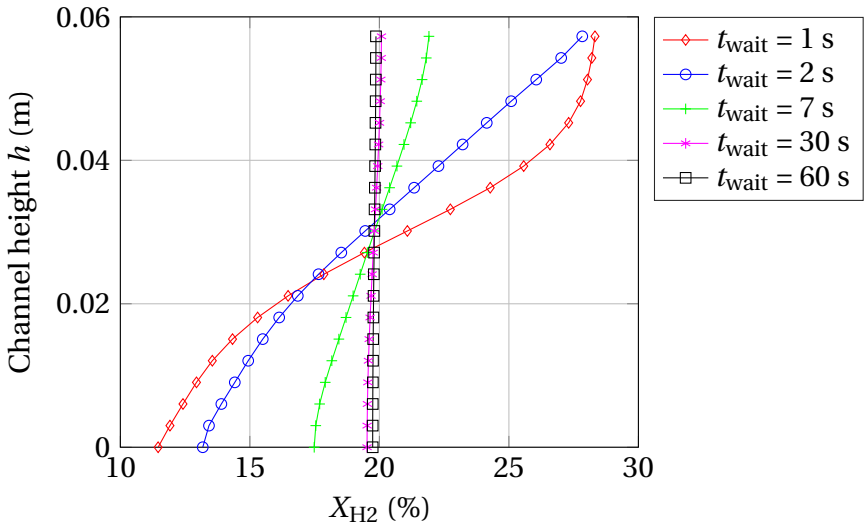

Figure 3.4: Simulated profiles of hydrogen mole fraction over the channel height with an average hydrogen concentration of 20 % H_2 for different waiting times.

high reproducibility of results. To ensure that, a standardized procedure to conduct the experiments was developed and is summarized as follows:

- Flushing of the channel with dry air for 5 minutes,
- partial evacuation of the channel volume with an external vacuum pump until the desired sub-atmospheric pressure level is reached,
- injection of hydrogen through nozzles in the top plate along the entire channel length until ambient pressure is reached,
- waiting for 60 s for the mixture to homogenize by diffusion and to reduce the turbulence level as far as possible prior to the experiment,
- ignition of the mixture and triggering of the high-speed cameras through the LabView control software,
- flushing the channel with dry air to exhaust the combustion products.

3.2 Conventional measurement techniques

The measurement techniques installed at the GraVent facility can be categorized in two groups. The first group can be considered as conventional measurement techniques, where the time-of-arrival photodiodes and the pressure transducers can be assigned. Both devices are mounted in the channel top plate along the channel axis, as depicted in Fig. 3.5.

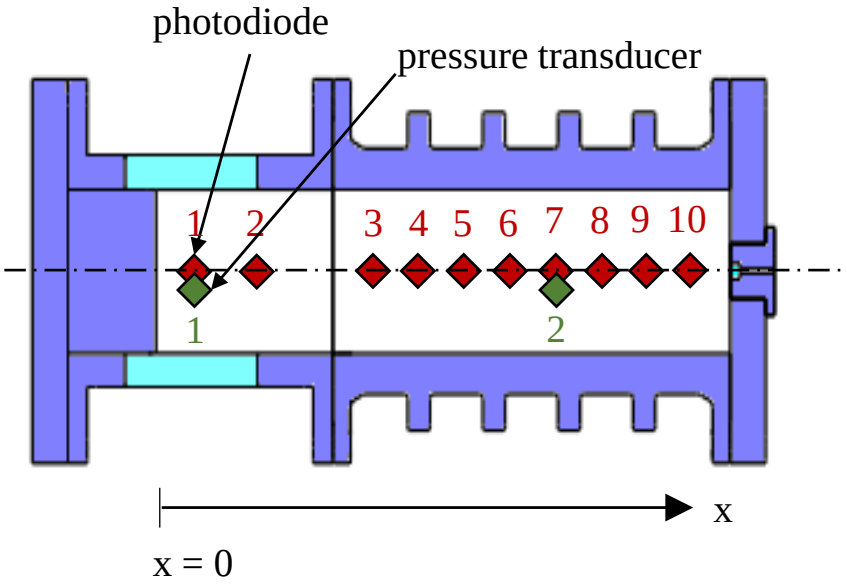

Figure 3.5: Depiction of the photodiode positions (red diamonds) and the pressure transducer positions (green diamonds).

3.2.1 Time-of-arrival photodiodes

The UV-sensitive photodiodes of type Hamamatsu S1336-18BQ are used to determine the arrival times of the passing flame front. Fig. 3.6 gives an overview of the photodiode setup installed in the channel top plate. The angle α determining the field of view of the photodiode has been determined to $\alpha \approx 6°$ in a prior project [110]. Due to the small channel height in the present work it has no significant influence on the calculated velocities based on the earlier detected arrival times of the flame fronts. The detected photodiode signal is measured with a sampling rate

of 250 kS/s, allowing for precise detection of flame front arriving times. Table 3.1 summarizes the mounting positions of the photodiodes.

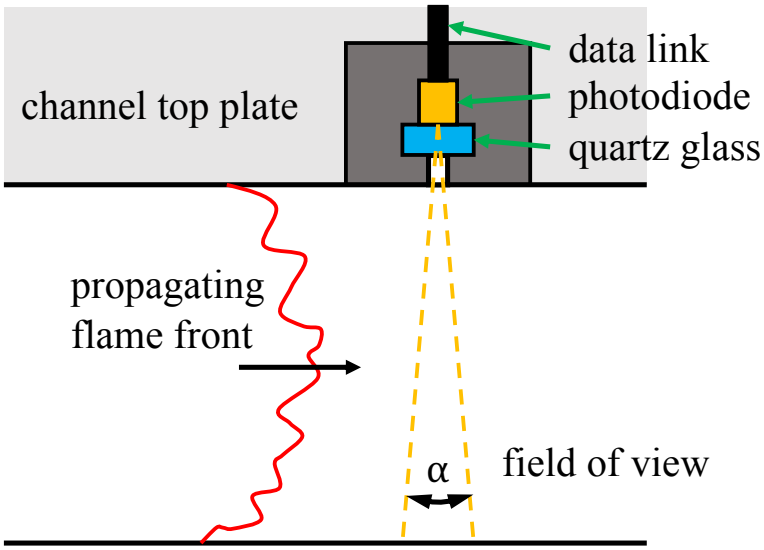

Figure 3.6: Overview of the photodiode setup in the explosion channel.

Table 3.1: Photodiode distances from the ignition position ($x = 0$).

Photodiode	1	2	3	4	5	6	7	8	9	10
Position (m)	0.1	0.2	0.5	0.6	0.7	0.8	0.9	1.0	1.1	1.2

Knowing the positions of the photodiodes (x_1 and x_2) and the arrival times of the flame (t_1 and t_2), velocity-distance diagrams can be obtained. Fig. 3.7 shows typical detected photodiode signals of a passing flame front. When the flame front reaches the light sensitive photodiode the signal rises to a peak value. To determine the arrival times of the passing flame front, a threshold value of the transmitted signal was chosen according to prior projects to determine the arrival time (dotted line) [110] [11]. The determination of the velocity values follows Eq. 3.1 where the mean flame velocity between two photodiodes is calculated. This calculated velocity corresponds to the flame front velocity observed by a stationary observer:

$$u_F\left(\frac{x_2+x_1}{2}\right)=\frac{\Delta x}{\Delta t}=\frac{x_2-x_1}{t_2-t_1} \tag{3.1}$$

with $x_2 > x_1$ and $t_2 > t_1$.

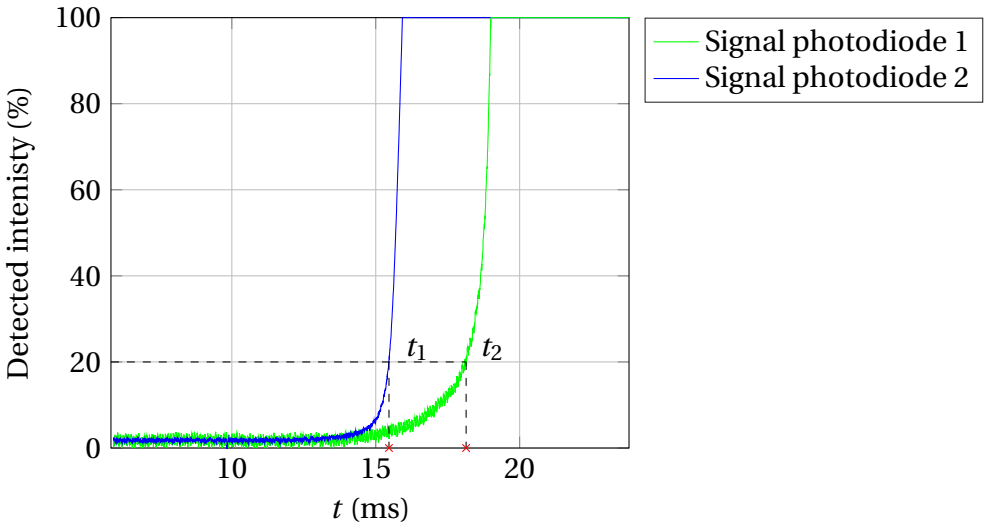

Figure 3.7: Typical detected raw photodiode signal of two photodiodes when a flame front is passing.

3.2.2 Pressure transducers

For measurement of the increasing pressure during an experiment, two piezoelectric pressure transducers Kistler 601A are used. Each of the two segments is equipped with one transducer. Fig. 3.5 shows the positions of the pressure transducers in the channel. Tab. 3.2 gives the exact positions of the pressure transducers along the channel axis. The transducers are mounted in the top plate of the channel and are connected to an external amplifier Kistler 5011B. The sampling rate of the pressure transducers is adjusted to 50 kS/s. High-temperature silicone was applied to the pressure transducers to avoid falsification of the pressure signal due to thermal shock [11] [110].

Table 3.2: Pressure transducer distances from the ignition position at $x = 0$ m.

Pressure transducer	1	2
Distance (m)	0.1	0.9

3.3 Optical measurement techniques

The optical measurement techniques used in this work are shadowgraphy and OH-PLIF. Both are performed simultaneously with a high time resolution of 20 kHz. The setup of the applied measurement techniques is depicted in Fig. 3.8. Shadowgraphy is conducted with a z-type setup, visualizing the second derivative of the density. The light source is a LOT Oriel Xe lamp with a power of 350 W and a broad band spectrum. A non-intensified Complementary Metal Oxide Semiconductor (CMOS) camera Photron SAX is used.

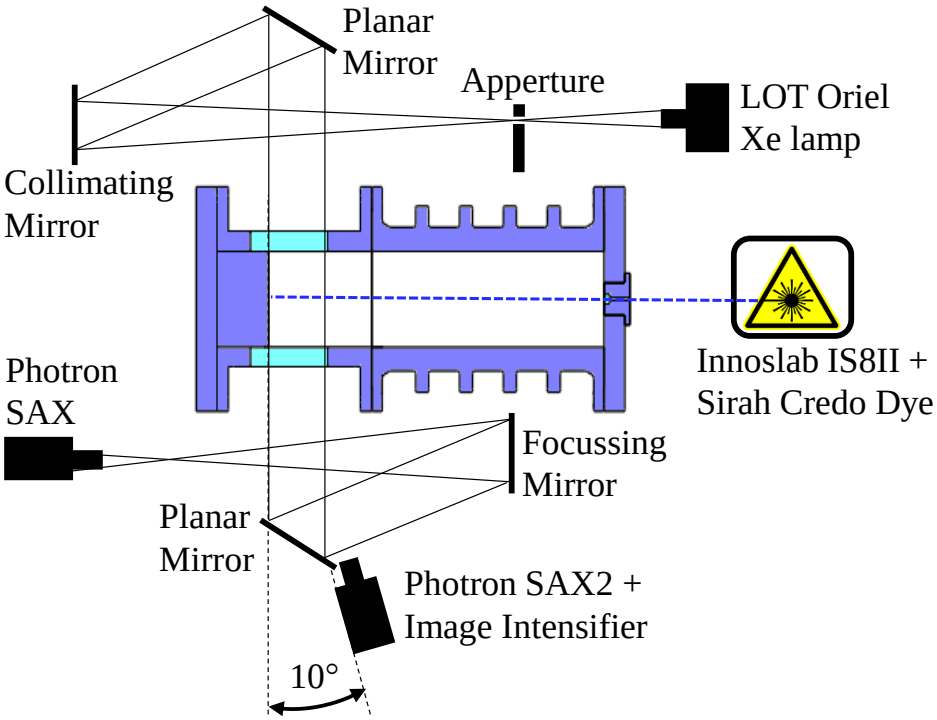

Figure 3.8: Setup of simultaneous shadowgraphy and OH-PLIF meausurement techiques.

The laser system used for the excitation of OH radicals is a combination of a diode-pumped solid-state Nd:YVO4 laser (INNOSLAB IS8II) and a tunable dye laser (Sirah Credo). The pumplaser emits at a wavelength of 532 nm. The dye laser is operating with Rhodamin 6G dissolved in ethanol, emitting light according to the desired set point of 565.89 nm in the resonator stage. After the following amplifier stage, the laser light

enters the Second Harmonics Generator (SHG) unit for frequency doubling. After separation of the occurring two wavelengths (565.89 nm and 282.94 nm) in the wavelength separation unit, only laser light at a wavelength of 282.94 nm exits the laser. This particular wavelength excites the transition of the OH radical from the $X^2\Pi_i$ band up to its excited state in the $A^2\Sigma^+$ band. For OH-PLIF measurements a CMOS camera Photron SAX2 is coupled with an external image intensifier Hamamatsu C10880-03. A 100 mm UV lens and a 320 ± 20 nm bandpass filter are used [13].

Table 3.3: Data of the used laser system consisting of the Innoslab IS8II pump laser and the Sirah Credo dye laser system [100].

	Innoslab IS8II	Sirah Credo
Power Output	43 W	2 W
Output Wavelength	532 nm	282.9446 nm
Repetition Rate	20 kHz	-
Output Energy	2 mJ	100 µJ
Pulse Length	6.5 ns	-

High-speed OH-PLIF measurements are conducted to gain information about microscopic flame topology, particularly about flame surface area increase due to flame front instabilities. This technique allows the visualization of OH radicals which are an intermediate species of the hydrogen oxidation and can be used as a marker of the flame front [63]. The main advantage of the OH-PLIF technique versus shadowgraphy is that there is no line-of-sight integration in the resulting pictures due to the planar laser sheet. This planar laser sheet allows the excitation of the OH radicals in a defined thin plane. The results are two-dimensional slices allowing measurement of the flame front length in this plane.

It must be emphasized that depending on the optical measurement technique and the chosen resolution, the field of view changes in x-direction and therefore does not match the full width of the optically accessible area of 0.23 m. The field of view in the present work was chosen for both optical measurement techniques to approximately 0.16 m.

4 Highly resolved simulations

In addition to experimental investigations, highly resolved simulations of the investigated problem are conducted to gain more insight into the small-scale wrinkling processes [52]. The two-dimensional simulations complement the experimental data and allow to investigate the flame wrinkling process at a higher resolution and under varying pressure.

4.1 Numerical setup

The open-source CFD package OpenFOAM [112] is used to solve the set of equations in a finite-volume framework. Unsteady compressible Navier-Stokes equations with detailed chemistry are solved. To compute the unsteady local composition of the multi-component mixture, $N-1$ transport equations are solved for the mass fractions Y_k of N species. Y_N (excess species nitrogen here) finally results from the fact that all mass fractions must sum up to unity. Linking the velocity gradients in the momentum equations to the resulting shear stress, the dynamic viscosity μ is obtained from Sutherland's formula [113] and other molecular transport properties like individual species diffusivities $D_k = \mu/(\mathrm{Sc}_k \rho)$ are derived therefrom. Mixture heat conductivity λ is calculated by Eucken's formula [90].

Because of its wide validation range (pressure from 0.05 to 87 atm, temperature from 298 to 2700 K and equivalence ratio from 0.2 to 6), the chemical source term $\dot{\omega}_k$ is calculated by means of Ó Conaire's detailed mechanism [84]. The original scheme, consisting of 9 species and 19 reversible elementary reactions is extended for the excited hydroxyl molecule OH^* following Kathrotia et al. [57]. In the context of this study, it is important to note that Arrhenius rate coefficients are only depending on temperature. However, pressure implicitly influences the reaction

rate via the concentration of involved species. Since gas-dynamic effects like shock waves do not play a role in this investigation, robust pressure-velocity coupling is realized by the Merged PISO-SIMPLE (PIMPLE) algorithm which is optimized for unsteady problems. Spatial discretization is second-order accurate for both convective and diffusive fluxes. Dynamic time-stepping with a maximum Courant number of 0.1 assures a stable and sufficiently accurate temporal discretization. Chemical source terms are linearized to avoid issues related to stiff Arrhenius chemistry. Closure of the governing equations for small-scale effects is unnecessary since all relevant scales are resolved. Thermal spark plug ignition is modeled by patching adiabatic flame temperature and chemical equilibrium mixture composition around the ignition kernel with a radius of 2.5 mm. Initial temperature is assumed to be 293 K. No-slip adiabatic walls are imposed at all boundaries.

To save computational power a rectangular two-dimensional domain is used in the calculations. Additionally, computational power is saved by setting the length of the computational domain to 0.325 m, approximately two times the length of the optically accessible area of the channel. According to Altantzis et al. [3] and Frouzakis et al. [42] the cellular structure of the flame front also depends on the ratio of the domain height and flame thickness. Therefore, to achieve the highest comparability with the experimental results, the height of the computational domain in this work is chosen to be 0.06 m, corresponding to the full height of the explosion channel.

A grid sensitivity study was conducted to ensure a sufficient resolution of the flame front structure. A structured grid with 12.19 million cells (40 μm cell size) was found to resolve the flame structure sufficiently. With this setup the flame structure was resolved by at least 10 cells even in the highest pressure case with the thinnest flame front as demonstrated in Fig. 4.1, resulting in DNS-like highly resolved simulations. Using a uniform grid spacing of $\Delta x = 40$ μm, the number of in-flame cells $\delta_B / \Delta x$ drops approximately from 20 to 12 in the relevant evaluated range of this study from $p = 0.5$ bar to $p = 8$ bar. In-flame phenomena and related two-dimensional flame stretch effects, due to front curvature and tangential strain, are thus naturally included in the simulation. Follow-

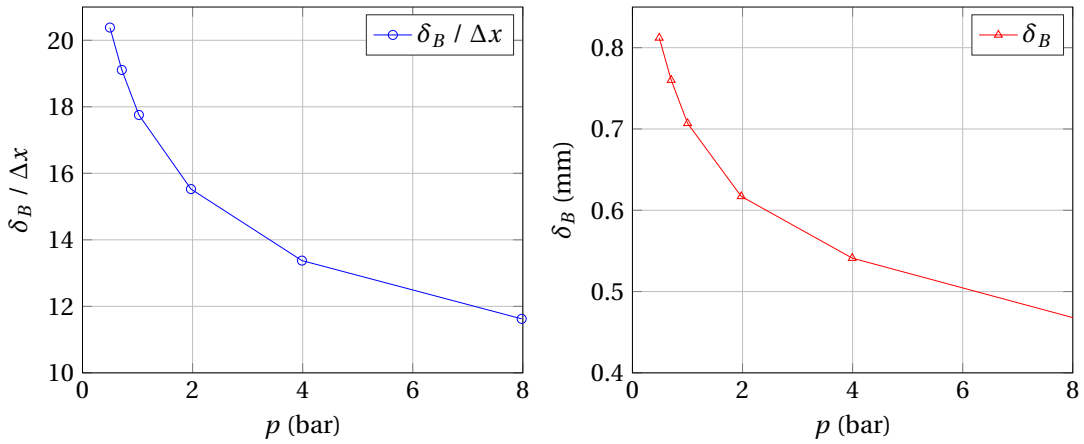

Figure 4.1: On the left: pressure dependency of flame thickness δ_B following Blint [10] for a hydrogen concentration of $X_{\mathrm{H2}} = 13\%$; On the right: the corresponding number of in-flame cells for a computational grid resolution of $\Delta x = 40$ μm.

ing Poinsot and Veynante [89], the flame thickness in Eq. 2.8 according to Blint [10] is known for its good a-priori predictions. Here, $\delta_Z = a_u / s_l$ denotes the Zeldovich or diffusion thickness in which the effect of pressure is accounted for both the laminar burning velocity s_l as well as the thermal diffusivity of the unburned mixture a_u. Evaluation of the thermal flame thickness from Eq. 2.3 from one-dimensional flame profile calculations in CANTERA [46] resulted in consistently larger values of δ (i.e. less conservative) and is therefore not used for the assessment of grid resolution.

The resolution of turbulence is incorporated in principle but not necessarily correct in a quantitative way. In general, turbulence-resolving simulations are not meaningful in two-dimensional domains, since vortex stretching does not exist in two-dimensional space. Fortunately, turbulence seems to be of inferior importance in the investigated problem. This assumption is especially valid since no turbulence-inducing obstacles are installed in the channel. The Kolmogorov dissipation scales are consequently not considered for the resolution requirement. Table 4.1 summarizes the numerically investigated cases at a hydrogen concentration of 13%.

Table 4.1: Case overview of highly resolved simulations. n denotes the number of computational cells in the particular simulation.

No.	X_{H2} (%)	p^0 (bar)	$n(\cdot 10^6)$
1 (ref.)	13	1.01	12.19
2	13	1.01	7.8
3	13	1.01	21.67
5	13	0.5	12.19
6	13	0.7	12.19
7	13	2.0	12.19

4.2 Numerically obtained flame fronts

Due to the amount of data accompanied by the highly resolved simulations, only snapshots have been saved and evaluated for each case. As an example Fig. 4.2 shows flame surfaces at different times evaluated from DNS for $X_{H2} = 13\,\%$ and an initial pressure level of $p^0 = 0.7$ bar. The flame surfaces were defined as $T = 800$ K contour lines, representing roughly the average between the unburned and burned gas temperature. The entire simulated domain is depicted. The ignition position was chosen corresponding to the experiments and the flame propagates from left to right.

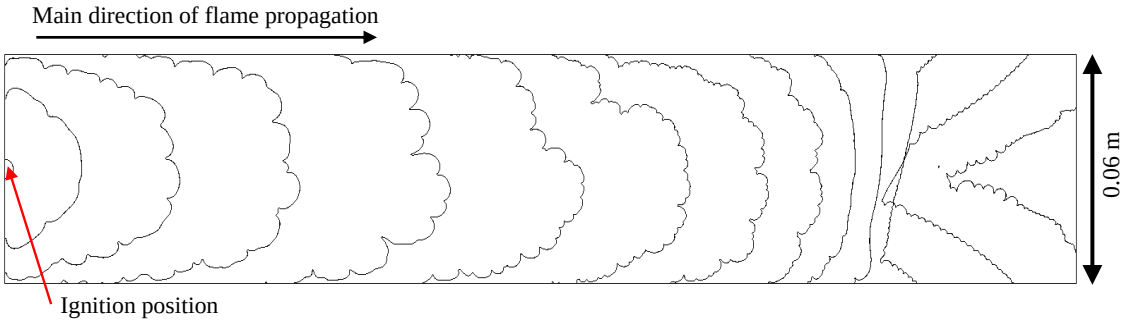

Figure 4.2: Simulated flame surfaces at different time steps for a hydrogen concentration of 13 % at an initial pressure level of 0.7 bar. Flame propagates from left to right.

As expected, it can be observed that the flame surface develops a characteristic flame surface structure due to intrinsic instability mechanisms. Furthermore, it can be seen that the macroscopic flame shape is similar

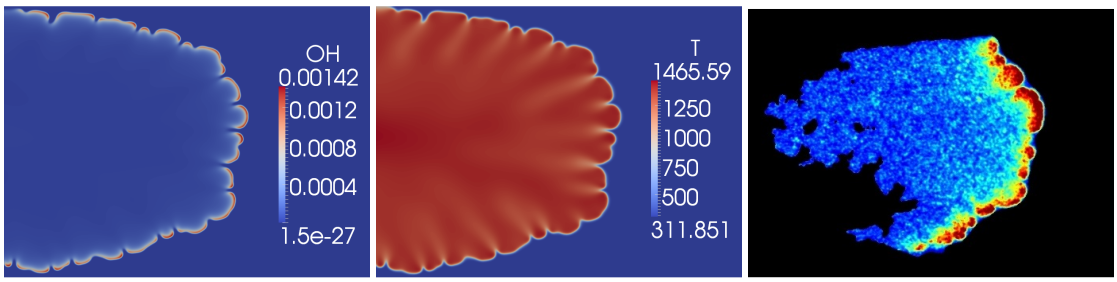

Figure 4.3: Qualitative comparison between the highly resolved simulations (left and center) and an experimental OH-PLIF image (right) for the identical concentration of 13% and an initial pressure of 1 bar.

to the flame structure in the experiments as described in Fig. 6.3. Due to the increasing pressure during the simulation, smaller flame wrinkles can be observed in the rear part of the domain, where the pressure experiences a significant increase. This behavior indicates that with increasing pressure the length scale at which wrinkles on the flame surface are developing, is continuously decreasing until eventually the flame surface becomes smooth again. In the last stages of flame propagation, a tulip flame phenomenon can occur. The flame surfaces in this stage are not used for further evaluation.

Good qualitative agreement with the experiment is evident from Fig. 4.3. Partial extinction in concave sections due to hydrogen deficiency is well reproduced by the simulation. This behavior manifests in the characteristic lower-temperature regions originating from the concave sections. Temperature in convex sections is clearly above the adiabatic flame temperature. Due to the negligence of heat losses, wall quenching is not included in the simulation. The bulk flame structure should be largely unaffected though. Qualitative and quantitative comparison of computed OH and OH^* fields is further insightful. The latter quantity can be interpreted as an indirect measure of heat release.

5 Data evaluation

For the determination of the wrinkled flame surface length L_{wrink} and the construction of the smooth flame surface length L_{smooth} an automated Matlab routine is used. Based on the work of Finke [40], an evaluation procedure is developed to account for the characteristics of the investigated problem [38]. The routine is based on the binarization of raw images obtained through the OH-PLIF technique and the highly resolved simulations. The main idea behind the evaluation process is to detect the flame surface area enlargement due to the microscopic flame surface wrinkling. Therefore, the real wrinkled flame surface length must be compared to a hypothetical smooth flame surface length, where the microscopic wrinkling is filtered. The macroscopic flame shape must be reproduced by the hypothetical smooth flame surface. That way the effect of small-scale wrinkling is isolated from macroscopic flame shape changes. Fig. 5.2 shows a detailed view of the detected flame front L_{wrink} in an OH-PLIF image and the constructed macroscopic flame front L_{smooth}. The single steps of the evaluation procedure are discussed in the following sections 5.1 and 5.2.

For both evaluated data sets (experimental and numerical) the identical evaluation procedure is used. That way, the highest degree of comparability of the results could be achieved. Fig. 5.1 summarizes the developed and applied evaluation process. The flame surface lengths obtained through the simulation are based on temperature contour plots which are assumed to represent the flame front itself.

5.1 Detection of wrinkled flame surface

In order to detect the real wrinkled flame surface in the OH-PLIF images and to determine the length of the wrinkled flame front, the following

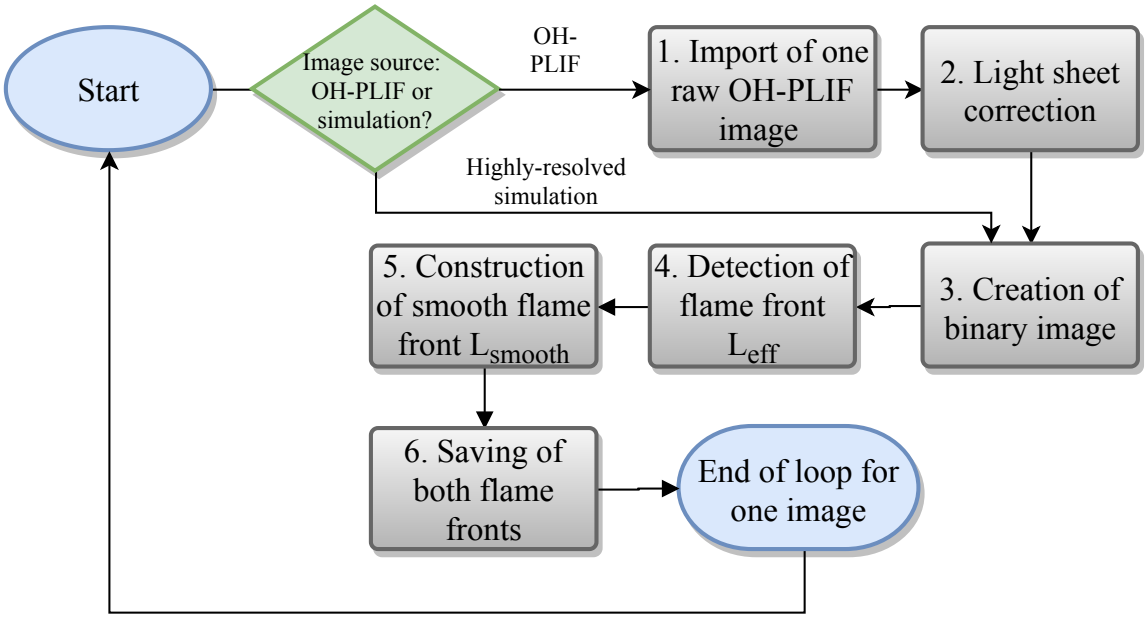

Figure 5.1: Overview over the data evaluation process conducted for every OH-PLIF image and flame contour plots from highly resolved simulations.

steps must be executed [58] [59]:

- Step 1: One raw grey-scale 8 bit OH-PLIF image is loaded into the evaluation routine.
- Step 2: A light sheet correction is conducted due to non-uniform distribution of the laser light intensity along the vertical direction of the laser light sheet. After this procedure, the images exhibit equal intensities of the OH-PLIF signal along the flame surface. Additionally, the 10° malposition of camera SAX2 in relation to the channel center line as shown in Fig. 3.8 is corrected.
- Step 3: Binarization of the image is executed where all pixels below a threshold value are set to 0 (black) and all pixels above this limit value are set to 255 (white). The threshold value is dynamically chosen by the routine itself based on the brightness of the currently processed image. This step is also executed for the wrinkled flame fronts from the highly resolved simulations.

- Step 4: This step leads to an image with white "spots". Spots belonging to the flame surface are connected and the side facing the fresh mixture is detected. This surface represents the wrinkled flame surface.

5.2 Construction of smooth flame surface

The construction of the smooth flame surface is based on filtering of the detected wrinkled flame surface. That way, only the surface length caused by the macroscopic shape of the convex flame is captured. Step 5 shown in Fig. 5.1 is separated into steps 5a to 5e and consists of the following:

- Step 5a: Creation of a new binary image: the starting point is the previously detected real flame surface (L_{wrink}) or the flame contour line from the simulations. Both surfaces are separating the burned and the unburned gas. With the flame moving from left to right all pixels left of the detected flame surface represent the burned gas and all pixels right to it, the unburned. A binary image is created, setting the burned gas to a value of 1 and the unburned gas to a value of 0.
- Step 5b: Generation of the filter grid: in the next step a grid is generated, dividing the image into quadratic cells (grid lines depicted in Fig. 5.2). The cell size, which represents the filter size, must be large enough so it does not detect the small-scale wrinkling of the flame surface. In the conducted work the selected reference cell size was 7.5 mm. A detailed discussion of the influence of this variable on the results will be given in Sec. 6.5.
- Step 5c: Determination of the amount of burned gas in each cell: If a cell contains solely burned (unburned) gas a value of $c = 1$ ($c = 0$) is assigned to the cell (numbers in cells in Fig. 5.2). For cells containing the flame surface, a number between $c = 0$ and $c = 1$ is calculated based on the ratio of burned pixels to all pixels contained by the cell.

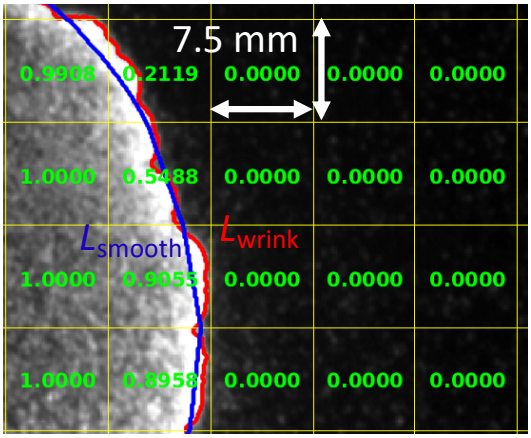

Figure 5.2: OH-PLIF image with detected wrinkled (L_{wrink}) and smooth (L_{smooth}) flame surfaces. Additionally, the filter utilized grid and the volume fraction of burned gas in each cell are depicted (0: unburned; 1: burned; a value between 0 and 1 means the cell is partially burned and therefore contains the flame surface).

- Step 5d: Calculation of values at the grid corners in cells with values between $c = 0$ and $c = 1$: the determination of the smooth flame surface is based on construction of an isoline in each cell at a value of $c = 0.5$. For this purpose the values at the grid corners (red dots in middle part of Fig. 5.4) must be calculated. First, a shifted grid (blue grid in left part of Fig. 5.4) is created. The values at the corners of this new grid are known. Now, an interpolating procedure is executed to determine the unknown corner values of the original grid. A grid cell is defined through two parameters: s and t, each defined from 0 to 1. Each corner is numbered from $i = 1$ to $i = 4$. The influence of an c-value saved at a specific corner on an arbitrary value inside the cell is represented through the following functions

$$N_1(s,t) = (1-s)\cdot(1-t) \tag{5.1}$$

$$N_2(s,t) = s\cdot(1-t) \tag{5.2}$$

$$N_3(s,t) = s\cdot t \tag{5.3}$$

$$N_4(s,t) = (1-s)\cdot t \tag{5.4}$$

with the properties

$$\sum_{i=1}^{4} N_i(s,t) = 1 \tag{5.5}$$

and

$$N_i\big|_j = \begin{cases} 1, & \text{for } i = j \\ 0, & \text{for } i \neq j \end{cases} \tag{5.6}$$

which determines the influence of the value at the corner i on the value at the corner j. When all values at the corners are known, all values inside the cell can be calculated utilizing:

$$c(s,t) = \sum_{i=1}^{4} N_i(s,t) \cdot c_i \tag{5.7}$$

with c_i being the known c-values at the four corners of the grid. Figure 5.3 shows a cell with an interpolated continuous c distribution across the cell area. The desired values at the corners of the original grid can now easily be calculated by evaluating the c-value at $s = 0.5$ and $t = 0.5$ (cell center).

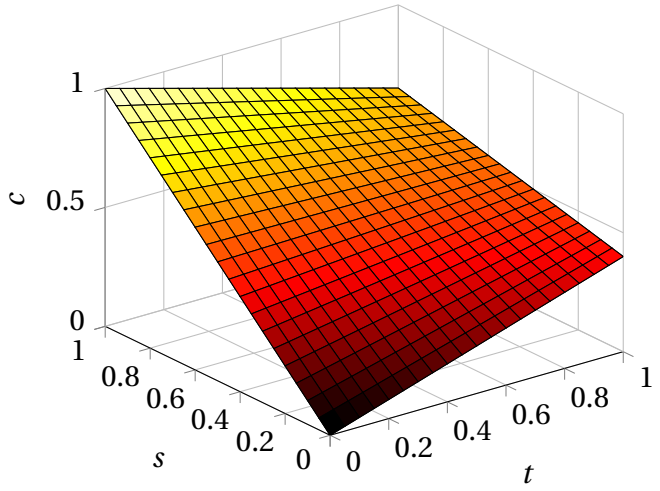

Figure 5.3: Distribution of local c-values inside a grid cell calculated from the known corner values.

- Step 5e: Construction of the smooth flame surface: with the now known values at the corner of the original grid, the same procedure

as described in the prior step is conducted in the original cell. Finally, the smooth flame surface can be interpolated as an isoline with at the value $c = 0.5$ (right part of Fig. 5.4).

Figure 5.4: Left: shifted blue grid with known corner values. Middle: interpolated values at the corners of the original grid. Right: Interpolation of the smooth flame surface from the known corner values as the isoline with a value of $c = 0.5$. Depiction adapted from [38].

- Step 6: Saving of the constructed smooth flame surface and employing the procedure in the next cell where the average c-value is between 0 and 1.

This procedure is executed for all cells with c-values between 0 and 1 until all cells of an image are processed. After that, the routine proceeds with the next image.

6 Model formulation

The modeling approach in this work is pursuing the idea of a multi-phenomena combustion model, based on the separation of accelerating effects [95] [115]. The basis for the new modeling concept is the connection of the flame surface area with the burning velocity shown in Eq. 2.41, which expands and adapts the concept of the increasing turbulent burning velocity due to flame surface area enlargement. This original formulation only contemplates the flame surface area enlargement due to turbulence, but here more effects are examined that have an impact on flame acceleration.

The unclosed source term in Eq. 2.39 is closed by the algebraic formulation in Eq. 6.2. This approach allows for a simple incorporation of experimental results in the modeling process. In the suggested modeling approach Eq. 2.41 is successively extended. Based on this procedure, the resulting burning velocity in Eq. 6.2 will be referenced to as an "effective burning velocity" summarizing all accelerating effects:

$$s_{\mathrm{eff}} = s_t \tag{6.1}$$

The resulting burning law reads as follows:

$$s_{\mathrm{eff}} = \underbrace{\Xi_{\mathrm{wrink}}}_{\text{1.}} \cdot \underbrace{F_p}_{\text{2.}} \cdot \underbrace{s_{\mathrm{l,0,ref}}}_{\text{3.}} \cdot \underbrace{F_{\mathrm{Thermo}}}_{\text{4.}} \cdot \underbrace{F_s}_{\text{5.}} \cdot \underbrace{F_\Delta}_{\text{6.}} \cdot \underbrace{F_t}_{\text{7.}} \cdot \underbrace{B}_{\text{8.}} \tag{6.2}$$

combining the following effects:

1. Flame surface area enlargement due to small-scale flame front wrinkling caused by flame instabilities.

2. Pressure effect on flame surface area enlargement due to small-scale flame front wrinkling.
3. Laminar unstretched burning velocity as the basis of the model.
4. Effect of pressure and temperature on laminar burning velocity.
5. Influence of local flame front curvature and the resulting stretch on laminar burning velocity.
6. Treatment of computational grid size effect.
7. Turbulence influence.
8. Test facility specific effect caused by flame containment.

An important assumption is that the accelerating effects do not cross-correlate in this modeling approach. This means that if two or more effects accelerate the flame front, they do not influence each other. This assumption is important to limit the level of complexity. The advantage of the mathematical structure in this modeling approach is a robust behavior in the case of a nonexistent effect. In that case the affected factor approaches a value of unity and has no accelerating effect on the propagating flame front. Additionally, Eq. 6.2 can be expanded by more accelerating effects in the future.

In the subsequent sections the modeling approach and the specific formulation of the factors in Eq. 6.2 will be presented and discussed.

6.1 Flame surface enlargement: Ξ_{wrink}

Following Eq. 2.41 the factor Ξ_{wrink} can be calculated through surface area comparison of the wrinkled and the smooth flame front. As already observed in Fig. 1.1 and shown in Fig. 5.2, it is feasible to qualitatively and quantitatively evaluate the obtained experimental data.

In Fig. 6.1 the velocity of the propagating flame front is plotted over the distance for two different lean hydrogen-air concentrations. The flame

front velocities u_F are increasing in both cases mainly due to macroscopic flame surface area enlargement through the growing flame kernel itself. Additionally, as observed in Fig. 1.1, small-scale flame surface wrinkling occurs in lean hydrogen-air flames due to intrinsic instability mechanisms and leads to an enlargement of the flame surface area. The influence of these macroscopic and microscopic effects on flame acceleration is superimposed. In simulations on coarse grids the effect of small-scale wrinkling on flame surface area enlargement cannot be resolved and has to be modeled. For this purpose both effects have to be separated to capture the sole effect of microscopic flame front wrinkling due to intrinsic instabilities.

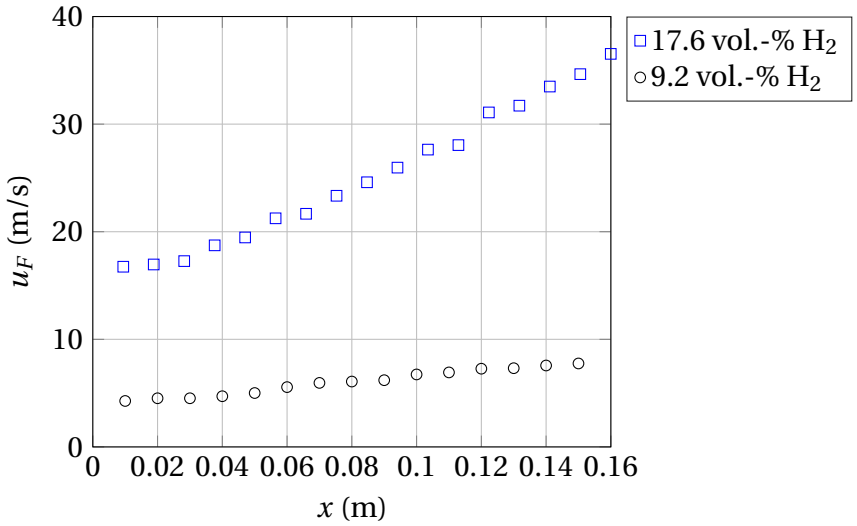

Figure 6.1: Velocity of the flame front over distance determined from OH-PLIF recordings.

Figure 6.2 shows the temporal development of flame surface area obtained from OH-PLIF measurements. The wrinkled flame surface length L_{wrink} and the smooth flame surface length L_{smooth} are plotted over time. The hydrogen-air concentration corresponding to this plot is 13 % H_2. Additionally, a filtered signal for both flame fronts is depicted to facilitate the interpretation of the results. The filtered signal is obtained through a 6^{th}-order Savitzki-Golay filter [96].

As expected, the wrinkled flame front L_{wrink} develops a larger surface area than the smooth flame front L_{smooth}. Both curves show the same tendency, namely at first an increase in time, then they reach a peak value

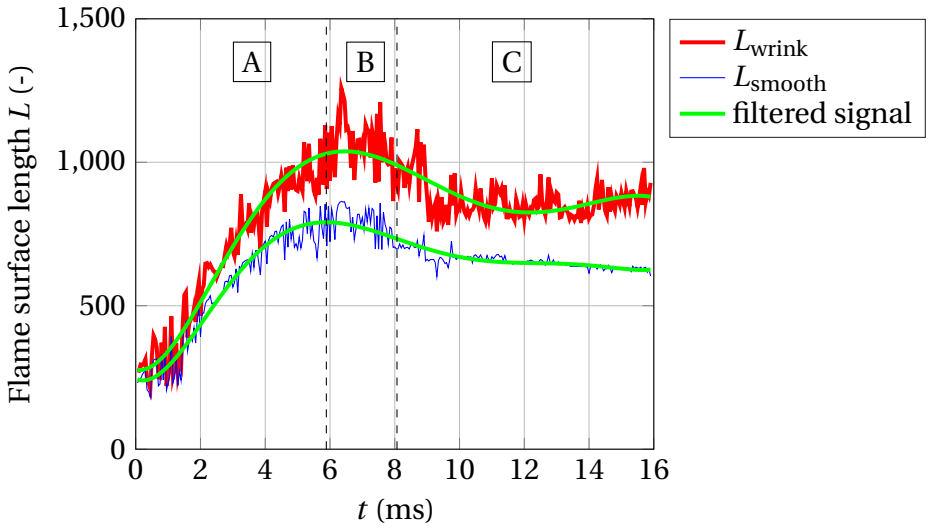

Figure 6.2: Development of smooth and wrinkled flame front lengths over time corresponding to a hydrogen-air mixture of 13% H_2.

and decrease again until they seem to reach a stationary level and finally exit the optically accessible area of the test facility.

This behavior is observed in all of the evaluated data and can be explained as follows: Shortly after ignition, a hemispherical flame kernel occurs, showing no flame front wrinkling. This explains why two flame front lengths are small compared to subsequent times. After this, the mean flame kernel grows until its maximum vertical extent is reached. At that time, the flame kernel diameter reaches the channel height and the curves reach their peak values. The decrease of the flame front lengths corresponds to the flattening of both flame fronts due to the decrease in curvature of the flame front with increasing flame radii. Finally, the flame propagates through the channel at a constant macroscopic flame shape. Based on these observations, the development of the flame front length can be divided in three regimes.

An experimentally observed flame propagation process corresponding to a mixture with a concentration of 9.2 % H_2 is presented in Fig. 6.3. Shown is the temporal development of the wrinkled flame front L_{wrink}. The ignition occurs at the left channel wall and the flame expands hemispherically until it reaches the channels top and bottom walls. This first regime can be considered a “development regime” marked as “A”. After

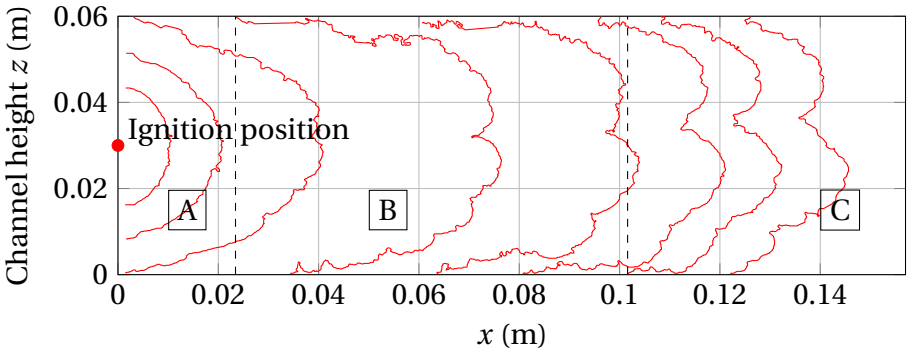

Figure 6.3: Flame propagation process divided into three stages. Solid line corresponds to an experimentally determined flame front L_{wrink} of a 9.2 % H_2 mixture at various times.

this development stage, the macroscopic flame front curvature decreases and the flame flattens until it reaches a shape at constant macroscopic curvature. This regime can be considered a “flattening regime”, marked as “B”. Finally, the last stage can be considered a “propagation regime”, denoted as “C”, where the flame propagates through the channel without major changes in macroscopic flame shape.

The classification into these regimes describes the early stage of flame propagation in a rectangular explosion channel, where the flame front has not reached the lateral walls (quartz glass windows) yet and the influence of the end plate is still negligible.

These regimes can be associated with the curves of the flame front lengths in Fig. 6.2. Each regime is separated by a vertical black dashed line. The position of the first dashed line, separating regime A and B, is corresponding to the moment when the flame front reaches the channels top and bottom walls and exhibits its maximum flame surface area. Hence, the position of the peak value of the smooth flame front length was chosen as the transition position from regime A to B. As the transition position from regime B to C, the inflection point of the filtered curve of the smooth flame front length was chosen. The reason for this procedure is the assumption that at this position the flame front starts to reach its final macroscopic curved shape due to remaining global curvature. Additionally, the inflection point is mathematically well-defined and can be captured easily.

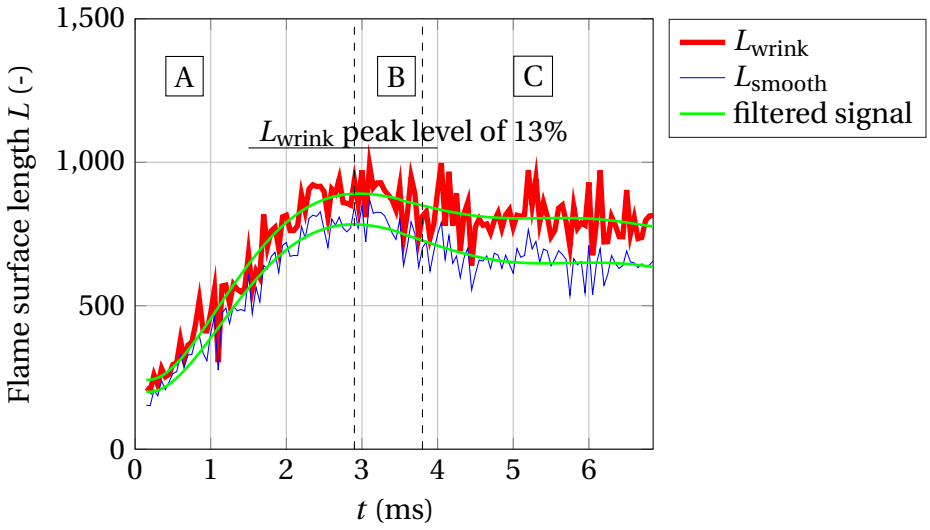

Figure 6.4: Development of flame front lengths over time corresponding to a hydrogen-air mixture of 19 % H_2. At 7 ms the flame front has left the visibility range of the camera at approximately x = 0.16 m.

The influence of flame front instabilities should vanish with higher hydrogen concentrations and the quantitative acquisition of this change is crucial for the modeling process. For this purpose, flame front lengths corresponding to a richer hydrogen-air mixture than 13 % H_2, namely 19 % H_2, are depicted in Fig. 6.4. By comparing Fig. 6.2 and Fig. 6.4 it is evident that the curve shapes are qualitatively similar. All previously discussed regimes (A, B and C) can also be identified in this plot. The curve corresponding to the smooth flame front length L_{smooth} in Fig. 6.4 shows approximately the same peak level as the respective curve in Fig. 6.2. This behavior was expected due to the identical channel geometry. The wrinkled flame front length L_{wrink} shows a noticeable deviation compared to that in Fig. 6.2. This detected decrease in L_{wrink} is due to the decreasing effect of small-scale flame front wrinkling with higher hydrogen concentrations in lean mixtures.

Following the definition in Eq. 6.3 the wrinkling factor Ξ_{2D} can be calculated in every single time step for all investigated concentrations. Fig. 6.5 shows the calculated wrinkling factor plotted over time for a hydrogen-air concentration of 13%.

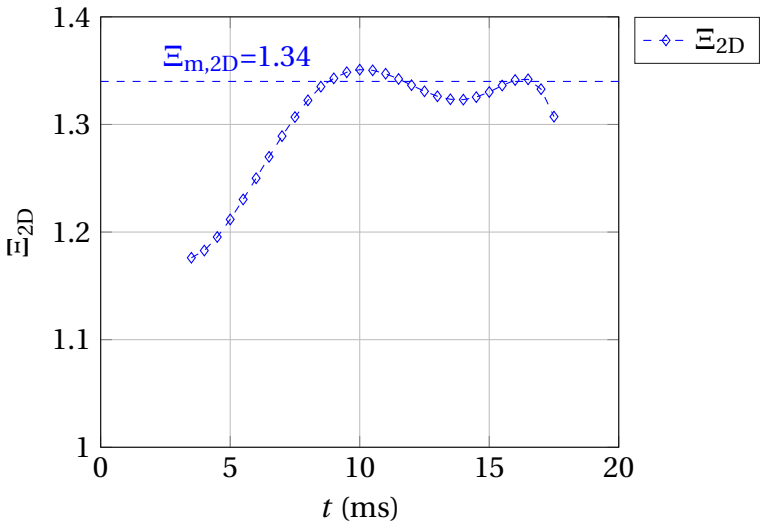

Figure 6.5: Development of the wrinkling factor over time for three different hydrogen-air mixtures and corresponding calculated mean wrinkling factors in regime C.

$$\Xi_{2D} = \frac{L_{\text{wrink}}}{L_{\text{smooth}}} \tag{6.3}$$

Since the OH-PLIF technique is a two-dimensional measurement technique, the calculated wrinkling factors are two-dimensional. The value of the mean two-dimensional wrinkling factor $\Xi_{m,2D}$ is also depicted in Fig. 6.5 and was calculated as a time average of Ξ in the propagating regime (regime C in Fig. 6.2 and Fig. 6.4):

$$\Xi_{m,2D} = \frac{L_{\text{wrink,C}}}{L_{\text{smooth,C}}} \tag{6.4}$$

The reason for this definition is that regime C seems to be most significant in characterizing flame propagation in the investigated experimental facility because the value seems to reach a constant level. In this regime the flame seems to propagate without considerably altering its macroscopic flame front shape.

The evaluation procedure was applied to all experimental data and a two-dimensional mean wrinkling factor $\Xi_{m,2D}$ was calculated for every considered hydrogen-air mixture. The experimental data ranges from

6 % H_2 to 23 % H_2 and the results are plotted in Fig. 6.6. As expected, the mean wrinkling factors associated with the leanest hydrogen-air mixtures show the highest values of $\Xi_{m,2D}$. The richer the lean mixture, the smaller the value for $\Xi_{m,2D}$.

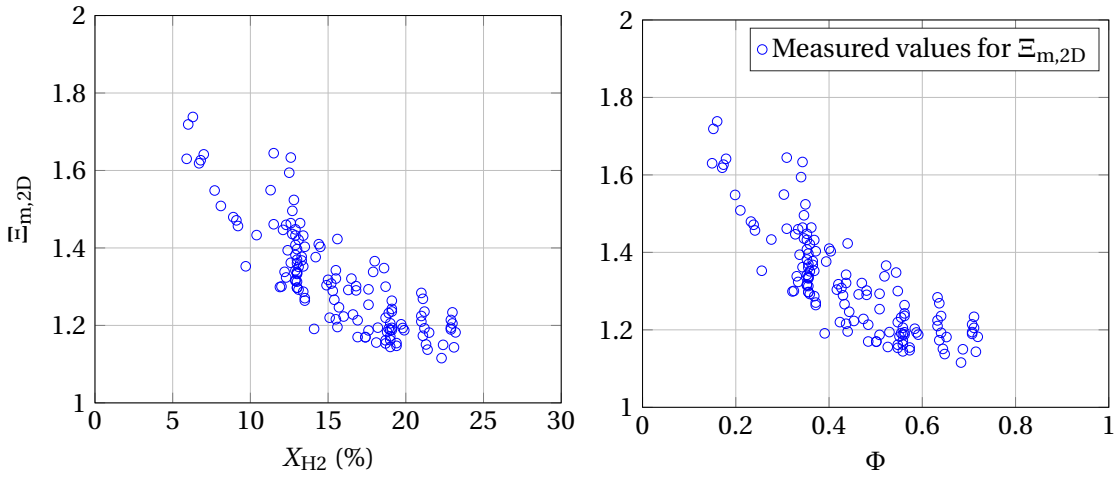

Figure 6.6: Mean two-dimensional wrinkling factors plotted over hydrogen-air concentration.

The purpose of this experimental work and the evaluation of the data is to improve combustion modeling for CFD simulations, taking flame front instabilities into account. Hence, the experimental results have to be associated with a quantity that is accessible in CFD simulations. Following the accepted theory of the formation of thermal-diffusive instabilities in lean hydrogen-air mixtures an effective Lewis number of the mixture $Le_{eff} < 1$ correlates with the occurrence of flame front wrinkling. This variable qualifies as a parameter describing the effect of flame front instabilities as a function of the mixture composition. It can be readily incorporated into numerical models. However, the Lewis number is a quantity defined as a property for one single species and not for a mixture. Hence, the effective Lewis number of the hydrogen-air mixture was calculated as proposed by Bechtold et al. [9] and summarized by Hoferichter et al. [54]. The effective Lewis number in this work defines as follows:

$$Le_{eff} = 1 + \frac{Le_E - 1 + B(Le_D - 1)}{1 + B} \tag{6.5}$$

$$B = 1 + \text{Ze}\left(\frac{1}{\Phi} - 1\right) \tag{6.6}$$

$$B = 1 + \text{Ze}\,(\Phi - 1) \tag{6.7}$$

$$\text{Ze} = \frac{E(T_{\text{ad}} - T_u)}{RT_{\text{ad}}^2} \tag{6.8}$$

The global activation energy E was chosen in this work to $E = 30\,\text{kcal/mol}$ following [102].

Figure 6.7 shows the relationship between the effective Lewis number and the mixture concentration on the left and the equivalence ratio on the right. It can be observed that in the near stoichiometric mixture the effective Lewis number is approaching unity, suggesting that in this concentration range flame wrinkling has a negligible effect in the initial propagation phase.

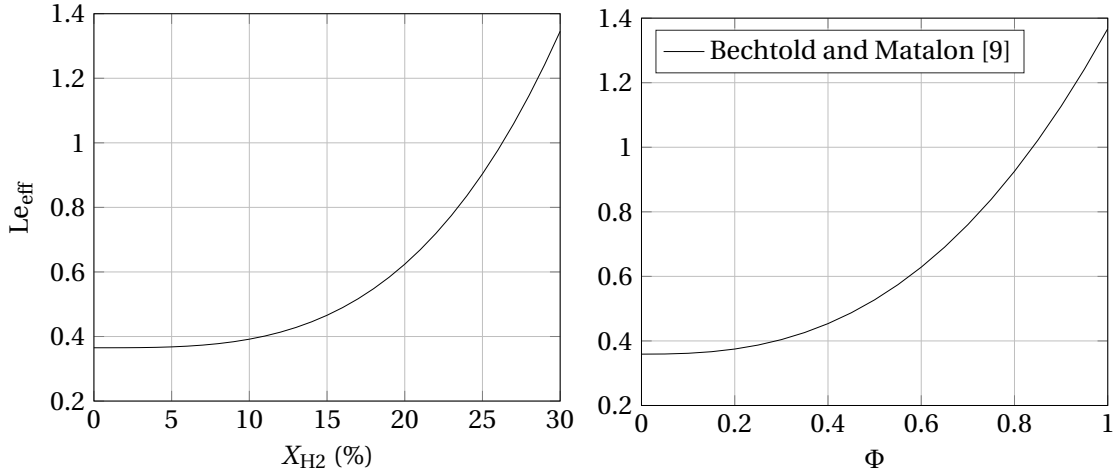

Figure 6.7: Effective Lewis numbers over varying concentration and equivalence ratio following Bechtold and Matalon [9] (Eq. 6.5).

The accelerating effect of flame surface enlargement is three-dimensional, which is why the two-dimensional factors have to be extended by the third dimension [71]. The current experimental setup does not allow measurements of these factors perpendicular to the

vertical plane. Therefore assumptions have to be made and the effects of the third dimension have to be included by modeling. Based on the observation that the flame surfaces in Fig. 6.9 indicate no preferred direction of wrinkling development, wrinkling of the flame surface is assumed to be identical in both directions which can be expressed with the following formulation, which was also suggested by Driscoll [37]:

$$\Xi_{\text{m,3D}} = \Xi_{\text{m,2D}}^{2}. \tag{6.9}$$

In Fig. 6.8, the two-dimensional mean wrinkling factors are plotted over the effective Lewis number of the mixture. The trend of the experimental data correlates with the theory of flame front instabilities, where the influence of flame front wrinkling should vanish in the initial phase around an effective Lewis number of unity. In addition to the experimental data a fitted and extrapolated curve is shown.

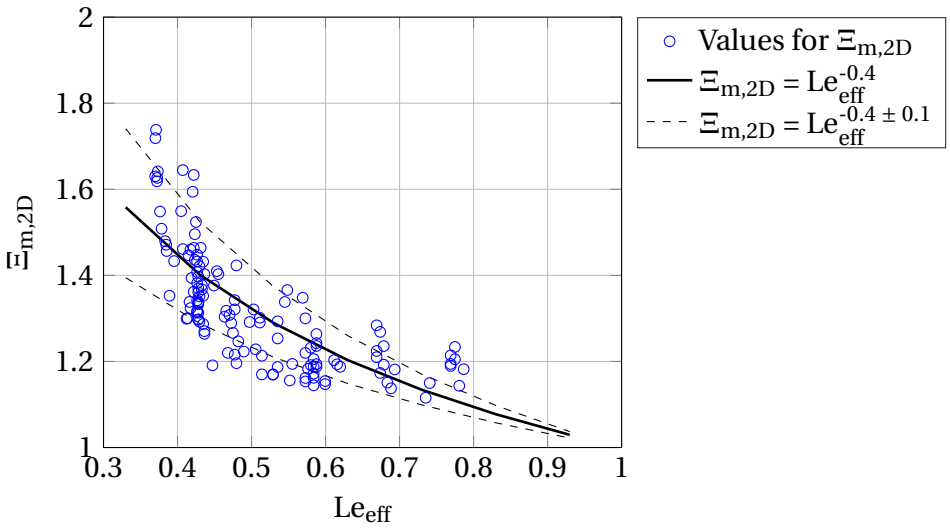

Figure 6.8: Mean two-dimensional wrinkling factor plotted over effective Lewis number of hydrogen-air mixture with a fitted solid curve showing the trend. The dashed lines indicate a variation of the exponent by ±0.1.

Finally, the developed burning law in this work based on Eq. 2.41 reads:

$$\Xi_{\text{wrink}} = \Xi_{\text{m,3D}} = \left(\text{Le}_{\text{eff}}^{-0.4}\right)^{2} \tag{6.10}$$

This correlation shows a robust behavior within the applicability range from $\mathrm{Le}_{\mathrm{eff}} = 0.35$ to $\mathrm{Le}_{\mathrm{eff}} = 0.77$.

6.2 Pressure influence on flame surface enlargement: F_p

The goal of this section is to quantitatively determine the increase of flame surface area due to variation of pressure. When the flame front propagates into the fresh mixture, it preconditions the fresh gases and the pressure is increasing. Eq. 6.11 defines the factor F_p as the ratio of the three-dimensional flame surface enlargement factor under pressure influence and the reference flame surface enlargement factor at 1 bar.

$$F_p = \frac{\Xi_{\mathrm{wrink,p}}}{\Xi_{\mathrm{wrink}}} \tag{6.11}$$

To meet this goal OH-PLIF data under variation of the initial pressure and simulation data under pressure build-up are investigated [60]. For both investigated data sets (experimental and numerical) the identical evaluation method described in section 5 is used. That way, the highest degree of comparability of results can be achieved between these two fundamentally different approaches.

In Fig. 6.9 shadowgraph images of lean hydrogen-air flames are compared with each other. The hydrogen concentration in all three cases is 13% and the images are taken at similar distances of the flame tip from the ignition position. The mixture is ignited through a spark plug at the position $(x, y, z) = 0$. The images show that each flame develops a wrinkled flame surface with varying length scales of the cellular structure. Due to the negligible turbulence level of the mixture prior to ignition, wrinkling of the flame surface is assumed to be mainly caused by intrinsic flame instabilities like the hydrodynamic or Landau-Darrieus instability [68] and the thermal-diffusive instability [74] under the influence of stretch. The comparison shows that the intensity of flame surface wrinkling increases with initial pressure p^0, an effect that was already observed in the past e.g., by [18], [19], [48] or [50]. However, following Warnatz et al. [111], the flame surface area is not necessarily increasing with

a decreasing length scale of the cellular structure.

Although Fig. 6.9 is clearly showing the effect of pressure on the propagating flame surface, namely the decrease of cell size, the data cannot be evaluated quantitatively because of the inherent line-of-sight integration of the shadowgraph technique.

To overcome this problem, planar OH-PLIF measurements have been conducted for the corresponding DNS cases 1, 6 and 7, summarized in Tab. 4.1. Figure 6.10 compares the post-processed OH-PLIF recordings for these cases. The mixture is ignited at the left boundary of the image and the flame propagates from left to right. The images are taken at a similar distance from the ignition position. It can be observed that all three flames develop a wrinkled flame surface structure with convex shaped parts towards the fresh mixture ahead of the flame front. This structure alters under variation of the initial pressure level p^0. The pressure rise in the experiment while the flame passes the optically accessible initial part of the channel ($\approx$ 12% of the overall channel length) has been checked for all investigated cases. Evaluating the pressure transducers it was found that even in the $p^0 = 2$ bar case the pressure rise during this initial phase is negligible. The pressure starts increasing after the flame front passed this initial part of the channel and therefore the detected flame surface enlargement in the experiment can be linked directly to the initial pressure level.

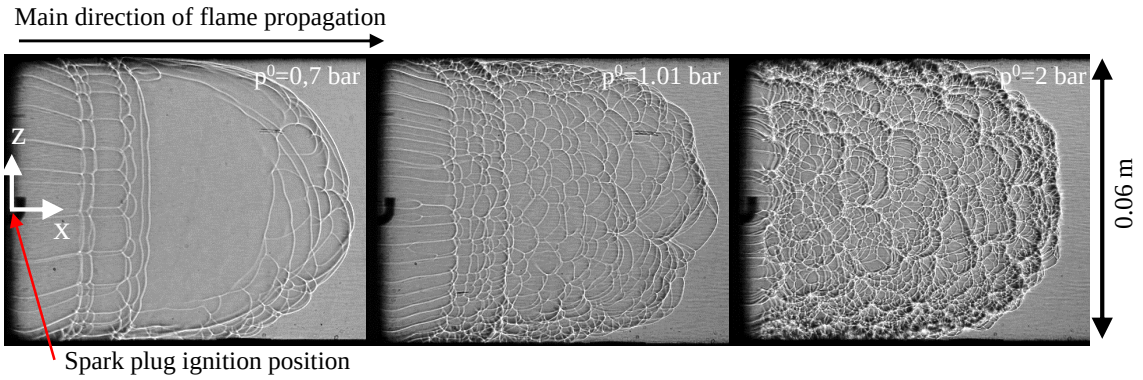

Figure 6.9: Shadowgraphy images of hydrogen-air flames with a hydrogen concentration of 13% propagating from left to right under variation of initial pressure p^0. The images were taken at similar distances of the flame tip from the ignition position.

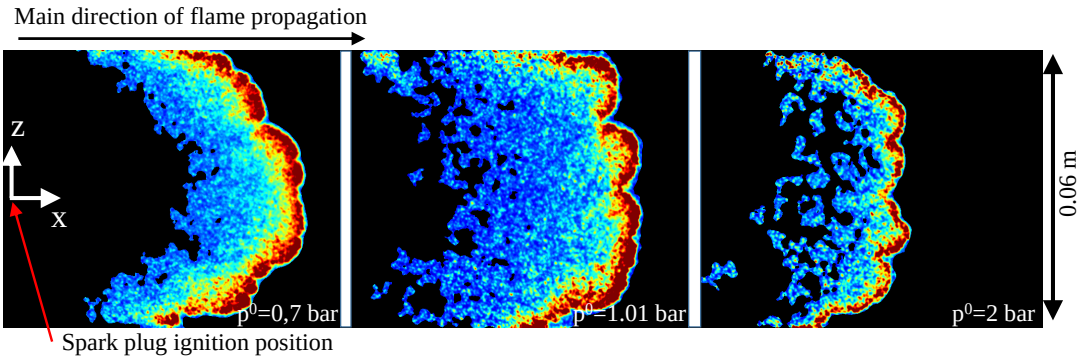

Figure 6.10: OH-PLIF images for a hydrogen concentration of 13% under variation of initial pressure p^0. The OH-PLIF signal is colorized according to its intensity in the raw images. Red: high intensity; blue: low intensity; black: no signal detected. The flame is propagating from left to right.

Figure 6.11 summarizes the experimentally determined two-dimensional flame wrinkling factors $\Xi_{m,2D}$ for different initial pressure levels (cases 8, 9 and 10 in Tab. 4.1). At each initial pressure level the hydrogen concentration was varied in the range between 12% and 23%. A strong dependence of the $\Xi_{m,2D}$ factor on the hydrogen concentration can be identified at each initial pressure level. As expected the flame wrinkling factor is decreasing with increasing hydrogen concentration due to decreasing influence of thermal-diffusive instability mechanisms in richer mixtures. Additionally, a fit is plotted for each initial pressure level to facilitate data evaluation.

To evaluate the effect of the initial pressure level on flame surface wrinkling, Figure 6.12 shows three-dimensional flame wrinkling factors Ξ_{wrink} for three initial pressure levels under varying hydrogen concentration. The curves are derived from the fitted curves in Fig. 6.11 and extended by utilization of Eq. 6.9. It can be observed that the Ξ_{wrink} factors for the initial pressure level of 2 bar show the highest values for a specific hydrogen concentration. With decreasing initial pressure level the Ξ_{wrink} values are also decreasing. This observation implies that the flame surface area is increasing with increasing initial pressure level. It can be stated that a smaller wrinkling structure leads to an enlarged flame surface in the investigated case. Furthermore, it can be observed that the flame area en-

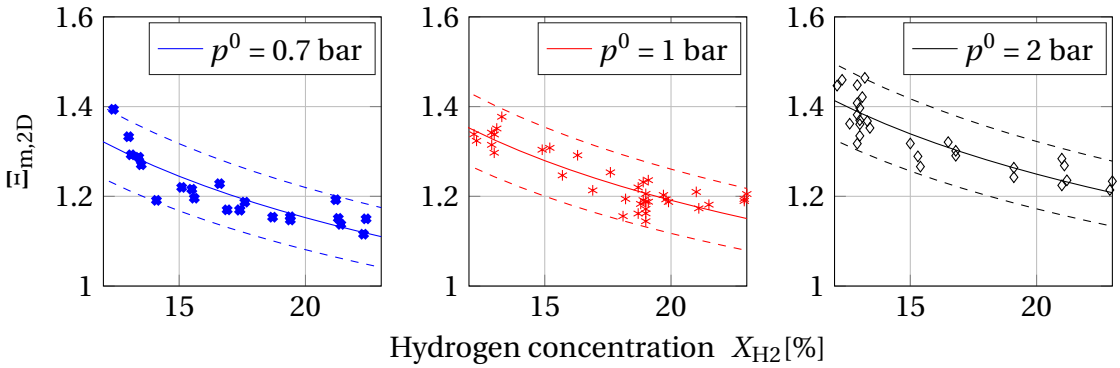

Figure 6.11: Values of experimentally determined flame wrinkling factor $\Xi_{m,2D}$ under concentration and initial pressure level variation (cases 1, 6 and 7 in Tab. 4.1). Additionally, a fit for each pressure level and an uncertainty interval of ±5.8% have been added enclosing all measured values.

largement due to a higher initial pressure level seems to have the same dependency for the investigated hydrogen concentration range.

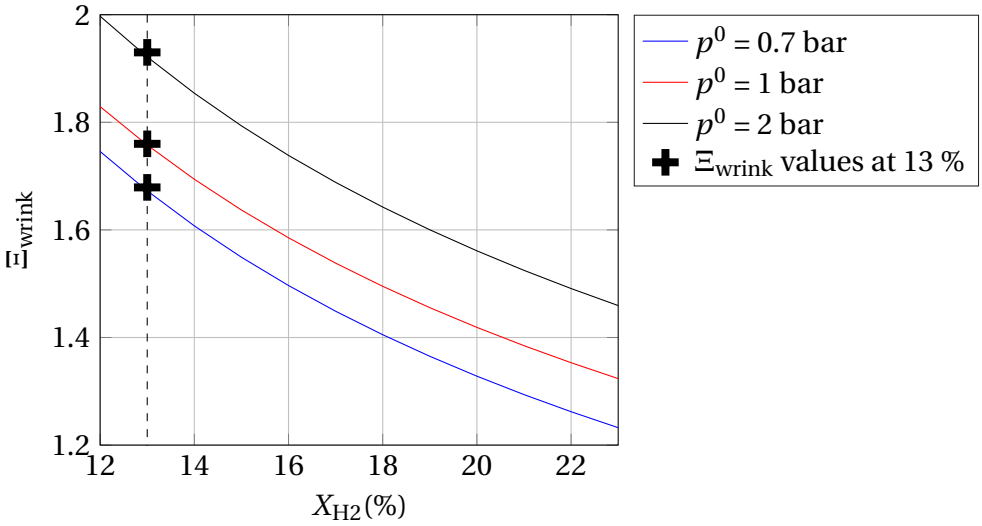

Figure 6.12: Three-dimensional flame area enlargement factor Ξ_{wrink} for varying initial pressure level and varying hydrogen concentration, derived from Fig 6.11.

The evaluated simulation data consists of flame surfaces corresponding to four initial pressure levels (0.5 bar, 0.7 bar, 1.01 bar and 2 bar) according to cases 1, 5, 6 and 7 in Tab. 4.1. The simulations were conducted for a constant hydrogen concentration of 13%. Due to the shorter domain

length compared to the explosion channel, the pressure during the simulation was stronger increasing and therefore was also taken into consideration during data evaluation and model formulation.

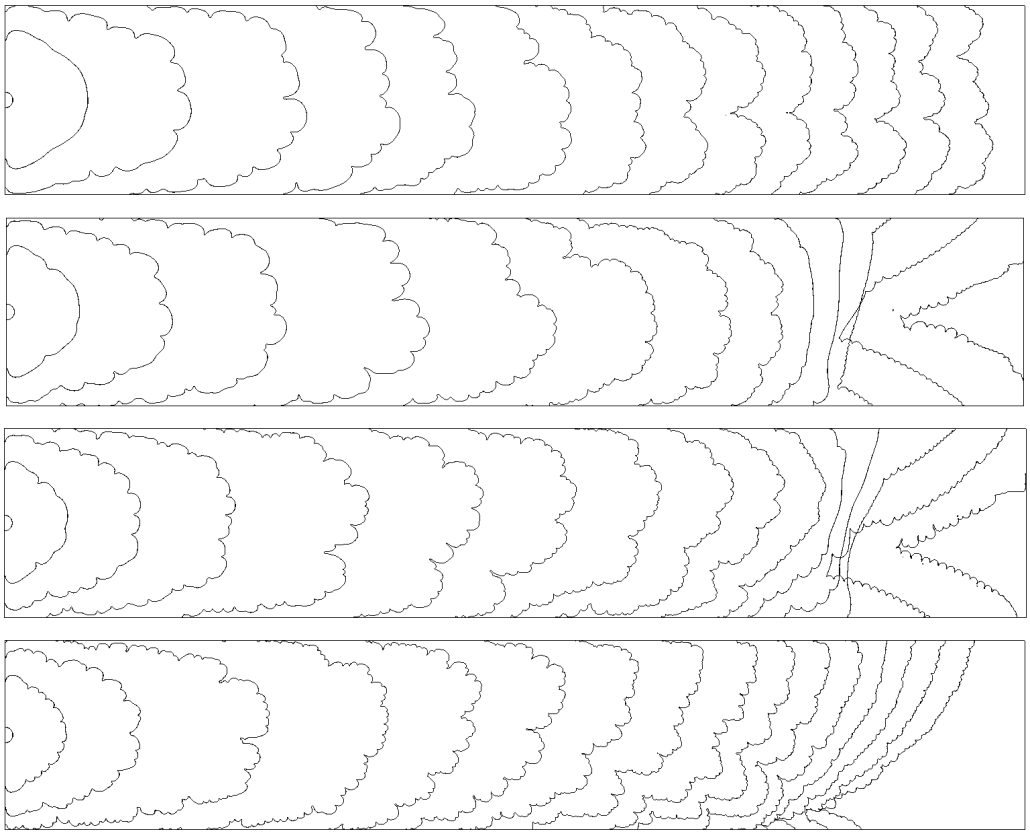

Figure 6.13: Numerically computed flame contour plots at different times. Δt denotes the time between each flame contour plot. From top to bottom: case 5 ($p^0 = 0.5$ bar, $\Delta t = 0.015$ s), case 6 ($p^0 = 0.7$ bar, $\Delta t = 0.015$ s), case 1 (reference, $p^0 = 1.01$ bar, $\Delta t = 0.015$ s) and case 7 ($p^0 = 2.0$ bar, $\Delta t = 0.02$ s).

Figure 6.13 shows the development of the simulated cellular flame structure for varying initial pressure p^0. The visualized flame surface is defined as the $T = 800$ K contour, i.e. roughly the average between initial temperature and adiabatic flame temperature. The cell size apparently decreases with increasing initial pressure. Especially in the high pressure case, primary as well as secondary cells can be identified. A second observation concerns the trend towards smaller cells during the pressure build-up in the closed domain. If a tulip shape of the flame appears in the final stages before complete burnout (frames 3 and 4, i.e. cases 6 and

1), these particular contour lines are not used for further evaluation. In the last frame (case 7, $p^0 = 2.0$ bar), featuring the slowest flame propagation, the output time interval is adjusted from $\Delta t = 0.015$ s to $\Delta t = 0.02$ s to obtain a similar number of contour lines. The smaller the flame speed, the more important buoyancy becomes. Therefore, the flame front develops an increasingly inclined shape since hot gases tend to move to the channel top.

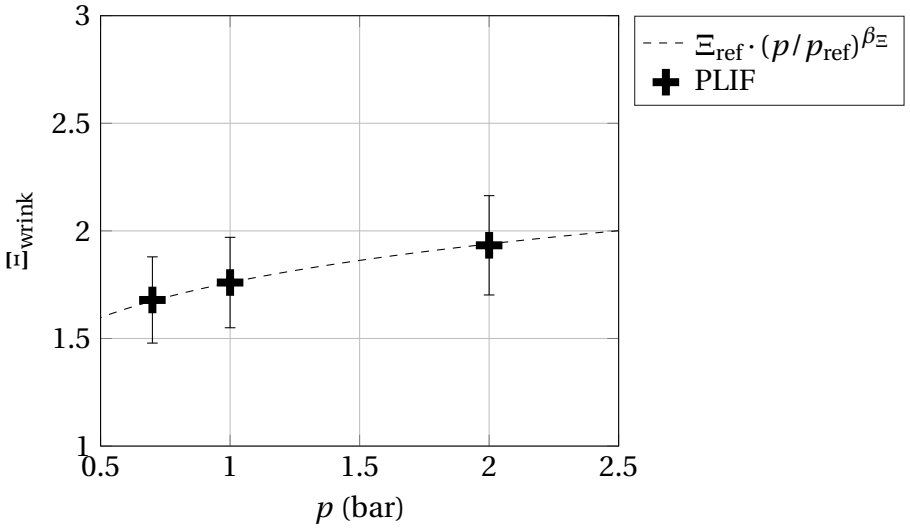

Figure 6.14: Experimentally determined three-dimensional flame wrinkling factors Ξ_{wrink} under varying initial pressure with uncertainties derived from uncertainty interval in Fig. 6.11. Additionally, a power law model is depicted describing the observed behavior.

Flame wrinkling factors have been evaluated for all simulations. Additionally, the pressure was evaluated during the simulation, allowing to connect the flame wrinkling factors to the corresponding pressure. Without significant spatial gradients, the pressure fields are nearly uniform. For increasing pressure, the graph reflects the competition between flame surface area enlargement and laminar burning velocity decline at the same time. Fig. 6.14 shows the detected Ξ_{wrink} values at 13% under varying initial pressure. Additionally, a power law fit is depicted describing the observed behavior under varying pressure. The idea to describe the observed behavior with a power law formulation is based on work of Dinkelacker et al. [30]. Dinkelacker et al. constructed a power law

dependency of flame wrinkling, more specifically turbulent flame speed, over a wide range of pressure levels.

Figure 6.15 summarizes the obtained experimental and numerical results. The Ξ_{wrink} factors from simulations for four different initial pressure levels are shown together with the experimental PLIF values. The shown flame wrinkling factors from the simulations are evaluated in regime C, where the macroscopic flame shape is not altering. It can be observed that Eq. 6.12 predicts the simulation values for higher pressures in a satisfactory way.

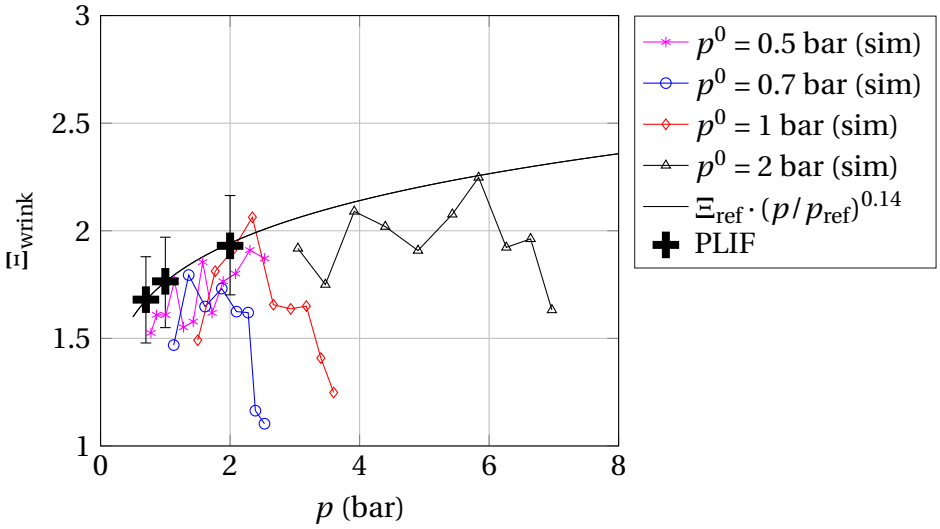

Figure 6.15: Development of the flame wrinkling factor under varying pressure.

The decrease of the flame wrinkling factor might be explained by the decrease of the size of the cellular structures due to thinner flame fronts with increasing pressure. This decrease of cellular cell size seems to result in an asymptotic approach to a smooth flame front accompanied by a decrease of the flame area enlargement factor. Finally, the power law exponent β_Ξ for the pressure extension in this work is determined to a value of 0.14:

$$F_p = \frac{\Xi_{\text{wrink,p}}}{\Xi_{\text{wrink}}} = \left(\frac{p}{p_{\text{ref}}}\right)^{0.14} \tag{6.12}$$

with $p_{\text{ref}} = 1$ bar.

6.3 Thermodynamic influence on laminar burning velocity: F_{Thermo}

Due to the piston-like effect of the propagating flame front in the closed channel, the unburned gas ahead of the flame front experiences preheating and compression. According to Gelfand et al. [44] the influence of temperature and pressure on $s_{\text{l},0}$ can be modeled mixture dependent. For this purpose, calculations of $s_{\text{l},0}$ at standard pressure (1 bar) and varying temperatures are conducted with Cantera [46] and the reaction mechanism of Konnov [65]. In the subsequent step calculations at standard temperature under varying pressure are conducted.

The pressure and temperature influence on $s_{\text{l},0}$ is summarized in the thermodynammic factor F_{Thermo} following Metghalchi and Keck [82]:

$$s_{\text{l},0} = s_{\text{l},0,\text{ref}} \left(\frac{T_u}{T_{\text{ref}}} \right)^{\alpha} \left(\frac{p}{p_{\text{ref}}} \right)^{\beta} = s_{\text{l},0,\text{ref}} F_{\text{Thermo}} \tag{6.13}$$

6.3.1 Temperature influence

Fig. 6.16 shows the calculated unstretched laminar burning velocities for different concentrations under varying initial temperatures plotted on a logarithmic scale. As expected, the lean mixtures have a lower laminar burning velocity than the stoichiometric mixture at the same temperature. Furthermore, the laminar burning velocities are increasing for increasing initial fresh gas temperatures. This relationship can be modeled by means of an exponential factor, as shown in Eq. 6.13.

Figure 6.17 shows the derived exponential factors for varying concentrations, which demonstrates that the exponential factors have higher values in lean mixtures than in richer ones. Additionally, a second order polynomial fit is depicted.[1] Eq. 6.14 describes the determined correlation for the exponential factor α.

[1] Second order polynomial fit functions were used in Eq. 6.14 and Eq. 6.15 due to input constraints of the used software.

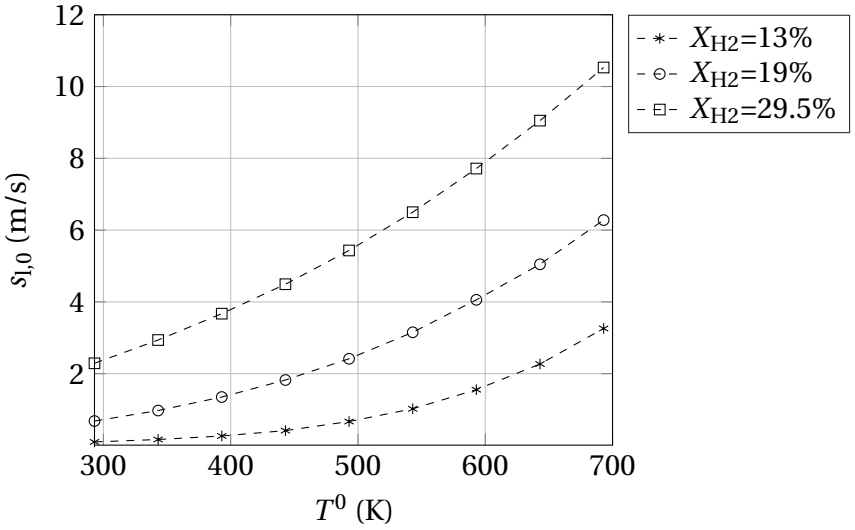

Figure 6.16: Calculated laminar burning velocities for different concentrations under varying initial temperature.

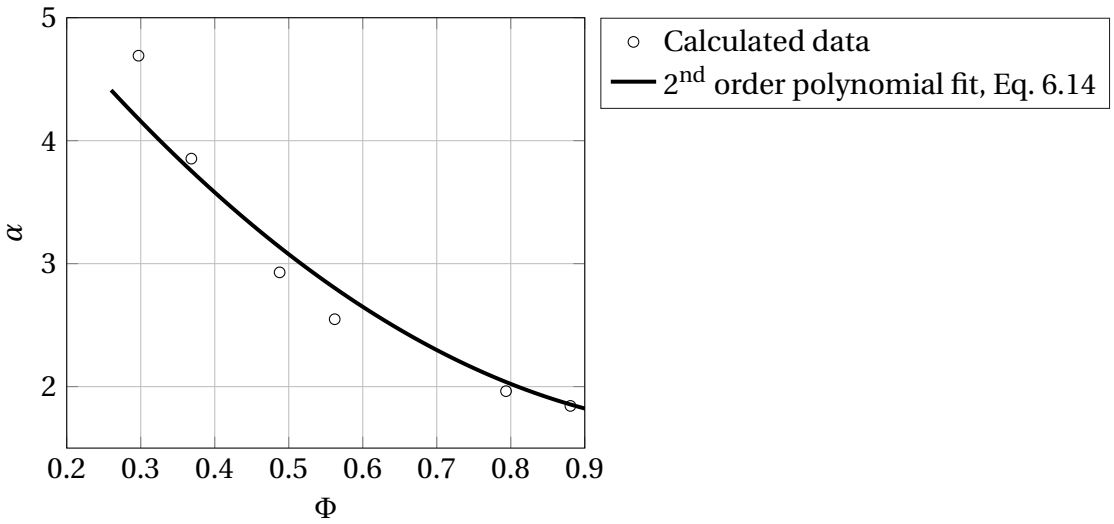

Figure 6.17: Calculated temperature exponents for varying concentrations. Additionally, a polynomial fit is plotted.

$$\alpha = 3.791\Phi^2 - 8.443\Phi + 6.35 \tag{6.14}$$

6.3.2 Pressure influence

Figure 6.18 shows the calculated unstretched laminar burning velocities for different concentrations under variation of the initial pressure. There are two behaviors that can be observed. In the rich and stoichiometric mixture, the laminar burning velocity initially rises with increasing pressure and decreases again as the pressure increases further. This effect is stronger in the rich mixture than in the stoichiometric mixture. The lean mixtures do not exhibit such behavior and the burning velocity drops immediately as the pressure level increases. The behavior under varying pressure is controversial in the literature, but a decay especially in lean mixtures is generally accepted [44] [65].

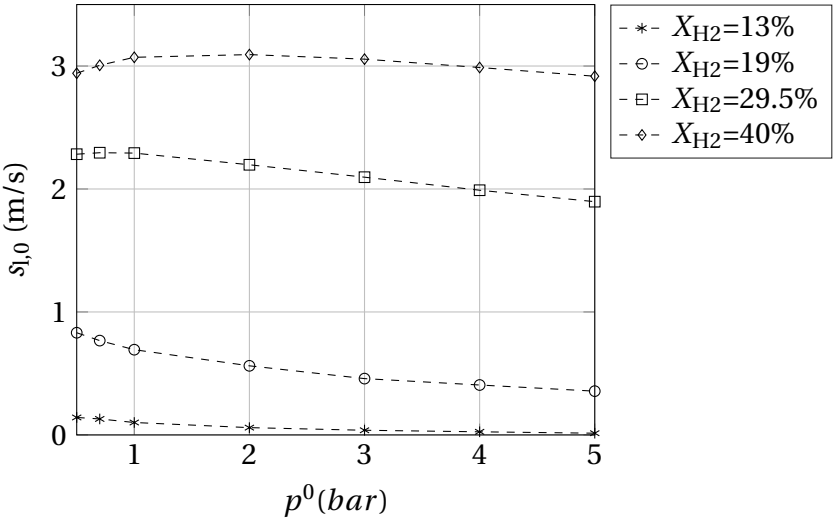

Figure 6.18: Calculated laminar burning velocities for different concentrations under varying pressure.

Fig. 6.19 shows the derived exponential factors for varying initial pressure levels, which demonstrates the influence of pressure is stronger in lean than in rich mixtures seen in larger values of the exponential factor.

Based on the identified dependence of the laminar burning velocity on the initial pressure level, Eq. 6.15 describes the determined correlation for the exponential factor:

$$\beta = -2.7\Phi^2 + 4.586\Phi - 2.1 \tag{6.15}$$

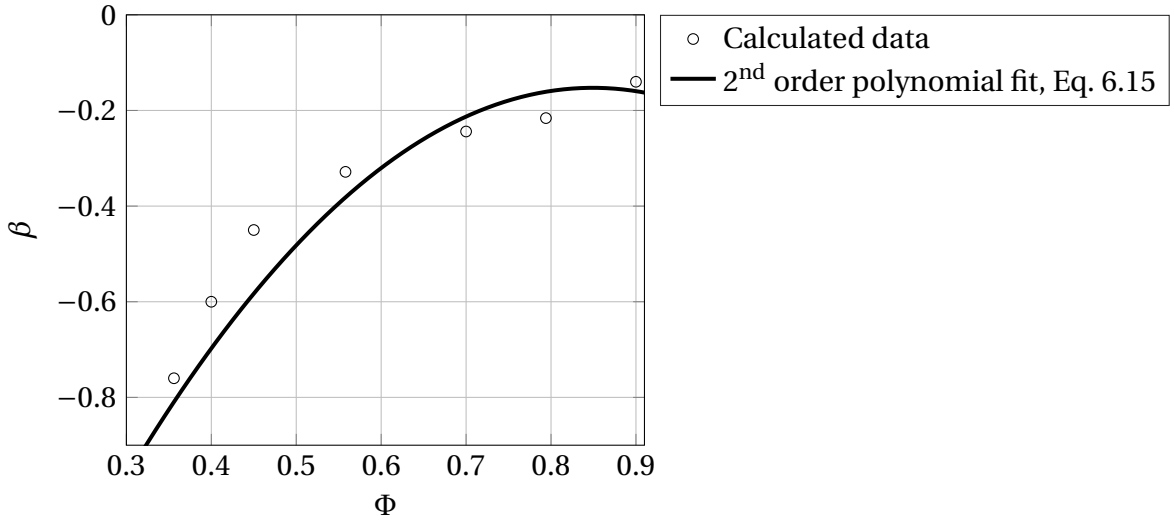

Figure 6.19: Calculated pressure exponents for varying concentrations. Additionally, a polynomial fit is plotted.

6.4 Influence of flame stretch: F_s

Due to the local small-scale flame front wrinkling, the laminar burning velocity is not constant along the flame front [107]. In the present work the investigated mixtures exhibit effective Lewis numbers below one. For that reason stretch effects play a significant role and increase the local burning velocity in convex parts of the flame front. To incorporate the influence of stretch on the laminar burning velocity in the new modeling approach the following issues must be resolved:

- Determination of the relationship of the stretched and unstretched laminar burning velocities.
- Determination of the Markstein length as the proportionality factor between stretch and the laminar burning velocity.
- Determination of stretch due to local small-scale flame front wrinkling.

The general correlations in Sec. 2.4 are the basis of the modeling approach in the present section. Here these equations are modified and

expanded to account for the characteristics of the investigated problem. The following sections discuss subsequently the issues mentioned above.

6.4.1 Relationship between stretched and unstretched burning velocity

Modeling of stretch effects in this work is based on the initial formulation of stretched laminar burning velocity introduced in Eq. 6.16:

$$s_{\mathrm{l,s}} = s_{\mathrm{l},0} - \mathscr{L} K \tag{6.16}$$

Based on the assumptions made in section 2.4 only curvature is contributing to the overall stretch rate. The contribution of strain to the overall stretch rate can be neglected [79] [88]. The stretch rate caused by flame front curvature can be determined by multiplying the geometrical small-scale local curvature κ with the local displacement speed s_d. The local displacement speed is expressing the local velocity of the flame front with reference to the fresh gas ahead of the flame. Following this, the stretch factor K can be formulated as follows:

$$K = s_d \kappa \tag{6.17}$$

According to Poinsot and Veynante [89] the local displacement speed s_d is difficult to determine in experiments and simulations, however, in this work assumptions are made to determine this variable. If the mixture is not prone to intrinsic instabilities and therefore not developing local flame front wrinkling ($\mathrm{Le}_{\mathrm{eff}} \approx 1$ or $\mathscr{L} \approx 0$) the displacement speed can be selected as the unstretched laminar burning velocity $s_{\mathrm{l},0}$ [92]. However, in mixtures with effective Lewis numbers < 1 the displacement speed should be selected as the stretched laminar burning velocity $s_{\mathrm{l,s}}$ according to Bradley et al. [17] and Chen [24]:

$$s_d = s_{\mathrm{l,s}} \tag{6.18}$$

leading to a non-linear relationship [92]. Following this, Eq. 6.16 can be transformed to:

$$\frac{s_{\mathrm{l,s}}}{s_{\mathrm{l,0}}} = (1 + \mathscr{L}\kappa)^{-1} \tag{6.19}$$

or in terms of non-dimensional numbers using the definitions in Eq. 2.20 and 2.21 following [86]:

$$\frac{s_{\mathrm{l,s}}}{s_{\mathrm{l,0}}} = \left(1 + \frac{\mathscr{L}}{\delta} \cdot \frac{K\delta}{s_{\mathrm{l,s}}}\right)^{-1} = (1 + \mathrm{MaKa})^{-1} \tag{6.20}$$

By non-dimensionalization of Eq. 6.16 the influence of the flame stretch on the laminar burning velocity can be formulated as a dimensionless factor considering the increase or decrease of the resulting burning velocity compared to the unstretched case. Finally, the factor F_s describing the enhancement of laminar burning velocity due to flame stretch reads as follows:

$$F_s = \frac{s_{\mathrm{l,s}}}{s_{\mathrm{l,0}}} = (1 + \mathscr{L}\kappa)^{-1} \tag{6.21}$$

6.4.2 Modeling of the Markstein number

Markstein lengths as mixture dependent proportionality factors between stretch and the burning velocity can be determined from theoretical considerations, as reported by e.g. Bechtold and Matalon [9], Lipatnikov and Chomiak [76], Lipatnikov and Chomiak [77] or Poinsot and Veynante [89]. Generally, the effects of strain and curvature on the laminar flame speed can be incorporated through separate Markstein numbers [79] [27] accounting for the varying contributions of strain and curvature to overall stretch. However following Bechtold and Matalon [9], the contributions of both effects can be combined into a single Markstein length.

A large scatter of Markstein lengths can be found in the literature for the same problem formulations, caused by varying definitions of laminar

burning velocity [103]. Compared to experimentally determined Markstein lengths, theoretically determined values also tend to overestimate the influence of stretch in very lean regimes.

To avoid these obstacles in the present work, experimentally determined Markstein lengths will be utilized. Fig. 6.20 summarizes experimentally determined Markstein lengths by different authors.

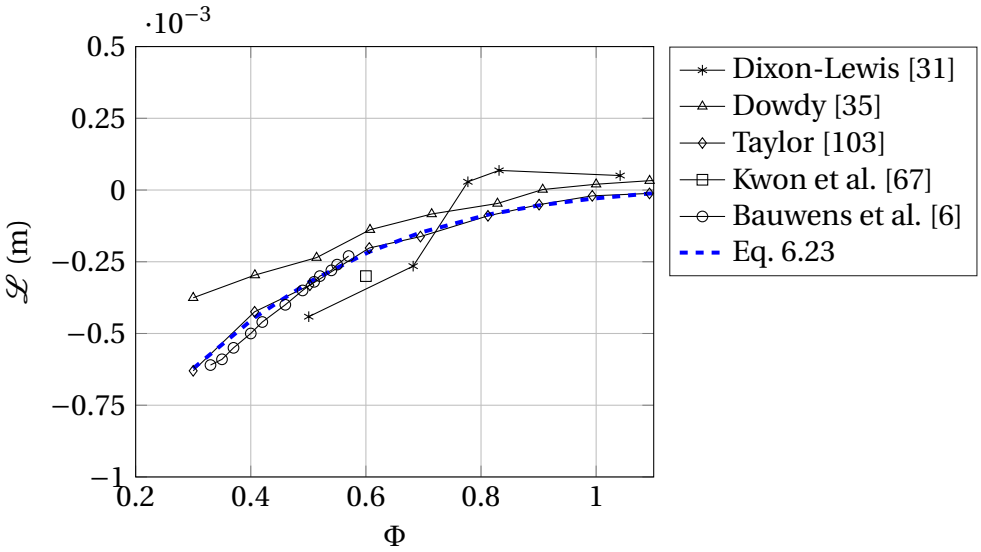

Figure 6.20: Overview of Markstein lengths for a hydrogen-air mixture under varying concentration according to different authors.

The selection of data from different authors shown in Fig. 6.20 is based on the used experimental setup to determine Markstein lengths. The determination based on expanding spherical flames seemed to be the appropriate experimental setup, since at least the initial flame propagation behavior in this work is similar.

An extensive investigation and determination of Markstein lengths based on expanding spherical flames can be found in Taylor [103]. As shown in Fig. 6.20 the values determined by Taylor [103] are in sufficient agreement with values reported by other authors. Recently, Bauwens et al. [6] employed values determined by Taylor [103] in their work.

It is important to note that in order to use the Markstein length L determined by Taylor [103] in the present work, the variable must be converted to a Markstein length $\mathscr{L}$ with reference to the unburned mixture,

following the relationship:

$$\mathscr{L} = L - \delta_Z \ln(\sigma) \tag{6.22}$$

with δ_Z as the Zeldovich flame thickness, Eq. 2.9.

The variation of the Markstein length with equivalence ratio can be modeled using the following polynomial fit based on values reported by Taylor [103]:

$$\mathscr{L} = 0.0007723\Phi^3 - 0.002694\Phi^2 + 0.003276\Phi - 0.001383 \tag{6.23}$$

In order to maintain a reasonable level of complexity in the new modeling concept, no pressure or temperature influence on Markstein lengths is contemplated, which is considered a reasonable simplification based on the occurring pressure and temperature ranges in the investigated cases in the present work.

6.4.3 Determination of flame front curvature

The determination of the flame front curvature is based on two approaches: the evaluation of OH-PLIF experiments and highly resolved two-dimensional simulations of the propagating flame front. Additionally, selected statistical moments of the flame front data are investigated to gain more insight into the small-scale wrinkling behavior of the flame front.

Since resolution of the computational grid of the simulations was chosen to be significantly higher than the resolution of the OH-PLIF images, the simulations allowed for more insight in the curvature behavior of the propagating flame front. It was also possible to compare both inherently different approaches to verify the applied evaluation techniques. Based on the simulations, it was also possible to investigate the strain influence on the overall stretch derived from the velocity gradients in the fresh gas ahead of the flame front. The stretch due to strain is small compared to stretch due to curvature. This observation confirms the assumption that

strain influence on stretch can be neglected and the primary contributor to stretch is local curvature of the flame front.

The determination of the geometrical curvature κ is based on the following mathematical definition along a two-dimensional curve [80]:

$$\kappa = \frac{\dot{y}\ddot{x} - \dot{x}\ddot{y}}{(\dot{y}^2 + \dot{x}^2)^{3/2}} \tag{6.24}$$

In order to calculate the curvature with this equation the curve must be parameterized $(x(s), y(s))$ with the parameter s and first and second derivatives $(\dot{x} = \frac{dx}{ds}, \ddot{x} = \frac{d^2x}{ds^2}, \dot{y} = \frac{dy}{ds}, \ddot{y} = \frac{d^2y}{ds^2})$ must be calculated with respect to s. The parameter s is chosen to be in order of the laminar flame front thickness which was estimated from one-dimensional temperature profiles calculated with Cantera [46] according to prior publications in the literature [72] [73].

Before evaluating flame front curvatures, the developed routine was tested for verification. The resolution of the images in this work was 0.1089 mm/pixel. The ability of the evaluation routine to detect small curvatures is dependent on the resolution of the raw OH-PLIF images. Figure 6.21 summarizes the result of the verification. Measured curvatures are plotted against known theoretical curvatures. The measured values follow the theoretical values so long as the routine is able to detect the correct curvatures of the test images. The routine follows the theoretical values up to 2 mm^{-1} which corresponds to a curvature radius of 0.5 mm.

Fig. 6.22 shows probability density functions (PDF) of the global flame front curvature of ten consecutive flame fronts determined from experimental data. The peak values of the PDFs are shifted to positive values, which is confirmed by the calculated skewness shown in Fig. 6.23. This plot shows the calculated skewness of the global curvature PDFs for a concentration of 13% H2 and an initial pressure level of 1 bar. It can be seen that the skewness is negative basically for the entire depicted time interval. This observation is consistent with data from literature for the case of small-scale flame front wrinkling due to flame instabilities [92] [93]. The shift to positive values means that positive curvatures (convex

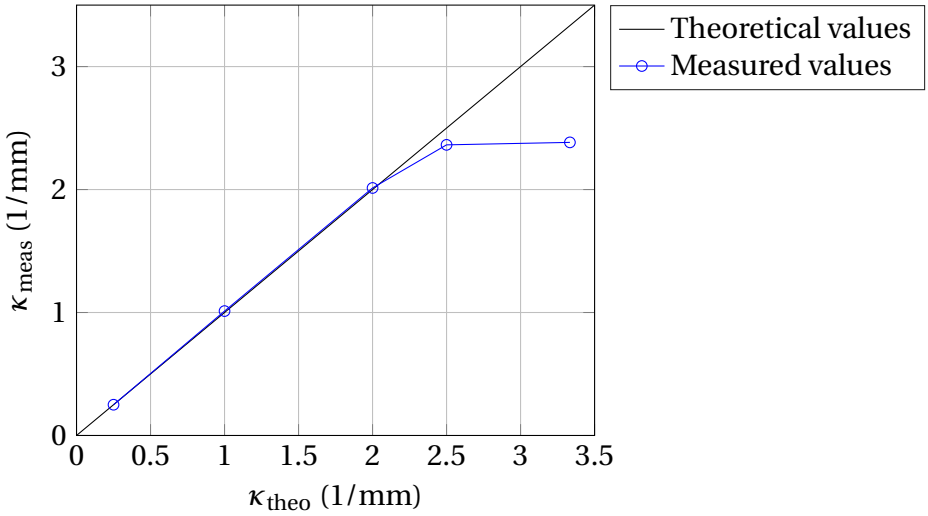

Figure 6.21: Measured curvature values plotted against known theoretical curvatures.

to unburned mixture) are more probable than negative curvatures along the flame front, confirming the observation quantitatively.

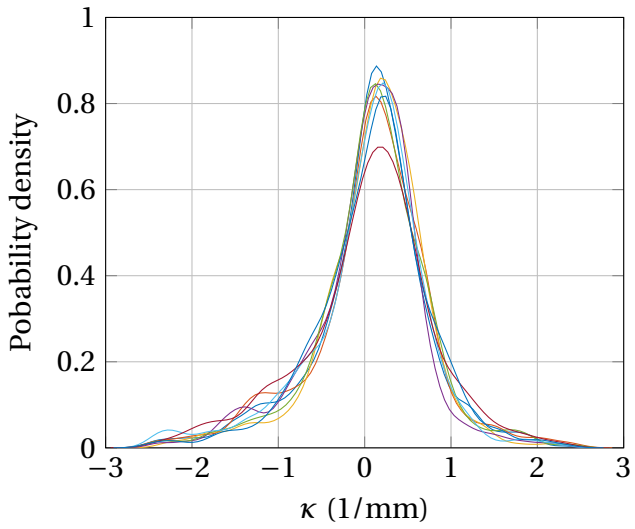

Figure 6.22: Probability density functions of global flame front curvatures of ten consecutive flame fronts with developed small-scale wrinkling. The flame fronts correspond to a concentration of 13% and an initial pressure level of 1 bar.

Since positive curvatures in lean hydrogen-air mixtures are responsible for flame acceleration, the modeling in this work is based on the averaged positive curvature values. Amato et al. [4] and Marshall et al. [80]

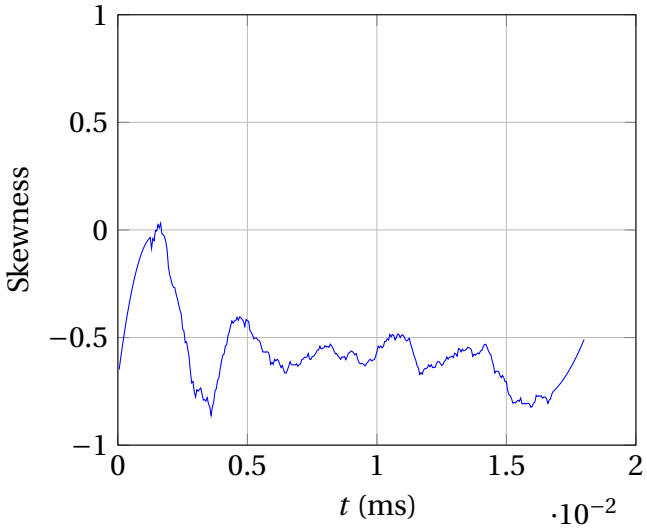

Figure 6.23: Development of skewness of the global curvature PDFs during a single experimental run over time for a concentration of 13% and a initial pressure level of 1 bar.

employ the concept of leading edge statistics in their work, where the curvature of the leading edge of the flame wrinkle is used for further modeling. In the present work this concept is adapted, but the entire convex part is considered for modeling. This results in a more conservative approach compared to mentioned literature.

Figure 6.24 shows the local curvature distribution along a flame front for a concentration of 13% and an initial pressure level of 0.5 bar derived from a highly resolved simulation. A close-up view of a flame front wrinkle is shown on the right of Fig. 6.24. Negative curvature values occur locally in concave parts of the flame front. The largest part of the flame front exhibits positive values. Based on the assumption that curvature influences the burning velocity locally, the pursued modeling approach in this work based on averaged positive curvature values is considered reasonable. These values are evaluated in every experimental run. Figure 6.25 shows averaged positive curvatures from OH-PLIF images for one experimental run plotted over time. The curvature value appears to reach a constant level towards the end of the optically accessible part of the channel, corresponding to regime C, depicted in 6.3. To determine the experimental curvature value, the averaging procedure was carried out in this regime.

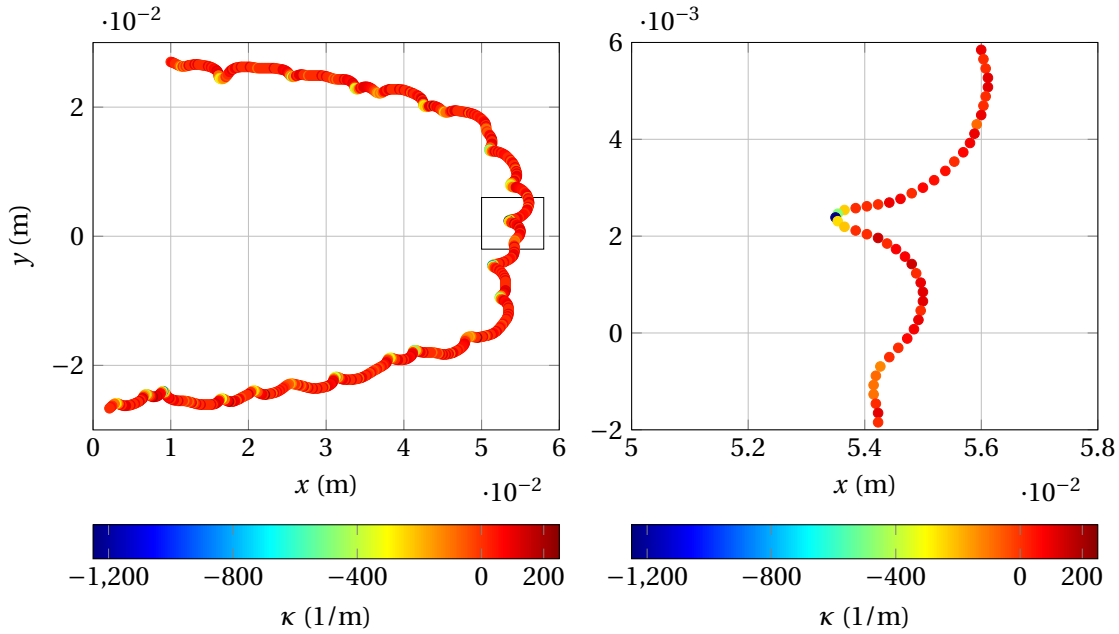

Figure 6.24: Local curvatue along the flame front from higly resolved simulations for a concentration of 13% and an initial pressure level of 0.5 bar. Left: entire flame front with area for close-up view; Right: close-up view of local curvature.

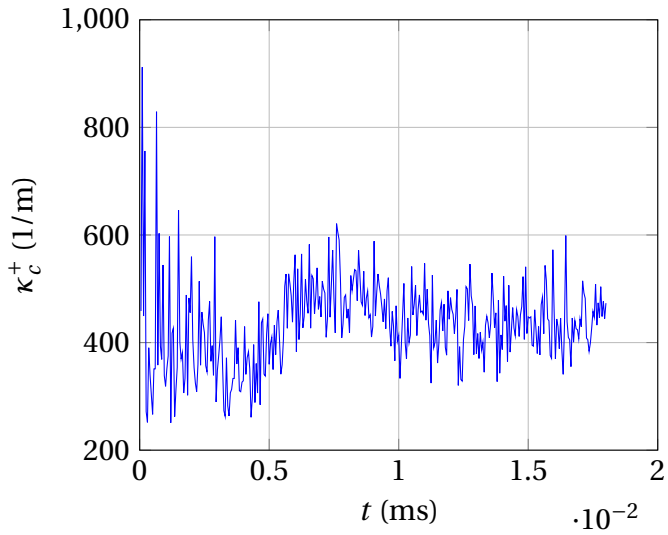

Figure 6.25: Mean positive curvature over time extracted from OH-PLIF images for a concentration of 13% and a initial pressure level of 1 bar.

Fig. 6.26 shows flame fronts obtained through highly resolved simulations under varying pressure and concentration. A developing cellular

structure of the flame front can be identified in all three cases. A reduction of the cell size can be seen under varying pressure (a to b). This effect could not be observed under varying concentration investigated in this project (a to c). Based on this, only the pressure dependency was considered for the formulation of the new modeling concept. The same observation of a larger sensitivity of the cell size regarding pressure can also be made in the shadowgraphy images shown in Fig. 6.27 and 6.28. This observation of non-sensitive curvature values regarding concentration variation has also been observed in the literature by Marshall et al. [80].

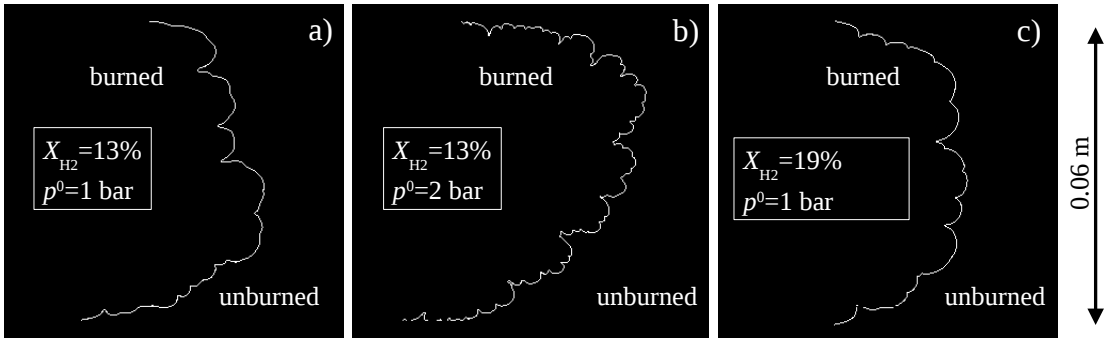

Figure 6.26: Calculated highly resolved flame fronts under variation of the concentration Φ (a to c) and variation of the initial pressure level p^0 (a to b).

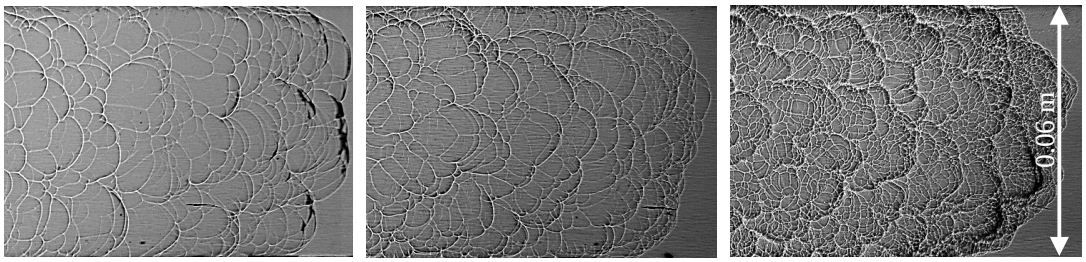

Figure 6.27: Shadowgraphy images of flame fronts under varying initial pressure levels.

Figure 6.29 summarizes the experimentally and numerically determined averaged positive curvature values under varying pressure. A pressure

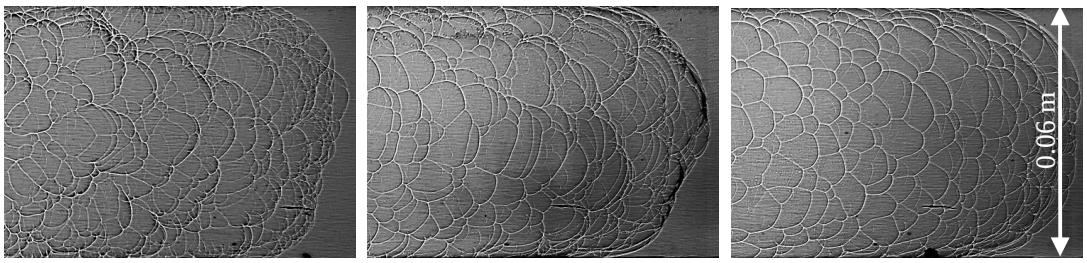

Figure 6.28: Shadowgraphy images of flame fronts under varying concentration levels.

dependence can be identified and is modeled by a power law according to Eq. 6.25:

$$\kappa_{2D} = \kappa_{ref} \left(\frac{p}{p_{ref}} \right)^{0.55} \tag{6.25}$$

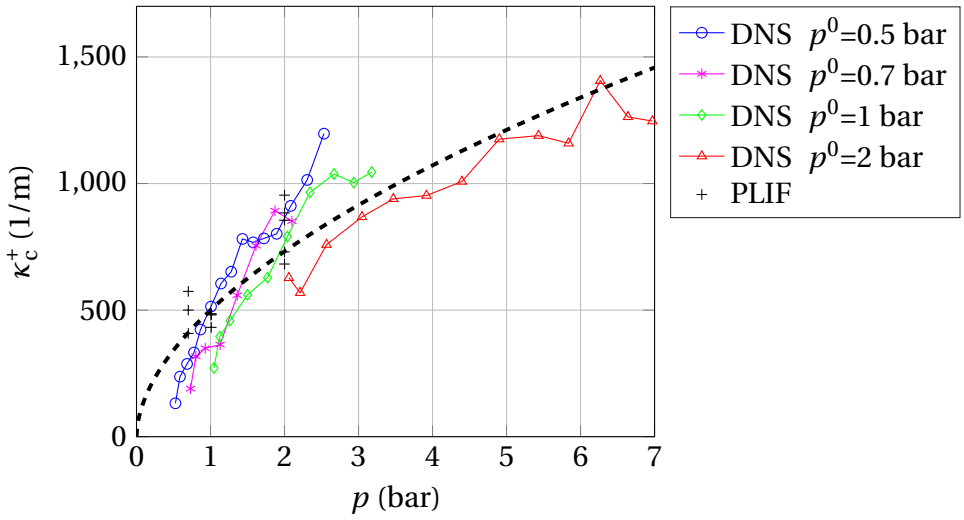

Figure 6.29: Mean positive curvature under varying pressure.

Due to the non-linear formulation of the dependence between the stretched and unstretched laminar burning velocities in Eq. 6.21, high curvature values can lead to unreasonably high burning velocity ratios. These unreasonably high burning velocity ratios most likely occur in the extreme case of very lean mixtures at high pressures and can also lead to numerical problems during simulations. For this reason, a limitation

strategy must be implemented to avoid these problems. The limitation strategy in this work is based on the limitation of the maximum pressure values influencing curvature in Eq. 6.25. Assuming a combustion process in an adiabatic closed volume entirely filled with a combustible mixture, the pressure increases from the initial pressure level p^0 to the thermodynamic limit value of the adiabatic isochoric complete combustion pressure p_{AICC}, at which the combustion is completed and the flame front is not moving anymore. The behavior of the flame front especially at high pressures is evaluated more closely based on non-dimensionalized flame wrinkling factors obtained from highly resolved simulations.

Figure 6.30 shows non-dimensionalized Ξ_{wrink} factors over non-dimensionalized varying pressure for three different initial pressure levels. The Ξ_{wrink} factors are non-dimensionalized with the maximum Ξ_{wrink} value of each simulation. The pressure is non-dimensionalized utilizing the adiabatic isochoric complete combustion pressure p_{AICC} for each initial pressure level. The p_{AICC} values were calculated with CANTERA [46] and are summarized in Table 6.1.

Table 6.1: Calculated values of adiabatic isochoric complete combustion pressures p_{AICC} for the investigated initial pressure levels.

p_0	0.5 bar	0.7 bar	1.01 bar	2 bar
p_{AICC}	2.576 bar	3.607 bar	5.15 bar	10.306 bar

Fig. 6.30 shows that the value of the flame wrinkling factor is initially increasing due to the developing small-scale wrinkling of the flame surface. After this development, the value appears to reach a constant level. Once the flame reached a specific pressure ratio, the value decreases again and the influence of small-scale wrinkling seems to diminish. The behavior of the decreasing ratio of the Ξ factors can be detected in all three investigated cases. Furthermore, the non-dimensionalized curves overlap and decrease at a similar non-dimensional value of the pressure ratio.

Based on this observation a limit value for the pressure influence will be considered in the present work. The contribution of pressure to curvature will be limited to a concentration dependent value of $0.5 \cdot p_{\mathrm{AICC}}$ preventing non-physically high burning velocity ratios leading to numerical

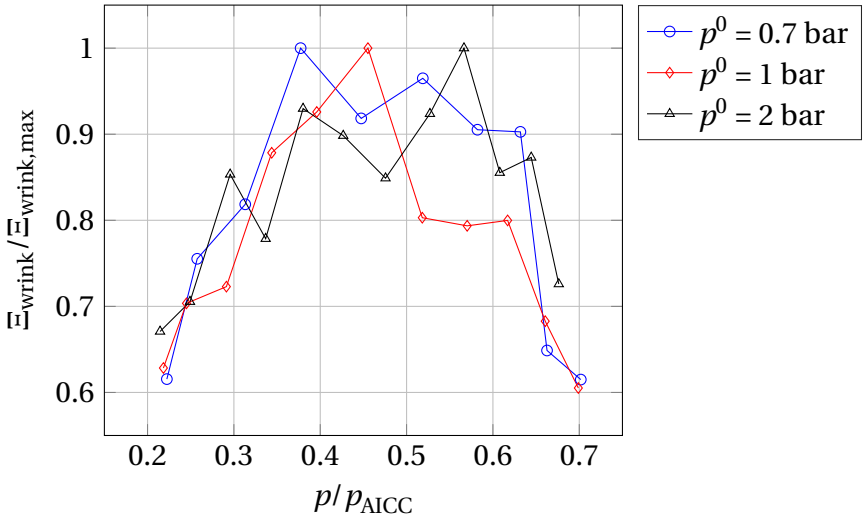

Figure 6.30: Values for Ξ_{wrink} of highly resolved simulations under variation of initial pressure p_0. Non-dimensionalized with p_{AICC} and the maximal Ξ_{wrink} value of each simulation, respectively.

instability. Eq. 6.25 results in the following formulation:

$$\kappa_{2D} = \kappa_{ref} \left(\frac{\max(p;\, 0.5 \cdot p_{AICC})}{p_{ref}} \right)^{0.55} \tag{6.26}$$

The increase of the pressure level from the initial value p^0 to the theoretical peak value p_{AICC} is of exponential nature, as seen in Fig. 6.31 for the THAI HD7 experiment [99]. The details of the experiment and setup are discussed later in Sec. 7.3.1. The value of 50% of p_{AICC} is reached approximately 2.2 s after ignition, whereas the peak value is reached shortly after at 2.7 s. This shows the limitation value ($0.5 \cdot p_{AICC}$) is reached towards the end of the experiment and the implemented limitation does not affect the simulations in the initial phase. After the value of 50% of p_{AICC} is reached the pressure value and the resulting curvature are constant until the end of the simulation. In this end phase of the simulation the influence of the end plate on flame propagation increases, resulting in flame propagation that is not along the rotational axis of the facility. Schramm et al. [99] state that other effects, e.g. acoustic waves seem to have significant influence on flame propagation in this end phase of the experiment, leading to the observed flame front behavior. Based on this,

the limiting of the curvature value formulated in Eq. 6.26 is considered a reasonable approach.

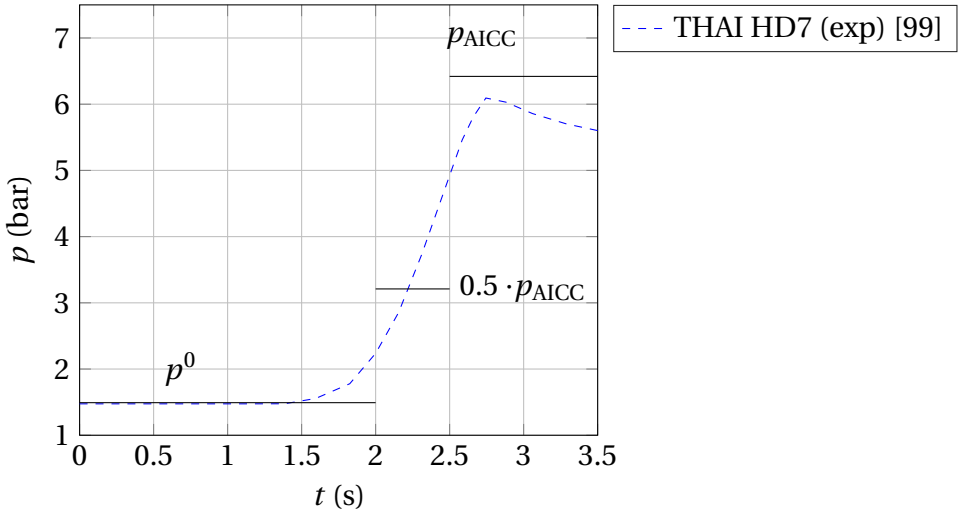

Figure 6.31: Comparison of pressure development in the simulations and the experiment.

Finally, the curvature values determined from the OH-PLIF images and the highly resolved simulations are inherently of two-dimensional nature. In reality, the investigated problem is three-dimensional, so an appropriate extension for the effect of the third dimension must be modeled. The extension in the present work is based on works by Hawkes et al. [53] and is formulated as follows:

$$\kappa_{3D} = \frac{\pi}{2} \cdot \kappa_{2D} \tag{6.27}$$

resulting in the final formulation:

$$\kappa_{3D} = \frac{\pi}{2} \cdot \kappa_{ref} \left(\frac{\max(\, p;\, 0.5 \cdot p_{AICC})}{p_{ref}} \right)^{0.55} \tag{6.28}$$

with $\kappa_{ref} = 500\ 1/\mathrm{m}$ and $p_{ref} = 1$ bar.

6.5 Grid size sensitivity: F_Δ

A grid sensitivity study with grid refinement until steady-state in the solution is reached cannot be conducted in the investigated problem scenario. To resolve the governing processes responsible for small-scale wrinkling of the flame front, computational grid resolutions below the laminar flame thickness would be required. A three-dimensional computational grid of that resolution cannot be handled by the usual computation power available in URANS simulation setups. However, the modeling strategy pursued in this work derives and implements a procedure to significantly reduce grid sensitivity.

Since the procedure for the reconstruction of the smooth flame front was adapted from CFD [5], it can be assumed that the filtered flame front from the experiment is similar to the flame front reproduced in a simulation on a computational grid of the equivalent grid size. For non-uniform computational grids where the edge lengths of the elements differ, an average cell edge length can be calculated based on the local cell volume:

$$l_\Delta = (\text{local cell volume})^{1/3} \tag{6.29}$$

The evaluation of the flame wrinkling factor in this work is based on a reference evaluation grid size of $l_\Delta = 0.0075$ m, indicated through white arrows in Fig. 5.2. The size of the evaluation grid has influence on the amount of flame wrinkles resolved through the theoretical smooth flame front, discussed in Sec. 5.2. The smaller the evaluation grid size, the smaller the detected flame wrinkling factor, since the smooth flame front can reproduce more of the true small-scale wrinkling. The inverse occurs when the evaluation grid size is increased. To quantify this effect, evaluations of the flame wrinkling factor are performed using varying grid sizes: $l_\Delta = 0.002$ m, 0.004 m, 0.006 m, 0.0075 m, 0.010 m, 0.012 m, 0.015 m, 0.020 m, 0.030 m.

The determined two-dimensional flame wrinkling factors for varying grid sizes are summarized in Fig. 6.32. A variation of concentration is also shown. The determined flame wrinkling factors under varying concen-

trations follow a similar trend. As expected, the smaller the evaluation grid size, the smaller the flame wrinkling factor and vice versa.

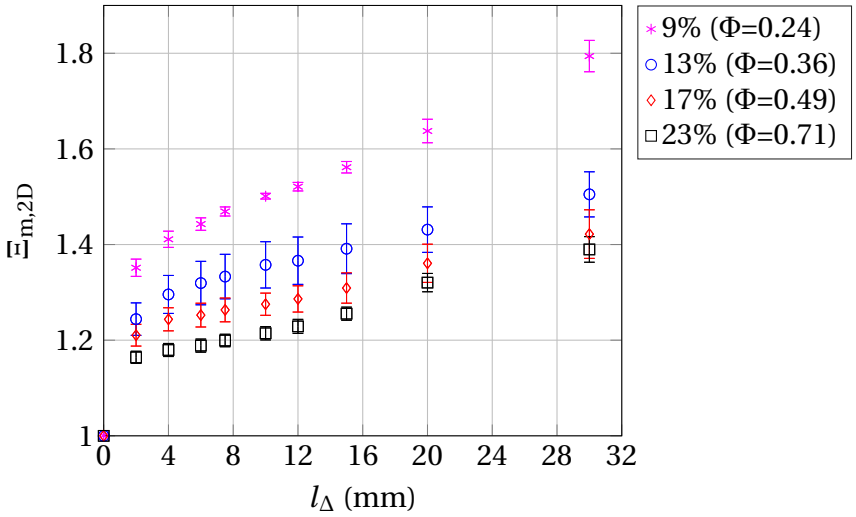

Figure 6.32: Experimentally determined two-dimensional flame wrinkling factors under varying evaluation grid size for different concentrations. The error bars denote standard deviations.

In Fig. 6.33, the experimentally determined values of the flame wrinkling factors for varying concentrations at 1 bar are plotted against non-dimensionalized grid size. For this, the respective flame wrinkling factor at a certain grid size $\Xi_{\text{wrink},\Delta}$ was non-dimensionalized by the wrinkling factor at the reference grid size $\Xi_{\text{wrink,ref}}$ resulting in the grid factor:

$$F_\Delta = \frac{\Xi_{\text{wrink},\Delta}}{\Xi_{\text{wrink,ref}}} \tag{6.30}$$

It can be observed in Fig. 6.33 that the factor F_Δ does not exhibit a significant influence of the hydrogen concentration. The trends overlap for varying concentrations. In the case where the grid sizes are decreasing in the direction of the theoretical lower limit, the factor approaches a finite value of greater than zero. Assuming a flame wrinkling factor $\Xi_{\text{wrink},\Delta} = 1$ with grid size approaching zero, the factor F_Δ approaches the value Ξ_{ref}^{-1}. Since the evaluation on grids larger than 30 mm was not possible and did not seem reasonable, factors F_Δ for larger grid sizes are extrapolated.

The determined dependence of factor F_Δ on the varying grid size was modeled using a power law according to Eq. 6.31. The calculated com-

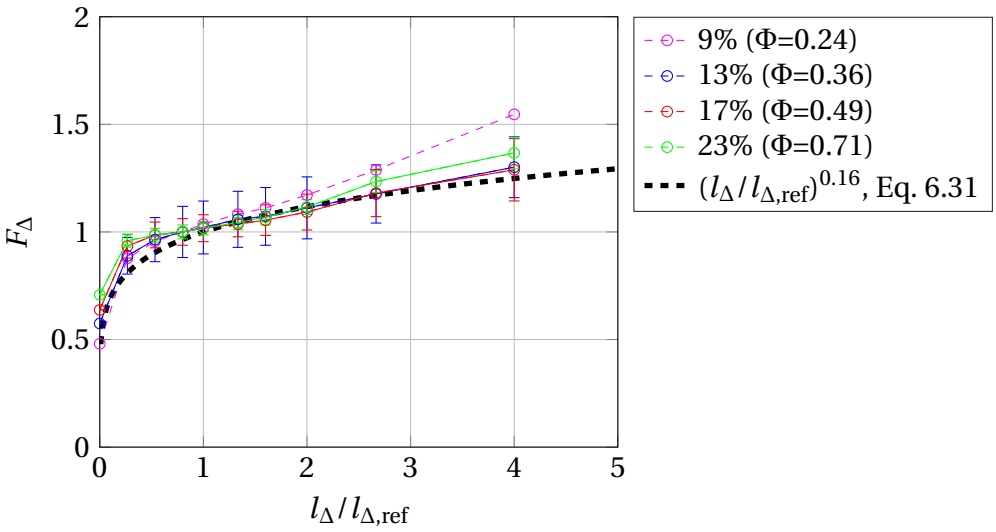

Figure 6.33: Non-dimensional grid factor under varying non-dimensional grid size.

putational local grid size l_Δ is divided by the reference value $l_{\Delta,\mathrm{ref}} = 7.5$. As intended, the factor F_Δ exhibits a value of 1 at the reference grid size. Additionally, the chosen power law dependence of the factor F_Δ on the dimensionless grid size avoids high non-physical values that would most likely occur utilizing a linear modeling approach. The final formulation reads as follows:

$$F_\Delta = \frac{\Xi_{\mathrm{wrink},\Delta}}{\Xi_{\mathrm{wrink,ref}}} = \left(\frac{l_\Delta}{l_{\Delta,\mathrm{ref}}} \right)^{0.16} \tag{6.31}$$

with the reference value $l_{\Delta,\mathrm{ref}} = 0.0075$ m.

6.6 Turbulence influence: F_t

In order to extend the application possibilities of the newly developed modeling approach to turbulent combustion, the new model must consider acceleration due to turbulence. However, the current experimental setup of the GraVent explosion channel does not allow for measurements of turbulence levels prior to and during an experiment. Therefore, an appropriate correlation from literature is incorporated into the modeling

concept.

A large number of validated models can be found in the literature capturing the effect of turbulence on flame acceleration. However, the correlation for turbulence influence included in this modeling approach must be chosen carefully. No cross-correlation of accelerating effects should be implemented. This means that the factor introduced for turbulence driven acceleration must not have an influence on the flame acceleration predicted by effects that are already captured in the formulated factors described above. Additionally, a robust low-turbulence limit behavior must be ensured. In this work the correlation following Peters [87] is used:

$$F_t = \frac{s_t}{s_{l,0}} = 1 - \frac{0.39}{2}\frac{l_t}{\delta_F} + \left(\left(\frac{0.39}{2}\frac{l_t}{\delta_F}\right)^2 + 0.78\frac{u' l_t}{s_{l,0}\delta_F}\right)^{0.5} \tag{6.32}$$

with the turbulent fluctuation velocity u' (Eq. 2.24) turbulent length scale l_t (Eq. 2.25) and the flame thickness δ_F (Eq. 2.10).

The advantage of this correlation for the newly developed modeling concept in this work is that Eq. 6.32 is only dependent on turbulence variables and for that reason does not cross-correlate with the other implemented factors in Eq. 6.2. This way, a clear separation of the acceleration mechanisms can be ensured. Additionally, Eq. 6.32 is valid in the entire Borghi-Diagram, Fig. 2.11. Based on the mathematical formulation of 6.32, the turbulence acceleration factor F_t exhibits a realistic behavior approaching the limiting case of vanishing turbulence and approaches the value of one. That means that the turbulent flame speed s_t approaches the value of the laminar burning velocity $s_{l,0}$.

6.7 Modeling of test facility specific effects: B

6.7.1 General aspects

According to Beauvais et al. [7], the geometry of an experimental facility is one of the most important and yet most complex parameters to con-

sider in the context of flame acceleration. The authors name three crucial geometrical parameters influencing flame propagation: the relative size of obstacles, the distance between obstacles and the degree of confinement. In the present work flame propagation in a fully confined smooth channel with no obstacles is investigated, therefore the focus of this section is solely on the effect of flame confinement on flame propagation.

The volume of burned gas resulting from the combustion process must be vented downstream. In an entirely closed experimental facility, the burned gas cannot escape the channel and produces an expansion flow downstream the flame front. The influence of this expansion flow on flame propagation is higher compared to a case with venting downstream. This effect is even more pronounced if the flame shape deviates from a planar shape, resulting in an enlarged global flame surface area. Eq. 2.23 can be extended by flame surfaces deviating from the planar cross-sectional shape of the experimental facility resulting in the following formulation:

$$\underbrace{\sigma s_u A_F}_{u_F} = u_{\text{gas}} A_{cross} + s_u A_F \tag{6.33}$$

with A_F as the enlarged flame surface area and A_{cross} as the cross-sectional area of the facility. Since the left side of Eq. 6.33 represents the flame propagation velocity for an external observer u_F, it shows that an enlargement of the global flame surface area A_F results in an higher u_F.

Burke et al. [22] experimentally investigated flame propagation in a cylindrical explosion channel with a greater extent in axial direction than in radial direction. A deformation of the flame surface at radial distances near the wall due to the non-spherical confinement of the experimental facility was observed. A higher burned gas velocity $u_{\text{gas,b}}$ behind the flame front was induced in the axial direction of flame propagation compared to the spherical case. This resulted in an enlarged flame surface in axial direction leading to enhanced flame propagation velocity u_F. The authors suggest the formulation of a facility dependent correction factor which accounts for this effect. The dependence of the velocity of the expansion flow behind the flame front on the confinement was also de-

scribed by Beauvais et al. [7].

The global flame surface area can be used as an indicator for the influence of the confinement on the flame propagation process. The larger the global flame surface area, the more unburned gas can be consumed and must be vented downstream through the present cross-sectional area of the facility. This leads to an enhanced burned gas velocity in the direction of flame propagation behind the flame front, resulting in an enhanced observed flame propagation velocity u_F.

The two experiments investigated in this work differ significantly not only in scale, more precisely in the ratio of the geometrical facility dimensions, but also in the experimental setup, like e.g. ignition position or the expected direction of propagation.

The first geometrical difference is the aspect ratio of the channel cross-section, which is formulated as follows:

$$AR_{\text{cross}} = \frac{l_1}{l_2} \tag{6.34}$$

with the channel dimensions l_1 and l_2 and $l_1 > l_2$.

The limiting case of $AR_{\text{cross}} = 1$ results in circular or square shaped cross-section. After the flame front reaches the side walls of the facility, it mainly propagates in one direction. Facilities with such aspect ratios are expected to exhibit a higher potential for the confinement to influence propagation velocity u_F, than facilities with $AR_{\text{cross}} > 1$. In such facilities the flame can propagate for a longer time in a perpendicular direction compared to the main propagation direction.

The second important geometrical difference is the ratio of channel length to hydraulic diameter. This aspect ratio AR compares the preferential direction of flame propagation in the experimental facility l_{max} to the hydraulic diameter:

$$AR = \frac{l_{\text{max}}}{d_h} = \frac{l_{\text{max}}}{\left(4 \cdot \frac{A}{P}\right)} \tag{6.35}$$

with d_h as the hydraulic diameter:

$$d_h = 4 \cdot \frac{A}{P} \tag{6.36}$$

Variable A stands for the cross-sectional area and P for the wetted perimeter of the cross-section. The hydraulic diameter d_h is used for geometries deviating from a circular shape.

Burke et al. [22] state that the higher the aspect ratio AR of the facility (length to diameter in their case) the higher the observed effect of the facility on flame propagation in axial direction.

To investigate the effect of the ratio of channel length to the hydraulic diameter on the propagation process, a numerical parameter study is conducted. Simulational results for varying aspect ratios AR are summarized in Fig. 6.34. The squared cross-sectional area is identical in all simulations ($l_y = l_z$ =0.06 m), leading to identical hydraulic diameters and cross-sectional aspect ratios of $AR_{cross} = 1$ in all investigated cases. The hydrogen concentration in all cases is 13.4% and the initial pressure level is 1 bar. All other physical parameters are chosen according to case B in Tab. 7.3 and according to the summary in Tab. 7.2. The only varying parameter between the depicted simulations in Fig. 6.34 is the aspect ratio AR. Additionally, a simulation with an opening boundary condition at the end wall upstream of flame propagation is shown to emphasize the effect of the end wall on the flame propagation process.

Initially, the flame surface area develops identically for all aspect ratios AR and is increasing with time. After this initial increase a peak occurs, and the flame surface area decreases again. The increase of flame surface area results from the enlarged flame surface in the main propagation direction. The propagating flame front is not planar, but rather has a finger-like shape. The decrease in flame area is due to flattening of the global flame shape in later stages of propagation. The higher the aspect ratio AR, the higher the peak level of the global flame surface area due to the reduced influence of the end wall on the propagating flame front. The peak levels of ratios AR =43 and AR =65 are similar, indicating that the effect of channel length on the initially developing global flame sur-

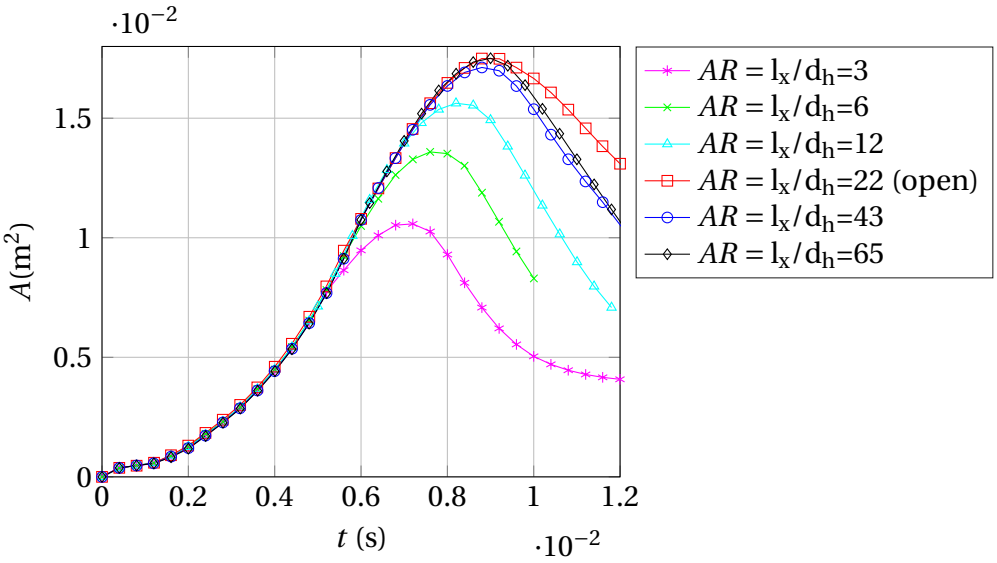

Figure 6.34: Flame surface area development over time for different channel length to hydraulic diameter ratios AR.

face area exhibits a limit. Beyond a certain aspect ratio AR, the influence of the end wall on the initially developing flame surface area seems to vanish. This observation is supported by the simulation with an opening boundary condition at the end wall upstream of flame propagation for an aspect ratio of $AR = 22$. The flame surface area in this simulation exhibits a similar peak level to the simulations with aspect ratios of AR =43 and AR =65. This parameter study qualitatively indicates an influence of the channel aspect ratio AR on the flame propagation process.

The higher the value of AR, the greater the deviation of the experimental facility from the spherical form. The facility is stretched in one direction compared to the other two perpendicular directions. According to Burke et al. [22], it can be assumed the higher the value of AR, the greater the influence of the experimental facility on global flame propagation behavior. Fig. 6.34 indicates an asymptotically reached limit value of AR where the influence of the upstream end wall on flame propagation seems to vanish. For values of AR significantly lower than the limit value, the effect of global flame surface enlargement appears to be compensated by the influence of the end plate on the unburned gas flow. The flame front does not develop such large flame surface areas as seen in Fig 6.34 for an $AR = 3$. The lower limit of AR is 1, describing a spherical experimental

facility.

The experimental facilities investigated in this work can be characterized based on the prior formulated aspect ratios AR_{cross} and AR. However, the experimental setup, such as ignition position or the expected direction of propagation must be considered as well, since these factors also influence the flame propagation process and therefore the observed propagation velocity u_F.

6.7.2 Formulation of test facility specific factor

The small-scale GraVent explosion channel exhibits a cross-sectional aspect ratio AR_{cross} as follows:

$$AR_{cross} = \frac{l_1}{l_2} = \frac{l_y}{l_z} = 5 \tag{6.37}$$

The value of $AR_{cross} > 1$ indicates that the cross-section of the GraVent facility is deviating from the square shape.

The ratio of channel length to the hydraulic diameter AR is as follows:

$$AR = \frac{l_{\max}}{d_h} = \frac{l_x}{\left(4 \cdot \frac{A}{P}\right)} = 13 \tag{6.38}$$

The global flame propagation in the GraVent facility is predominantly in one direction and the experimental facility is expected to influence the flame propagation process. The global flame area during flame propagation is expected to be significantly larger than the channel cross-section.

According to Burke et al. [22], the effect of the confinement on the flame propagation process should be formulated concentration dependent, since the accelerating effect of the expanding burned gas across the flame front is dependent on mixture concentration. The volume of burned gas vented downstream is dependent on the density ratio σ across the flame front.

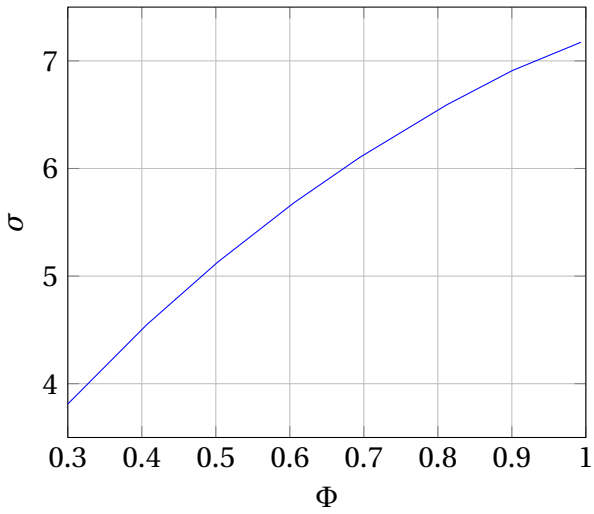

Figure 6.35: Density ratio σ over varying concentration.

In Fig. 6.35 the ratio of the density of the unburned and the burned gas σ, defined in Eq. 2.2, is plotted for a varying concentration showing that the density of the gas drops significantly across the flame front. The ratio increases at concentrations closer to the stoichiometric ratio. The trend for σ over Φ shown in Fig. 6.39 can be reproduced by the following polynomial fit:

$$\sigma = -3.25\Phi^2 + 9.05\Phi + 1.4 \tag{6.39}$$

For simulations of flame propagation in the GraVent facility, the test facility specific factor B was chosen as follows:

$$B = 0.5 \cdot \sigma \tag{6.40}$$

The formulation of Eq. 6.40 is based on fitting the simulational results to the experimentally determined propagation velocities. Despite this simple approach, the formulation allows a reproduction of the experimental results of the GraVent facility under varying concentrations. It is important to note that the formulation of parameter B in Eq. 6.40 is determined for the specific dimension ratios of the investigated GraVent setup and therefore is a function of concentration and dimension ratios.

The THAI facility exhibits not only significantly different geometrical di-

mensions and aspect ratios than the GraVent facility, but also the experimental setup is different.

The THAI facility exhibits the following cross-sectional aspect ratio AR_{cross}:

$$AR_{cross} = \frac{l_1}{l_2} = \frac{D}{D} = 1 \tag{6.41}$$

The ratio of channel length to hydraulic diameter AR reads as follows:

$$AR = \frac{l_{\max}}{d_h} = \frac{l_x}{D} = 2.92 \tag{6.42}$$

with d_h as the geometrical diameter D of the THAI facility.

Comparing the cross-sectional aspect ratios AR_{cross} of the GraVent and the THAI facility, the degree of confinement through the cross-sectional area is assumed to be higher in the THAI facility, as it exhibits $AR_{cross} = 1$. However, due to the experimental setup this effect is assumed to play a minor role. The ignition position in the THAI facility is not directly at the wall, as seen in Fig. 7.10. This leads to flame propagation in all directions in the initial phase. Additionally, buoyancy enhances the ascending of the burned gas plume. This effect allows for longer downward flame propagation before reaching the facility walls. Simulations show unburned volume in the lower part of the facility at later stages of propagation [38]. Based on the low aspect ratio AR the end plate is expected to have a significant effect on flame propagation much earlier than in the GraVent facility. Therefore, the main focus is on the initial phase of flame propagation in the THAI facility, where the effect of confinement on flame propagation velocity u_F is expected to play a minor role. Based on this, a value of $B = 1$ is chosen for flame propagation simulations in the present work.

The assumption of $B = 1$ is consistent with the concept of the new modeling approach, where effects that are assumed to play a minor role are set to a value of unity and therefore do not influence other accelerating effects.

The test facility specific factor B should be determined for each investigated facility. Experimental investigation of the influence of varying aspect ratios on the flame propagation process was not feasible in the present work. However, estimates based on the two experiments and the numerical parameter study are possible. With increasing AR_{cross} the effect of confinement on flame propagation is decreasing, due to the lower degree of confinement. With increasing AR the influence of confinement on flame propagation increases until a limit value is reached asymptotically. For other facilities with a dimension ratio AR between the two experimentally investigated cases, the parameter B should be chosen between 1 and the concentration and AR_{cross} dependent corresponding value of the GraVent facility $\sigma/2$. For aspect ratios below the calculated value of $AR = 2.92$ of the THAI facility, the parameter B should be 1. For larger aspect ratios AR than in the GraVent facility, the effect of the confinement on flame propagation is expected to be larger, leading to larger values of B. For aspect ratios larger than the asymptotically reached limit value of 65, no further increase of parameter B is expected.

7 Model validation

To analyze the performance and validate the newly developed modeling concept, transient simulations of lean hydrogen-air combustion are conducted and the results are compared to experimental data. The software package ANSYS CFX [5] is used throughout all URANS simulations.

The comparison between the simulation results and the experimental data is based on velocity-distance diagrams (v-x diagrams). This method is more sensitive than the comparison based on x-t diagrams because the calculation of the velocities is based on the differential quotient, according to Eq. 3.1. For the calculation of the flame propagation velocities in the simulations the flame tip is used as the reference point. In all cases the flame tip propagates along the center channel axis until the end plate starts to affect and deaccelerate the flame front. The data from the simulations is averaged over a time interval chosen in a way to avoid numerical scatter in the plots, and at the same time to provide a reasonable approximation of the flame velocity. The time interval length is based on the flame velocity in the investigated case, resulting in shorter averaging intervals in fast flames and longer intervals in slow flames.

The validation of the new modeling concept starts with small-scale simulations of the GraVent facility without turbulence generating obstacles. A wide concentration range is investigated to demonstrate the performance of the model. Following that, a simulation with obstacles is conducted to check the performance of the modeling concept when turbulence is the main driver for acceleration. Finally, a large-scale simulation of the THAI facility is conducted to show the applicability of the modeling concept to different scales.

7.1 Small-scale simulations without obstacles

7.1.1 Simulation setup and physical models

The simulations presented in this section are focused on the reproduction of the flame front propagation velocity and not on resolving the detailed flame front characteristics. As a result, the two symmetry planes (x-y and x-z; see Fig. 3.2) of the explosion channel are utilized to reduce computational cost. Fig. 7.1 shows the computational domain consisting of a quarter of the channel cross section along the entire channel length.

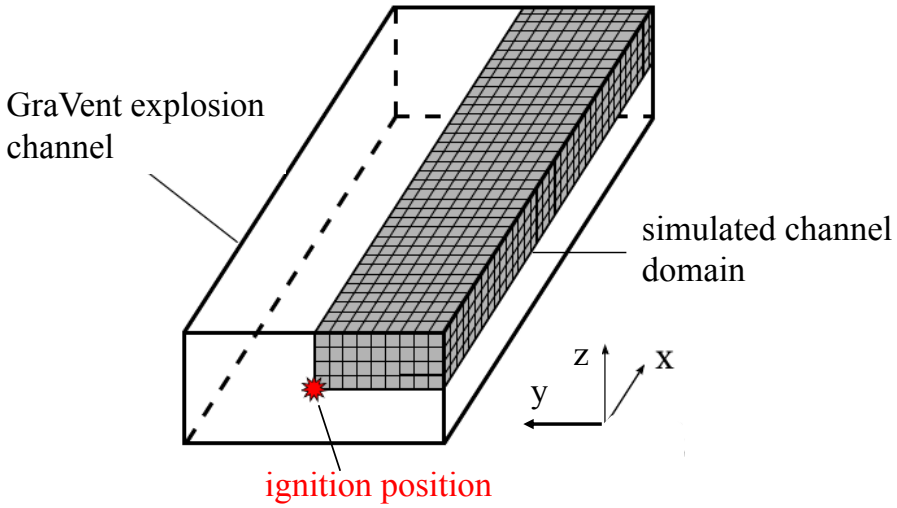

Figure 7.1: Depiction of the simulated domain of the GraVent explosion channel adapted from [38].

By utilizing the symmetry planes of the channel, the simplification of the simulation model is assumed to have minimal influence on the flame propagation velocity. Case e in Fig. 7.2 and Tab. 7.1 serves as the reference setup used throughout the present work. Simulations using the entire channel volume as the computational domain (case d) have been conducted and no significant difference of the propagation velocity was identified compared to the reference case, as can be seen in Fig. 7.2. Furthermore, the simulations in the small-scale channel are conducted without buoyancy effects. This simplification is based on the small height of the channel compared to the channel length, the main direction of flame propagation. Nevertheless, simulations under the influence of

buoyancy have been conducted to justify this assumption (Fig. 7.2, cases a and d). The velocity-distance diagrams derived from simulations with buoyancy depicted in Fig. 7.2 showed no significant deviation in comparison to those with no buoyancy.

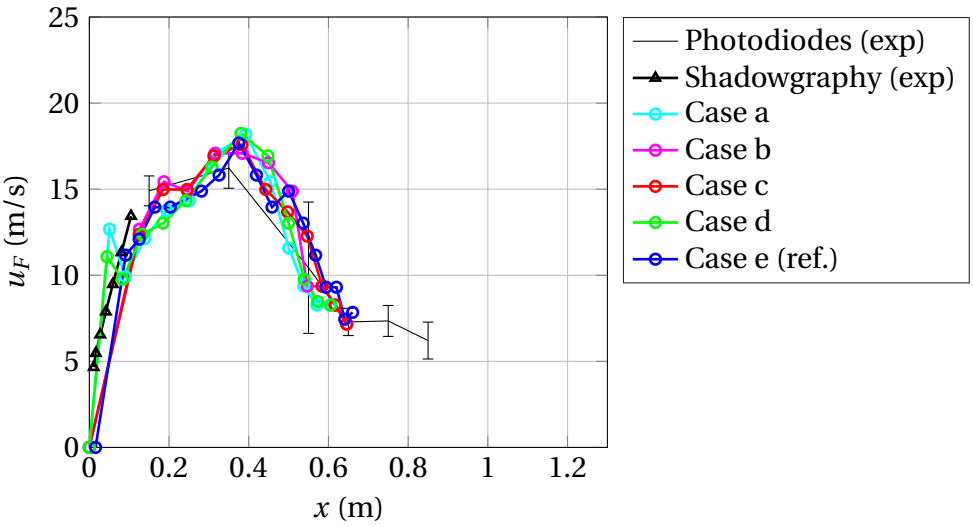

Figure 7.2: Comparison of simulational and experimental results for a concentration of 13.4% and an initial pressure level of 1 bar. The simulational data corresponds to the cases described in Tab. 7.1.

Table 7.1: Case overview of simulations shown in Fig. 7.2. The row "Opening" indicates if an opening in the computational domain according to the description in Sec. 7.1.3 was considered in the simulation or not.

Case	Computational Domain	Buoyancy	Radiation	Opening
a	half (x-z-plane sym.)	yes	no	no
b	half (x-z-plane sym.)	no	no	yes
c	quarter (x-z- and x-y-plane sym.)	no	yes	no
d	full (no sym.)	yes	no	no
e (ref.)	quarter (x-z- and x-y-plane sym.)	no	no	no

A structured computational grid with hexahedral elements is used throughout the entire validation process. The cell size varies in the range of 2 mm to 30 mm. This range is limited by calculation cost on the one hand (case with 2 mm grid resolution) and by the channel height itself on

the other hand (case with 30 mm grid resolution; two cells across channel height). The simulation on the 2 mm grid is carried out for the initial phase only, due to the immense computational cost.

The walls of the computational domain are modeled using an adiabatic no slip boundary condition. Radiation of the flame front is assumed to have minor influence on the flame propagation velocity and is therefore neglected in the simulations. To confirm this assumption, velocity-distance diagram derived from a simulation with radiation (case c) is compared to the cases without radiation in Fig. 7.2. The radiation in the simulations was modeled utilizing the P1 radiation model [97] according to the approach in Schramm et al. [99] and Schramm et al. [98]. No significant influence on global flame propagation velocities could be identified.

The initial conditions in the simulations are selected according to the initial conditions in the experiment. The initial pressure is set to $p^0 = 1$ bar and the initial temperature to $T^0 = 293$ K. The SST turbulence model is used throughout all simulations and the initial turbulence level is set to $k^0 = 1e{-}04$ m^2/s^2 with an eddy-viscosity-ratio of $\mu_t/\mu = 10$. A wide range of different initial turbulence levels was tested but no significant impact on the flame propagation process could be identified.

The CFX high resolution advection scheme and the built-in Second Order Backward Euler transient scheme with adaptive time stepping are used in all simulations. The initial time step is $t^0 = 1e-06$ s. The MAX residuals of the solved equations are chosen as the convergence criteria for the simulations. This type of residual is the appropriate choice in unsteady simulations according to [5]. The simulations show good convergence behavior, reaching residual levels between $1e{-}03$ and $1e{-}04$. Simulations with tighter convergence criteria were conducted as well, however without influence on the predicted flame front velocities. Therefore, the less strict convergence criteria are chosen because of the significantly lower computational cost.

Table 7.3 summarizes the investigated cases in the small-scale GraVent explosion channel. The concentration varies from 11 to 19.1%. The case with a concentration of 13.4% was simulated with varying grid sizes and

Table 7.2: Summary of the simulation setup of the small-scale GraVent facility.

	Parameter	Value	Remark
Physical models	Turbulence Model	SST	Initialisation: k=0.0001 epsilon=0.0001
	Grid	Structured	2; 7.5; 15; 30 mm
	Bouyancy	No	
	Radiation	No	
Solver settings	Timestep	Adaptive	Min. value 1e-06
	Convergence Criteria	MAX Residuals	< 1e-03
	Advection Scheme	High Resolution	
	Transient Scheme	Second Order	
Boundary conditions at the wall	Heat Transfer	Adiabatic	
	Mass and Momentum	No Slip Wall	
	Wall Roughness	Smooth Wall	
	Wallfunction	Automatic	

the case with 15% was additionally investigated under the influence of turbulence generating obstacles.

Table 7.3: Overview of investigated simulation cases.

case	concentration (%)	grid size (mm)	obstacles
A	11	7.5	no
B	13.4	7.5	no
C	15	7.5	no
D	19.1	7.5	no
E	15	6	yes
F	13.4	2	no
G	13.4	15	no
H	13.4	30	no

7.1.2 Velocity-distance diagrams

Figure 7.3 shows experimentally determined velocity over distance. The data is based on the combination of shadowgraphy recordings and photodiode measurements. In the optically accessible front part of the channel shadowgraphy was used with a time resolution of 20 kHz. In the rear part of the channel where no optical access is possible photodiode measurements were conducted. The experimental photodiode data is based on three experimental runs. Confidence intervals are shown in the plots.

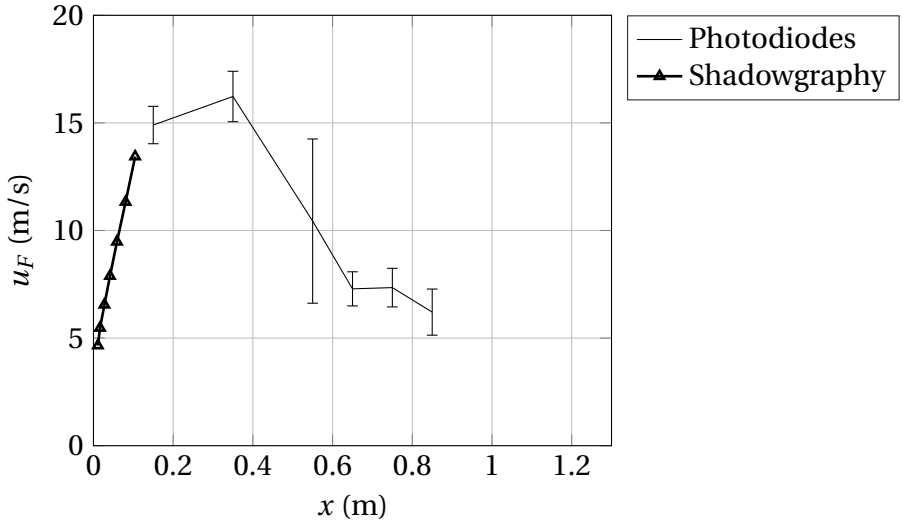

Figure 7.3: Experimental velocity-distance data for a concentration of 13.4% and an initial pressure of $p^0 = 1$ bar. Additionally, standard deviations are depicted for the photodiode data.

The experiments showed the velocity increasing in the initial phase of flame propagation. At a distance of approx. 0.4 m the velocity reaches the peak value, then decreases to a lower level and remains at this level until the end of the experimentally investigated distance. Since the propagation velocity does not change significantly anymore, the simulations were conducted until the flame front reached this velocity plateau in the middle part of the channel.

The reason for this velocity profile, which can be observed in all investigated cases under varying concentrations, is the influence of the end plate on the fresh gas flow ahead of the flame front. The measured velocity u_F is the propagation velocity of the flame front with respect to

an inertial coordinate system, according to Eq. 2.22. It is the sum of the burning velocity and the fresh gas flow velocity ahead of the flame front. The fresh gas ahead of the flame front is pushed forward by the flame front itself and moves in the same direction as the flame front. Due to this piston effect both velocities are superimposed. At a distance of approximately 0.6 m the fresh gas flow propagating ahead of the flame has reached the end of the channel. The fresh gas cannot propagate further and is compressed. Therefore, the velocity of the fresh gas flow drops significantly, resulting in a lower superimposed velocity measured by the stationary observer.

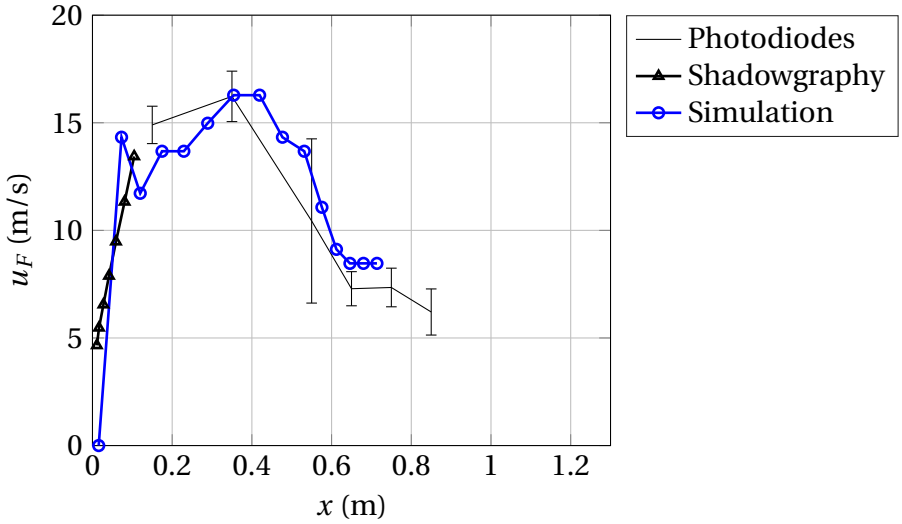

Figure 7.4: Velocity over distance obtained through a simulation compared to experimental data for a concentration of 13.4% and the reference grid size of 7.5 mm.

Figure 7.4 compares simulational and experimental results for case B according to Tab. 7.3. The velocity of the flame front is plotted over the distance for a hydrogen concentration of 13.4%. The grid size used in the simulation was 7.5 mm. It can be observed that the simulation reproduces the velocity profile very well. The peak level and the distance where the velocity decreases are in accordance with the experimental results.

In the next step, simulations with varying grid sizes are conducted. Fig. 7.5 compares the simulational results for the cases B, F, G and H (Tab. 7.3) with the experimentally determined velocity profile. The grid size variation encompasses grid sizes from 2 mm to 30 mm. The simulations on

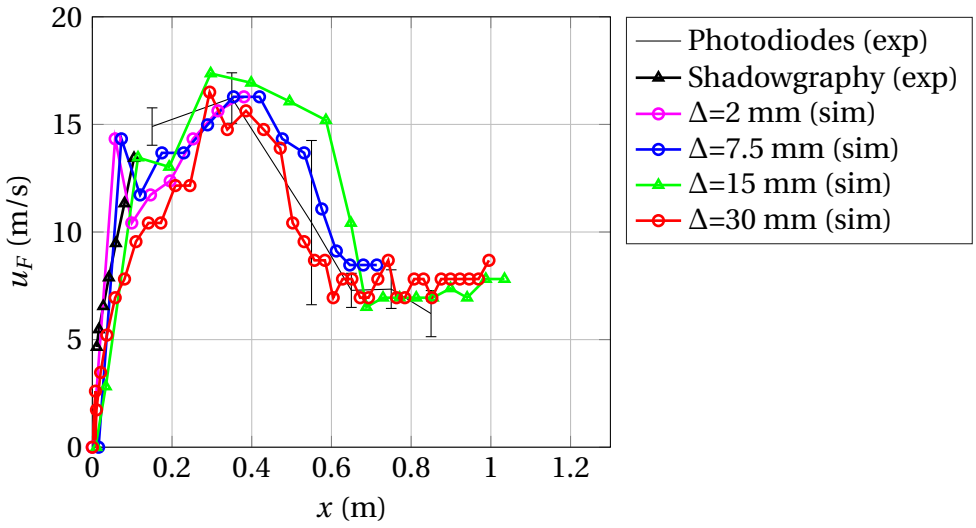

Figure 7.5: Comparison of simulational and experimental results under varying grid size for a concentration of 13.4%.

varying grid sizes are able to reproduce the experimental data qualitatively and quantitatively in a satisfactory way.

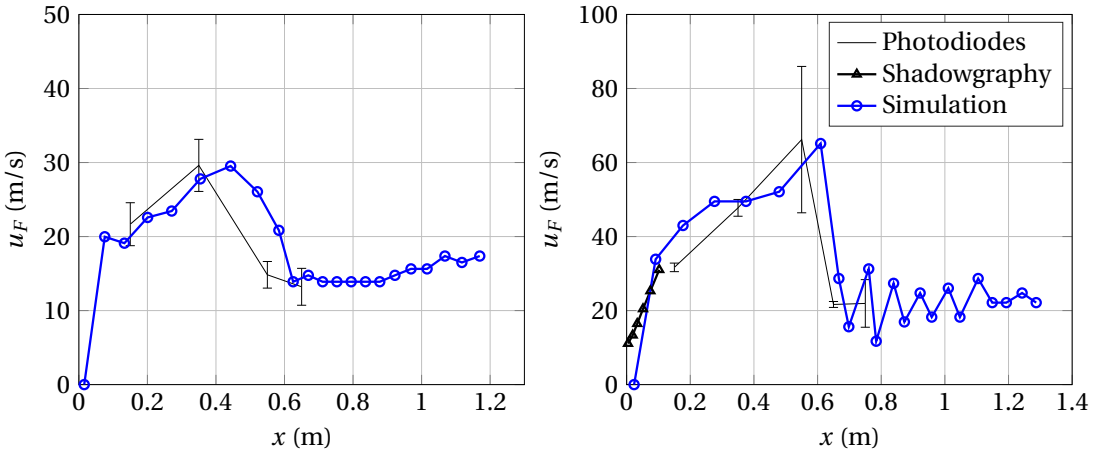

Figure 7.6: Simulations compared to experimental data for concentrations of: on the left: 15%; and on the right: 19.1%.

Figure 7.6 compares simulational and experimental results for higher hydrogen content of the mixture. Velocity-distance profiles of mixtures with hydrogen concentrations of 15% on the left side and 19.1% on the right side are shown. The simulations correspond to cases C and D in Tab. 7.3. The experimental results under varying concentrations exhibit a qualitative velocity-distance behavior similar to the 13.4% case. As expected,

the peak velocities are increasing with increasing hydrogen content due to the higher laminar burning velocities for the mixtures with higher hydrogen content. Again, the simulations predict the velocity profiles very well.

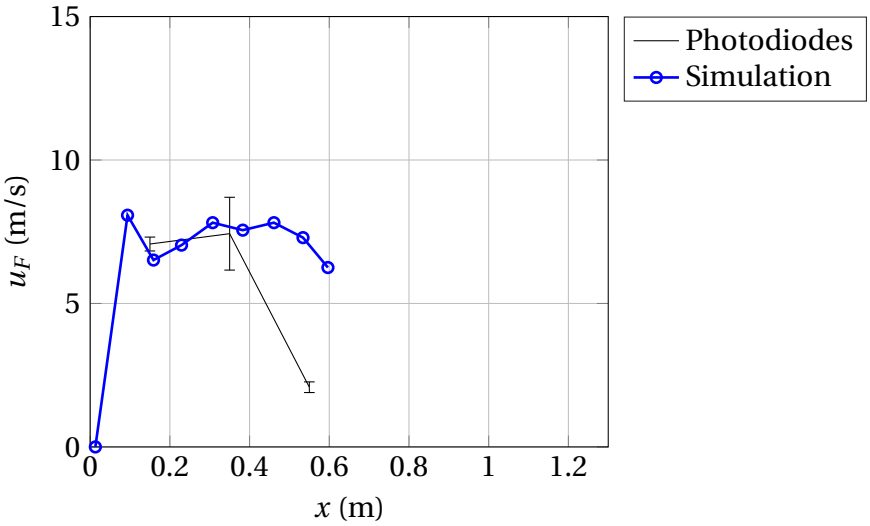

Figure 7.7: Simulations compared to experimental data for a concentration of 11% at reference grid size of 7.5 mm.

Figure 7.7 compares the simulational and experimental results for a lower hydrogen content than 13.4%. The investigation of lower hydrogen concentrations was not possible because of the employed measurement setup, which was not able to detect slower flame fronts. As can be seen, the new model predicts the peak velocity correctly.

It can be summarized that the new modeling concept is able to predict the velocity profiles of propagating flame fronts over a wide concentration range. With B as the facility correction factor it was possible to reproduce velocity distance diagrams of mixtures with propagation velocities differing up to one magnitude. Additionally, the implemented treatment of varying grid sizes showed adequate performance in a wide range of different grid sizes.

7.1.3 Pressure-time diagrams

The reproduction of the pressure signal from the experiment turned out to be a significant challenge in the simulations. Because of the constructional characteristics of the GraVent facility it does not qualify for precise pressure measurements in cases with slow flame propagation and small pressure build-ups. Due to the slow flame propagation and the ignition of the mixture in the optical segment, leakage to the venting volume below the explosion channel occurred. The influence of the venting volume on the pressure development was significant.

The optical segment exhibits narrow gaps along the window inserts due to its design, through which gas exchange can take place between the explosion channel and the venting volume. To reduce the influence of this gap as much as possible, the venting volume was filled with wax. This measure had a positive influence on the pressure measurement, but the effect of the venting volume could not be completely eliminated.

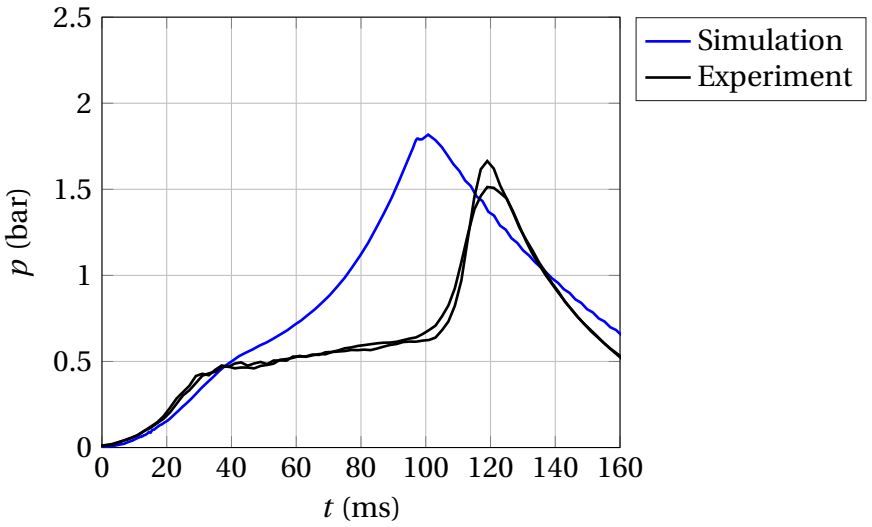

Figure 7.8: Comparison of experimentally determined and simulational pressure-time data for a concentration of 13.4%.

Figure 7.8 shows the time trace of the pressure determined in the simulation and the measured pressure signal for three experiments. The pressure in the experiment initially increases strongly and flattens out again at about 30 ms. Afterwards the pressure curve is almost constant until it suddenly rises to the maximum value at approximately 110 ms and then

drops again.

In order to correspond to the constructional characteristics of the GraVent facility, the calculation grid was modified for this particular case. An opening boundary condition with a total area of 15 mm^2 was inserted into the computational domain. This boundary condition modeled the gas exchange with the venting volume. The location was chosen similar to the position of the assumed largest leak from the explosion channel to the venting volume below, at a distance of x=0.23 m between the removable lateral window and the test facility itself (see Fig. 3.2). This modification of the calculation grid had no significant effect on the flame propagation velocity, as can be seen in Fig. 7.2, case b. However, the pressure trace could be reproduced qualitatively and quantitatively in a satisfactory way. Due to this inherent characteristic of the GraVent test facility the investigation of pressure traces is limited to the already discussed case.

7.2 Small-scale simulations with obstacles

7.2.1 Simulation setup

Since flame propagation under the influence of obstacle generated turbulence is not the focus of this project, but the influence of turbulence on the flame propagation process must be considered for the applicability of the model, an experiment from the DDT-Database [12] has been simulated and compared with the experimental data. A setup with obstacles, combined with the lowest available hydrogen concentration in the database was chosen for this. This way it could be shown that the developed modeling concept is applicable when turbulence is the main reason for flame acceleration and even in that case, the influence of flame instabilities on the initial flame propagation phase must still be considered.

The experimental setup differs from the setup used for model development introduced in Sec. 3.1. Tab. 7.4 summarizes channel setup of the simulated case with obstacles. The notation BR30S300 stands for a block-

age ratio of 30% with an obstacle spacing of 300 mm. The obstacles are placed in the channel section between 0.25 m and 2.05 m distance downstream of the ignition position. The overall channel length in this setup is 5.1 m.

Table 7.4: Explanation of the notation of the investigated case with obstacles.

case	blockage ratio (%)	obstacle distance (m)	obstacle section (m)
BR30S300	30	0.3	0.25 - 2.05

The setup of the physical models in this investigation is identical to the setup shown in Tab. 7.2. The computational grid is a structured grid with hexahedral cells with an edge length of 6 mm. This way cells with identical sizes could be used throughout the simulational domain. The simulations are conducted utilizing the new modeling concept (Eq. 6.2) and a validated flame speed model from literature where turbulence is the main acceleration mechanism according to Peters [87].

7.2.2 Velocity-distance diagram

The experimental data set shown in Fig. 7.9 consists of three experimental runs. The flame front acceleration is significantly greater under the influence of turbulence generating obstacles than in the case without obstacles. The flame front accelerates up to a peak velocity value of approximately 350 m/s. After this peak value, the velocity drops again since no turbulence generating obstacles are mounted in the rear part of the channel. The velocity-distance data determined in simulations is compared with experimentally determined data. Additionally, the predicted flame speed according to the new correlation is compared to the prediction following Peters [87]. The acceleration of the flame to velocities of up to 350 m/s is reproduced correctly with the new correlation. Furthermore, the position of the velocity maximum at the correct position is reproduced. This shows that not only the influence of turbulence but the combination of all other accelerating effects must be considered.

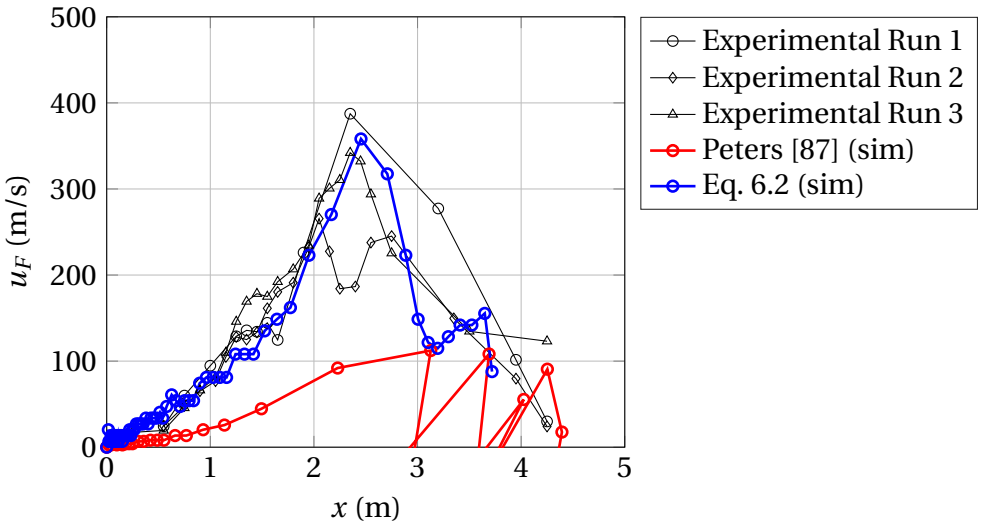

Figure 7.9: Comparison of simulations utilizing the new formulation and the formulation according to Peters [87] with experimental data for a concentration of 15% at reference grid size of 6 mm for the configuration BR30S300.

7.3 Large-scale simulations

Finally, simulations on a scale significantly larger than the scale of the GraVent facility are conducted to verify the applicability of the developed modeling concept on a range of scales. For this purpose the THAI facility [2] [99] has been chosen due to the similarity of the conducted experiments, however on a larger scale.

7.3.1 Simulation setup

The THAI facility is a 9.2 m high vessel with rotational symmetry and a maximum diameter of 3.15 m. The main dimensions and the ignition location are shown in Fig. 7.10. Additionally, locations of temperature probes are depicted, which are used to determine the point in time of the passing flame front. This data is used to calculate the propagation velocity of the flame front.

The simulated experiment exhibits a hydrogen concentration of 10% and corresponds to the HD7 case in [99]. It is assumed that the hydrogen is

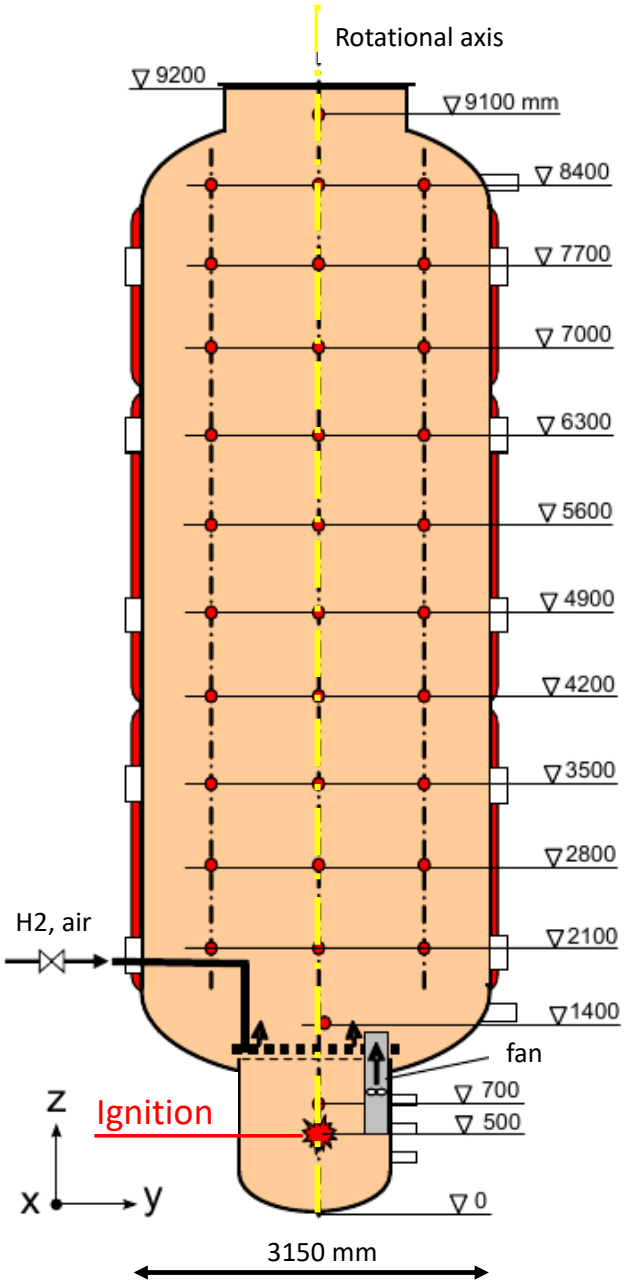

Figure 7.10: Depiction of the main dimensions of the THAI facility. Additionally, temperature measuring points used for determination of the velocity are shown. Depiction adapted from [2].

homogeneously distributed in the vessel domain and the initial turbulence level is negligibly low. No turbulence generating obstacles are installed in the vessel domain in the investigated case. The mixture is ignited at a height of 0.5 m from the bottom in the vessel center. The initial temperature is set to 291 K and the initial pressure level is set to 1.492 bar,

according to the experiment.

After ignition, the flame front propagates in all spatial directions away from the ignition location. The THAI facility allows the flame front to propagate in the vertical direction, which makes the buoyancy model necessary in the simulations. Simulations considering radiation have been conducted and no significant influence on the flame propagation velocity was identified. Therefore, the influence of radiation is not considered in the subsequent simulations in order to significantly lower computational costs. Tab. 7.5 summarizes the setup used in the simulations of the THAI facility.

Table 7.5: Summary of the simulation setup for large-scale simulations.

	Parameter	Value	Remark
Physical models	Turbulence Model	SST	Initialisation: k=0.0001 epsilon=0.0001
	Grid	Structured	Variabel
	Bouyancy	Yes	
	Radiation	No	
Solver settings	Timestep	Adaptive	Min. value 1e-06
	Convergence Criteria	MAX Residuals	< 1e-03
	Advection Scheme	High Resolution	
	Transient Scheme	Second Order	
Boundary conditions at the wall	Heat Transfer	Adiabatic	
	Mass and Momentum	No Slip Wall	
	Wall Roughness	Smooth Wall	
	Wallfunction	Automatic	

The simulations are performed on a structured grid of the entire THAI facility. Rotational symmetry is not used to reduce computational costs. The cell sizes and shapes vary slightly throughout the computation domain because of the more complex geometry of the THAI facility compared to the GraVent facility.

7.3.2 Velocity-time diagrams

After ignition, the flame propagates initially in all spatial directions until the lateral vessel walls are reached. After that, the flame propagates mainly in the vertical upward direction. The evaluation of the flame velocities in the simulations is conducted along the rotational symmetry axis in the center of the vessel, shown in Fig. 7.10.

The evaluation of the experimental data is based on the distance-time information of the flame front arriving at the temperature probes mounted in the vessel domain (shown in Fig. 7.10) [99]. The velocity-distance diagrams are then derived from the position and time information of the flame front following Eq. 3.1.

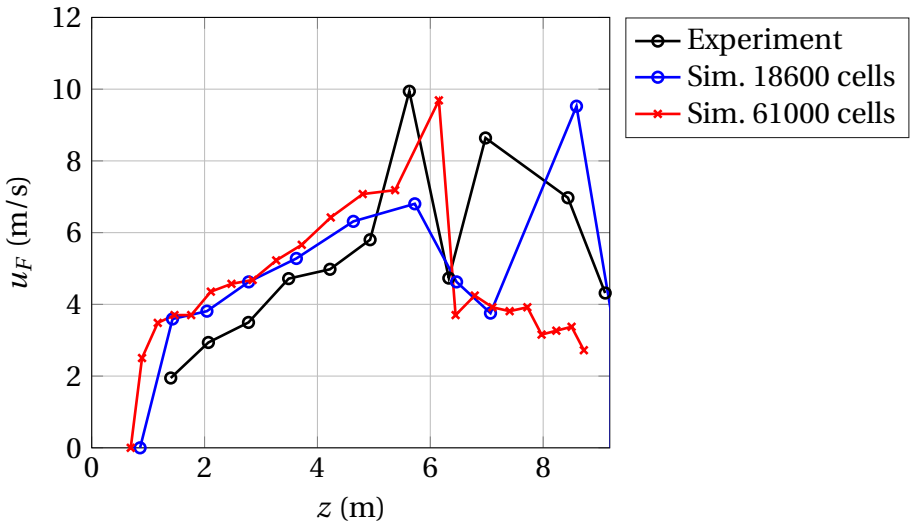

Figure 7.11: Comparison of velocity-distance data from experiment and simulation.

In Fig. 7.11 experimental velocity-distance data is shown. The flame front is accelerating along the rotational axis upwards in the vertical direction. Propagation velocity of the flame front above 6 m is not meaningful because the flame does not propagate in the vessel center [99]. At these distances, the vessel top wall influences the flame propagation process.

The velocity-distance data obtained through two simulations with varying cell numbers are compared with the experimental data. The simulations adequately reproduce the experimental results up to the meaning-

ful distance of approximately 6 m. Additionally, the variation of the cell numbers has minor effect on the propagation velocity due to the implemented treatment, discussed in Sec. 6.5.

7.3.3 Pressure-time diagrams

Figure 7.12 shows the pressure development during the experiment and the simulations plotted over time. Additionally, the initial pressure level $p^0 = 1.492$ bar and the calculated theoretical final pressure level $p_{\mathrm{AICC}} = 6.4$ bar are shown. The experimental pressure starts increasing at about 1.5 s and reaches the peak level around 2.7 s and starts decreasing again. Due to the slow propagation of the flame, the pressure increases homogeneously in the whole vessel during the experiment. The experimentally determined pressure does not reach the theoretical peak value which is due to heat loss through non-adiabatic walls in the experiment.

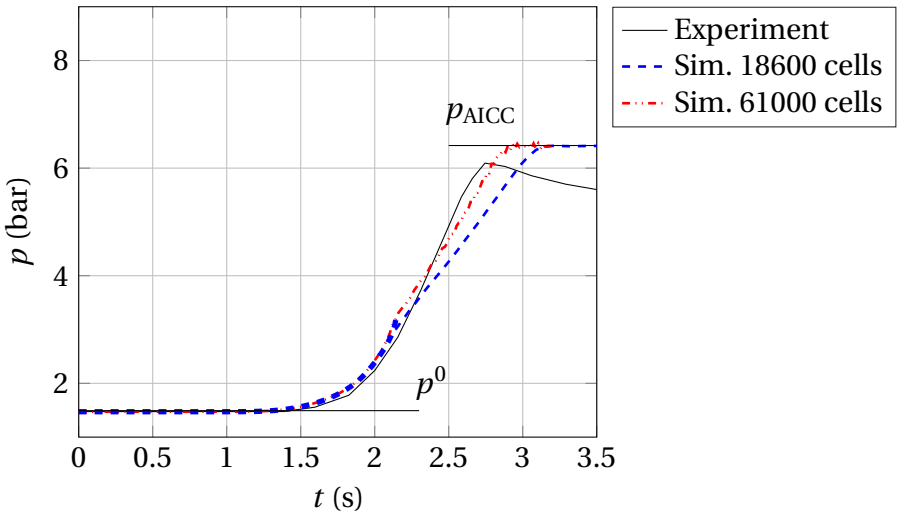

Figure 7.12: Comparison of pressure development in the simulations and the experiment.

The pressure-time results from the simulations are compared to the experimentally determined data. The maximum value and the position of the maximum value in time are in very good agreement with the experiment when the test facility correction factor is chosen to $B = 1$. The decrease of the pressure signal after the flame front reached the top wall is not reproduced in the simulation due to the adiabatic wall modeling.

8 Summary

The overall goal of this work was to develop a new modeling concept for lean hydrogen-air flames in quiescent mixtures. For this purpose, flame acceleration experiments have been conducted in a small-scale explosion channel with negligible turbulence levels.

The measurement strategy used combined conventional techniques like photodiodes and dynamic pressure transducers and optical techniques, such as shadowgraphy and OH-PLIF measurements. The results of the conventional measurement techniques were also used for model validation. The optical measurement techniques were employed to gain insight and to quantitatively assess flame wrinkling. Additionally, highly resolved simulations have been conducted to complement the experimental data. This way, the pressure influence on flame front wrinkling could be investigated.

For the evaluation of the experimental data gathered with optical measurement techniques and the evaluation of the numerical data from the highly resolved simulations, automatic evaluation routines were developed. These routines allowed on the one hand the detection of the real wrinkled flame front and on the other hand the calculation of a filtered flame front without small-scale flame front wrinkling. Furthermore, a routine has been developed which allowed the evaluation of the local curvature of the flame front.

The acceleration mechanisms have been summarized in a semi-empirical correlation and validated through small-scale and large-scale simulations. The flame propagation predicted in the simulations was compared to experimental data, showing satisfactory flame acceleration behavior. The following sections discuss the results in more detail.

8.1 Experiments

Lean hydrogen-air flames under varying initial pressure were investigated in several measurement campaigns. The focus of the experiments was the investigation of the initial propagation behavior of homogeneous hydrogen-air mixtures in a smooth channel with a negligible initial turbulence level. The following summarizes the results of these experiments:

- Small-scale wrinkling of the flame front due to intrinsic instabilities was observed and evaluated qualitatively and quantitatively. As expected, shadowgraphy images show that the flame front wrinkling is more pronounced the leaner the mixture. This observation was confirmed quantitatively by evaluation of OH-PLIF images.
- The length scale of the local cellular structure of the flame front decreases with increasing pressure. A quantitative evaluation showed that the decrease of the length scale with increasing pressure is accompanied by an increase of the flame surface area.
- The convex curvature of the local flame front towards the fresh gas due to the intrinsic instability effects led to probability density distributions with peak values shifted to positive values, resulting in a positive skewness of the PDFs.

8.2 Modeling

Based on these results an algebraic model was formulated, capturing the identified flame accelerating effects. The modeling efforts are summarized as follows:

- The chosen mathematical structure of the new formulation ensures a robust limit value behavior if the influence of an effect on flame acceleration is small or negligible. In this case, the new formulation still produces correct results for the remaining accelerating effects.

Furthermore, the structure of the new formulation allows for extension to further accelerating effects if required.

- Laminar burning velocity is a key parameter in the new modeling concept. A suitable correlation for lean unstretched hydrogen-air flames is formulated based on experimental data found in the literature. The influence of pressure and temperature on the laminar burning velocity is quantified by CANTERA calculations and integrated into the modeling concept.

- Flame surface enlargement due to small-scale flame wrinkling was linked to an effective Lewis number formulation. The detected influence of pressure on flame surface enlargement is considered in the modeling approach.

- The laminar burning velocity along the wrinkled flame front of lean hydrogen-air flames is locally not constant due to flame stretch effects. In areas where the flame front is convex towards the fresh gas, the laminar burning velocity significantly increases depending on the local stretch rate and the Markstein length. This effect is incorporated in the new model with a non-linear relationship between the stretched and unstretched burning velocity.

- The influence of turbulence on flame acceleration could not be investigated in the current setup of the experimental facility. The influence of turbulence was included through an appropriate correlation from literature. The correlation according to Peters [87] was identified as appropriate since this correlation accounts for the accelerating effect of turbulence alone.

- In order to minimize the grid size sensitivity of the simulations, the evaluation of the flame surface enlargement factor from experimental data was carried out using varying evaluation grid sizes. A dependency of the flame surface enlargement factor on the evaluation grid size could be identified. With decreasing evaluation grid size, the flame surface enlargement factor also decreased. The inverse occurred when the evaluation grid size was increased. Based on the assumption that the filtered flame fronts from experiments are similar to flame fronts reproduced on computational grids of equivalent

grid size, a factor capturing the observed dependency of the flame surface enlargement factor on the evaluation grid size was formulated. That way the sensitivity of the simulations regarding the grid resolution could be reduced significantly.

- The influence of the test facility on the flame propagation process was incorporated into the model through factor B. In the case of flame propagation in a channel with a high aspect ratio AR (GraVent), the modeling constant was linked to the density ratio σ. When flame propagation occurred in a facility with a low aspect ratio AR (THAI), the influence of the confinement on flame propagation was assumed to be negligible and parameter $B = 1$ was chosen in accordance with the general modeling concept in this work.

8.3 Validation

The validation of the new modeling concept was based on the reproduction of velocity-distance diagrams derived from experiments. In the first step, simulations of the small-scale GraVent explosion channel were conducted:

- Simulations in the concentration range from 11 to 19.1% showed satisfactory results concerning the flame acceleration behavior. The new correlation was able to reproduce the characteristic velocity-distance diagrams qualitatively and quantitatively.
- Simulations on varying grid sizes from 2 mm to 30 mm were conducted and it was demonstrated that the grid sensitivity has been reduced significantly through the developed treatment.
- Finally, a configuration with turbulence generating obstacles was examined at a concentration of 15%. The simulation employing the new modeling concept successfully reproduced the experimental data. Furthermore, a simulation has been conducted solely considering turbulence as the acceleration mechanism. The velocity-distance diagram could not be reproduced and it was shown that

the identified acceleration mechanisms in the early stage of flame propagation play a crucial role in lean hydrogen-air mixtures.

In the final phase, simulations of flame propagation in the THAI facility were performed. Since the THAI facility exhibits significantly larger dimensions than the GraVent facility, the performance of the developed modeling concept could be tested on a broad scale range:

- A simulation of flame propagation at a concentration of 10% and an initial pressure of 1.495 bar has been conducted and compared to experimental data. The new model was able to reproduce the velocity-distance behavior.
- The pressure development over time occurring in the experiment could be reproduced in the simulations in a satisfactory way.
- Simulations with varying computational grid size led to satisfying results, demonstrating that the implemented grid size treatment shows good performance on a broad scale range.

Bibliography

[1] Nuclear Energy Agency. Flame Acceleration and Deflagration to Detonation Transition in Nuclear Industry. State of the Art Report 7, OECD NEA/CSNI, 2000.

[2] Nuclear Energy Agency and Committee on the Safety of Nuclear Installations. ISP-49 on Hydrogen Combustion. Technical Report R(2011)9, OECD NEA/CSNI, 2012.

[3] C. Altantzis, C.E. Frouzakis, A.G. Tomboulides, S.G. Kerkemeier, and K. Boulouchos. Detailed numerical simulations of intrinsically unstable two-dimensional planar lean premixed hydrogen/air flames. *Proceedings of the Combustion Institute*, 33(1): 1261–1268, 2011.

[4] A. Amato, M. Day, R.K. Cheng, J. Bell, and T. Lieuwen. Leading edge statistics of turbulent, lean, H2-air flames. *Proceedings of the Combustion Institute*, 35(2):1313 – 1320, 2015.

[5] ANSYS Inc. ANSYS CFX, 2014. Version 15.0.7.

[6] C.R.L. Bauwens, J.M. Bergthorson, and S.B. Dorofeev. Experimental investigation of spherical-flame acceleration in lean hydrogen-air mixtures. *International Journal of Hydrogen Energy*, 42(11):7691 – 7697, 2017. Special issue on The 6th International Conference on Hydrogen Safety (ICHS 2015), 2015, Yokohama, Japan.

[7] R. Beauvais, F. Mayinger, and G. Strube. Turbulent Flame Acceleration - Mechanisms and Significance for Safety considerations. *International Journal of Hydrogen Energy*, 19(8):701 – 708, 1994.

[8] J.K. Bechtold and M. Matalon. Hydrodynamic and diffusion effects on the stability of spherically expanding flames. *Combustion and Flame*, 67(1):77 – 90, 1987.

[9] J.K. Bechtold and M. Matalon. The Dependence of the Markstein Length on Stoichiometry. *Combustion and Flame*, 127(1-2):1906–1913, 2001.

[10] R.J. Blint. The relationship of the laminar flame width to flame speed. *Combustion Science and Technology*, 49(1-2):79–92, 1986.

[11] L.R. Boeck. *Deflagration-to-Detonation Transition and Detonation Propagation in H2-Air Mixtures with Transverse Concentration Gradients*. PhD Thesis, Technische Universität München, Garching, 2015.

[12] L.R. Boeck, P. Katzy, J. Hasslberger, A. Kink, and T. Sattelmayer. The GraVent DDT database. *Shock Waves*, 26(5):683–685, 2016.

[13] L.R. Boeck, R. Mevel, T. Fiala, J. Hasslberger, and T. Sattelmayer. High-speed OH-PLIF imaging of deflagration-to-detonation transition in H2-air mixtures. *Experiments in Fluids*, 57(6), 2016.

[14] R. Borghi. *On the Structure and Morphology of Turbulent Premixed Flames*, pages 117–138. Springer US, Boston, MA, 1985.

[15] R. Borghi. Turbulent combustion modeling. *Progress in Energy and Combustion Science*, 14(1):245 – 292, 1988.

[16] D. Bradley. Instabilities and flame speeds in large-scale premixed gaseous explosions. *Philosophical Transactions of the Royal Society of London A*, 357:3567–3581, 1999.

[17] D. Bradley, A.K.C. Lau, and M. Lawes. Flame Stretch Rate as a Determinant of Turbulent Burning Velocity. *Philosophical Transactions: Physical Sciences and Engineering*, 338(1650):359–387, 1992.

[18] D. Bradley, R.A. Hicks, M. Lawes, C.G.W. Sheppard, and R. Woolley. The Measurement of Laminar Burning Velocities and Markstein Numbers for Iso-octane-Air and Iso-octane-n-Heptane-Air

Mixtures at Elevated Temperatures and Pressures in an Explosion Bomb. *Combustion and Flame*, 115(1-2):126–144, 1998.

[19] D. Bradley, C.G.W. Sheppard, R. Woolley, D.A. Greenhalgh, and R.D. Lockett. The Development and Structure of Flame Instabilities and Cellularity at Low Markstein Numbers in Explosions. *Combustion and Flame*, 122(1-2):195–209, 2000.

[20] W. Breitung. *Hydrogen Technology - Chapter 9: Safety Analysis of Hydrogen Vehicles and Infrastructure*. Springer, Berlin, 1999.

[21] W. Breitung, C.K. Chan, S. Dorofeev, A. Eder, B.E. Gelfand, M. Heitsch, R. Klein, A. Malliakos, J.E. Shepherd, E. Studer, et al. Flame acceleration and deflagration-to-detonation transition in nuclear safety. *State-of-the-Art Report by a Group of Experts, OECD Nuclear Energy Agency, NEA/CSNI/R(2000)7*, 2000.

[22] M.P. Burke, Z. Chen, Y. Ju, and F.L. Dryer. Effect of cylindrical confinement on the determination of laminar flame speeds using outwardly propagating flames. *Combustion and Flame*, 156(4):771 – 779, 2009.

[23] D. Chapman. On the rate of explosion in gases. *Philosophical Magazine*, 47:90–104, 1899.

[24] Z. Chen. On the extraction of laminar flame speed and Markstein length from outwardly propagating spherical flame. *Combustion and Flame*, 158(2):291–300, 2011.

[25] G. Ciccarelli and S. Dorofeev. Flame acceleration and transition to detonation in ducts. *Progress in Energy and Combustion Science*, 34(4):499–550, 2008.

[26] P. Clavin. Dynamic behavior of premixed flame fronts in laminar and turbulent flows. *Progress in Energy and Combustion Science*, 11(1):1–58, 1985.

[27] P. Clavin and G. Joulin. Flamelet library for turbulent wrinkled flames. *Lecture Notes in Engineering: Turbulent Reactive Flows*, 40: 213 – 239, 1989.

[28] Damköhler, G. Der Einfluss der Turbulenz auf die Flammengeschwindigkeit in Gasgemischen. *Zeitschrift für Elektrochemie und angewandte physikalische Chemie*, 46:601–652, 1940.

[29] F. Dinkelacker and S. Hölzler. Investigation of a Turbulent Flame Speed Closure Approach for Premixed Flame Calculations. *Combustion Science and Technology*, 158(1):321–340, 2000.

[30] F. Dinkelacker, B. Manickam, and S.P.R. Muppala. Modelling and simulation of lean premixed turbulent methane/hydrogen/air flames with an effective Lewis number approach. *Combustion and Flame*, 158(9):1742–1749, 2011.

[31] G. Dixon-Lewis. Kinetic mechanism, structure and properties of premixed flames in hydrogen-oxygen-nitrogen mixtures. *Philosophical Transactions of the Royal Society of London A*, 292:45–49, 1979.

[32] S.B. Dorofeev. Flame Acceleration and Explosion Safety Applications. *Proceedings of the Combustion Institute*, 33:2161–2175, 2011.

[33] S.B. Dorofeev, V. Sidorov, M. Kuznetsov, I. Matsukov, and V. Alekseev. Effect of scale on the onset of detonations. *Shock Waves*, 10: 137–149, 2000.

[34] S.B. Dorofeev, M. Kuznetsov, V. Alekseev, A. Efimenko, and W. Breitung. Evaluation of limits for effective flame acceleration in hydrogen mixtures. *Journal of Loss Prevention in the Process Industries*, 14(6):583–589, 2001.

[35] D.R. Dowdy, D. B. Smith, S.C. Taylor, and A. Williams. The use of expanding spherical flames to determine burning velocities and stretch effects in hydrogen/air mixtures. *Proceedings of the Combustion Institute*, 23:325–332, 1991.

[36] P. Drinovac. *Experimentelle Untersuchungen zu katalytischen Wasserstoffrekombinatoren für Leichtwasserreaktoren*. PhD Thesis, Rheinisch-Westfälische Technische Hochschule Aachen, Aachen, 2006.

[37] J.F. Driscoll. Turbulent premixed combustion: Flamelet structure and its effect on turbulent burning velocities. *Progress in Energy and Combustion Science*, 34(1):91–134, 2008.

[38] P. Druck. *Untersuchung magerer H2-Luft Flammen in geschlossenen Geometrien mittels experimenteller Methoden und CFD Simulationen auf unteraufgelösten Rechengittern.* Master Thesis, Technische Universität München, Garching, 2017.

[39] J.H. Ferziger and M. Perić. *Computational Methods for Fluid Dynamics.* Springer, Berlin, 1999.

[40] K. Finke. *Entwicklung und Validierung eines MATLAB-Algorithmus zur Darstellung der Flammenfront aus OH-PLIF- und PIV-Aufnahmen einer turbulenten, vorgemischten Wasserstoffflamme.* Diploma Thesis, Technische Universität München, Garching, 2015.

[41] A. Friedrich, J. Grune, G. Necker, K. Sempert, G. Stern, A. Veser, M. Kuznetsov, A. Kotchourko, W. Breitung, and T. Jordan. Kriterien für Flammenbeschleunigung und Detonationsübergang in Wasserstoff-Luft-Gemischen mit Konzentrationsgradienten und partiellem Einschluss, GRS-Abschlussbericht Vorhaben Nr. 1501346. Technical report, Pro-Science GmbH, Karlsruher Institut für Technologie, 2011.

[42] C.E. Frouzakis, N. Fogla, A.G. Tomboulides, C. Altantzis, and M. Matalon. Numerical study of unstable hydrogen/air flames: Shape and propagation speed. *Proceedings of the Combustion Institute*, 35(1):1087–1095, 2015.

[43] Gesellschaft für Reaktorsicherheit (GRS). Deutsche Risikostudie Kernkraftwerke Phase B - Eine zusammenfassende Darstellung. Technischer Bericht GRS-72, GRS, 1989.

[44] B.E. Gelfand, L.V. Silnikov, S.P. Medvedev, and S.V. Khomik. *Thermo-Gas Dynamics of Hydrogen Combustion and Explosion.* Springer, Berlin, Heidelberg, 2012.

[45] P. Gerlinger. *Numerische Verbrennungssimulation: effiziente numerische Simulation turbulenter Verbrennung.* Springer, Berlin; Heidelberg; New York, 2005.

[46] D.G. Goodwin, H.K. Moffat, and R.L. Speth. Cantera: An object-oriented software toolkit for chemical kinetics, thermodynamics, and transport processes. `http://www.cantera.org`, 2016. Version 2.2.1.

[47] Y.A. Gostintsev, A.G. Istratov, and Yu.V. Shulenin. Self-similar propagation of a free turbulent flame in mixed gas mixtures. *Combustion, Explosion and Shock Waves*, 24(5):563–569, 1988.

[48] X.J. Gu, M Z. Haq, M. Lawes, and R. Woolley. Laminar Burning Velocity and Markstein Lengths of Methane-Air Mixtures. *Combustion and Flame*, 121(1-2):41–58, 2000.

[49] F. Halter, C. Chauveau, N. Djebaili-Chaumeix, and I. Gökalp. Characterization of the effects of pressure and hydrogen concentration on laminar burning velocities of methane-hydrogen-air mixtures. *Proceedings of the Combustion Institute*, 30(1):201 – 208, 2005.

[50] M.Z. Haq, C.G.W. Sheppard, R. Woolley, D.A. Greenhalgh, and R.D. Lockett. Wrinkling and Curvature of Laminar and Turbulent Premixed Flames. *Combustion and Flame*, 131(1-2):1–15, 2002.

[51] J. Hasslberger. *Numerical Simulation of Deflagration-to-Detonation Transition on Industry Scale*. PhD Thesis, Technische Universität München, Garching, 2017.

[52] J. Hasslberger, P. Katzy, and T. Sattelmayer. On the effect of pressure on intrinsic flame instabilities in lean hydrogen-air mixtures - Part I: Detailed chemistry based direct numerical simulation. In *26th International Colloquium on the Dynamics of Explosions and Reactive Systems (ICDERS)*, Boston, MA, USA, 2017.

[53] E.R. Hawkes, R. Sankaran, and J.H. Chen. Estimates of the three-dimensional flame surface density and every term in its transport equation from two-dimensional measurements. *Proceedings of the Combustion Institute*, 33(1):1447–1454, 2011.

[54] V. Hoferichter, C. Hirsch, and T. Sattelmayer. Analytic prediction of unconfined boundary layer flashback limits in premixed

hydrogen-air flames. *Combustion Theory and Modelling*, 21(3): 382–418, 2017.

[55] International Atomic Energy Agency. `https://www.iaea.org/PRIS/WorldStatistics/OperationalReactorsByType.aspx`, 2016.

[56] E.D. Jouguet. Sur la propagation des reactions chimiques dans les gaz. *Journal de Mathematiques Pures et Appliquees*, 1:347–425, 1905.

[57] T. Kathrotia, M. Fikri, M. Bozkurt, M. Hartmann, U. Riedel, and C. Schulz. Study of the H+O+M reaction forming OH*: Kinetics of OH* chemiluminescence in hydrogen combustion systems. *Combustion and Flame*, 157(7):1261–1273, 2010.

[58] P. Katzy, L.R. Boeck, J. Hasslberger, and T. Sattelmayer. Application of High-Speed OH-PLIF Technique for Improvement of Lean Hydrogen-Air Combustion Modeling. In *International Conference on Nuclear Engineering (ICONE)*, Charlotte, NC, USA, 2016.

[59] P. Katzy, J. Hasslberger, L.R. Boeck, and T. Sattelmayer. The Effect of Intrinsic Instabilities on Effective Flame Speeds in Under-Resolved Simulations of Lean Hydrogen-Air Flames. *Journal of Nuclear Engineering and Radiation Science*, 3(4):041015, 2017.

[60] P. Katzy, J. Hasslberger, and T. Sattelmayer. On the effect of pressure on intrinsic flame instabilities in lean hydrogen-air mixtures - Part II: Experimental investigation based on OH-PLIF technique. In *26th International Colloquium on the Dynamics of Explosions and Reactive Systems (ICDERS)*, Boston, MA, USA, 2017.

[61] R. Keppeler and M. Pfitzner. Modelling of Landau-Darrieus and thermo-diffusive instability effects for CFD simulations of laminar and turbulent premixed combustion. *Combustion Theory and Modelling*, 19(1):1–28, 2015.

[62] R. Klein, W. Breitung, I. Coe, L. He, H. Olivier, W. Rehm, and E. Studer. Models and criteria for prediction of deflagration-to-detonation transition (DDT) in hydrogen-air-steam systems under

severe accident conditions. Technical Report, Forschungszentrum Jülich, 2000.

[63] K. Kohse-Höinghaus and J.B. Jeffries. *Applied Combustion Diagnostics*. Taylor & Francis, New York, 2002.

[64] A.N. Kolmogorov. The Local Structure of Turbulence in Incompressible Viscous Fluid for Very Large Reynolds Numbers. *Proceedings of the Royal Society of London A*, 434:9 – 13, 1991.

[65] A.A. Konnov. Remaining uncertainities in the kinetic mechanism of hydrogen combustion. *Combustion and Flame*, 152(4):507–528, 2008.

[66] M. S. Kuznetsov, J. Grune, A. Friedrich, K. Sempert, W. Breitung, and T. Jordan. Hydrogen-air deflagrations and detonations in a semi-confined flat layer. *Proceedings of the Sixth International Seminar on Fire and Explosion Hazards*, Leeds, UK, 2010.

[67] O.C. Kwon and G.M. Faeth. Flame/stretch interactions of premixed hydrogen-fueled flames: measurements and predictions. *Combustion and Flame*, 124(4):590–610, 2001.

[68] L.D. Landau. On the Theory of Slow Combustion. *Acta Physicochimica URSS*, 19:77–85, 1944.

[69] C.K. Law and C.J. Sung. Structure, aerodynamics and geometry of premixed flamelets. *Progress in Energy and Combustion Science*, 26 (4-6):459–505, 2000.

[70] J.H.S. Lee. *The Detonation Phenomenon*. Cambridge University Press, 2008. ISBN 9781139473200.

[71] T.W. Lee and S.J. Lee. Direct comparison of turbulent burning velocity and flame surface properties in turbulent premixed flames. *Combustion and Flame*, 132(3):492–502, 2003.

[72] T.W. Lee, G.L. North, and D.A. Santavicca. Curvature and Orientation Statistics of Turbulent Premixed Flame Fronts. *Combustion Science and Technology*, 84(1-6):121–132, 1992.

[73] T.W. Lee, G.L. North, and D.A. Santavicca. Surface properties of turbulent premixed propane/air flames at various Lewis numbers. *Combustion and Flame*, 93(4):445 – 456, 1993.

[74] B. Lewis and G. von Elbe. Combustion, Flames and Explosion of Gases. Academic Press, New York, 1987.

[75] A.N. Lipatnikov. *Fundamentals of Premixed Turbulent Combustion*. CRC Press, Taylor & Francis Group, 2013.

[76] A.N. Lipatnikov and J. Chomiak. Turbulent flame speed and thickness: phenomenology, evaluation, and application in multi-dimensional simulations. *Progress in Energy and Combustion Science*, 28(1):1–74, 2002.

[77] A.N. Lipatnikov and J. Chomiak. Molecular transport effects on turbulent flame propagation and structure. *Progress in Energy and Combustion Science*, 31(1):1 – 73, 2005.

[78] F. Liu, X. Bao, J. Gu, and R. Chen. Onset of cellular instabilities in spherically propagating hydrogen-air premixed laminar flames. *International Journal of Hydrogen Energy*, 37(15):11458–11465, 2012.

[79] G.H. Markstein, North Atlantic Treaty Organization. Advisory Group for Aeronautical Research, and Development. *Nonsteady flame propagation*. Agardograph Series. Published for and on behalf of Advisory Group for Aeronautical Research and Development, North Atlantic Treaty Organization by Pergamon Press, 1964.

[80] A. Marshall, J. Lundrigan, P. Venkateswaran, J. Seitzman, and T. Lieuwen. Fuel effects on leading point curvature statistics of high hydrogen content fuels. *Proceedings of the Combustion Institute*, 35(2):1417 – 1424, 2015.

[81] E. Mason and T. Marrero. Gaseous Diffusion Coefficients. *Journal of Physical and Chemical Reference Data*, 1(1):3–117, 1972.

[82] M. Metghalchi and J.C. Keck. Burning velocities of mixtures of air with methanol, isooctane, and indolene at high pressure and temperature. *Combustion and Flame*, 48:191 – 210, 1982.

[83] V.V. Molkov, D.V. Makarov, and H. Schneider. Hydrogen-air deflagrations in open atmosphere: Large eddy simulation analysis of experimental data. *International Journal of Hydrogen Energy*, 32(13): 2198 – 2205, 2007.

[84] M. Ó Conaire, H.J. Curran, J.M. Simmie, W.J. Pitz, and C.K. Westbrook. A comprehensive modeling study of hydrogen oxidation. *International Journal of Chemical Kinetics*, 36(11):603–622, 2004.

[85] C. Olm, I.G. Zselya, R. Palvölgyia, T. Vargaa, T. Nagya, H.J. Curranc, and T. Turanyia. Comparison of the performance of several recent hydrogen combustion mechanisms. *Combustion and Flame*, 161 (9):2219–2234, 2014.

[86] N. Peters. Turbulente Brenngeschwindigkeit - Abschlussbericht zum Forschungsvorhaben Pe 241/9-2. Technical Report, 1994.

[87] N. Peters. The turbulent burning velocity for large-scale and small-scale turbulence. *Journal of Fluid Mechanics*, 384:107–132, 1999.

[88] N. Peters. *Turbulent Combustion*. Cambridge Monographs on Mechanics. Cambridge University Press, 2000.

[89] T. Poinsot and D. Veynante. *Theoretical and Numerical Combustion*. RT Edwards, Inc., 2005.

[90] B.E. Poling, J.M. Prausnitz, J.P. O'connell, et al. *The properties of gases and liquids*, volume 5. McGraw-Hill New York, 2001.

[91] S. Pope. *Turbulent Flows*. Camebridge University Press, 2000.

[92] B. Renou, A. Boukhalfa, D. Puechberty, and M. Trinite. Effects of stretch on the local structure of preely propagating premixed low-turbulent flames with various lewis numbers. *Symposium (International) on Combustion*, 27(1):841 – 847, 1998.

[93] B. Renou, A. Boukhalfa, D. Puechberty, and M. Trinite. Local scalar flame properties of freely propagating premixed turbulent flames at various lewis numbers. *Combustion and Flame*, 123(4):507 – 521, 2000.

[94] O. Reynolds. On the dynamical theory of incompressible viscous fluids and the determination of the criterion. *Philosophical Transactions of the Royal Society of London A*, 186:123–164, 1895.

[95] G.D. Roy, S. Frolov, and A. Starik. *Nonequilibrium Phenomena: Plasma, Combustion, Atmosphere*. 2009.

[96] A. Savitzky and M.J.E. Golay. Smoothing and Differentiation of Data by Simplified Least Squares Procedures. *Analytical Chemistry*, 36(8):1627–1639, 1964.

[97] S. Sazhin, E. Sazhina, O. Faltsi-Saravelou, and P. Wild. The P1-model for themal radiation transfer: advantages and limitations. *Fuel*, 75(3):289–294, 1996.

[98] B. Schramm, J. Stewering, and M. Sonnenkalb. Erprobung und Validierung von CFD-Codes für die Simulation von unfalltypischen Phänomenen im Sicherheitseinschluss. Technical Report RS1500, GRS, 2013.

[99] B. Schramm, J. Stewering, and M. Sonnenkalb. Einsatz von CFD-Codes für die Simulation von unfalltypischen Phänomenen im Sicherheitseinschluss: Validierung und gezielte Modellerweiterung. Technical Report, GRS, 2017.

[100] Sirah Lasertechnik. Datasheet Credo Dye, 2015.

[101] T.N. Srinivasan and T.S. Gopi Rethinaraj. Fukushima and Thereafter: Reassessment of Risks of Nuclear Power. *Energy Policy*, 52: 726–736, 2013.

[102] C.J. Sun, C.J. Sung, L. He, and C.K. Law. Dynamics of weakly stretched flames: Quantitative description and extraction of global flame parameters. *Combustion and Flame*, 118(1-2):108–128, 1999.

[103] S.C. Taylor. *Burning Velocity and the Influence of Flame Stretch*. PhD Thesis, University of Leeds, 1991.

[104] I.C. Tolias, A.G. Venetsanos, N. Markatos, and C.T. Kiranoudis. CFD modeling of hydrogen deflagration in a tunnel. *International Journal of Hydrogen Energy*, 39(35):20538 – 20546, 2014.

[105] I.C. Tolias, A.G. Venetsanos, N. Markatos, and C.T. Kiranoudis. CFD evaluation against a large scale unconfined hydrogen deflagration. *International Journal of Hydrogen Energy*, 42(11):7731 – 7739, 2017. Special issue on The 6th International Conference on Hydrogen Safety (ICHS 2015), 2015, Yokohama, Japan.

[106] S.D. Tse, D.L. Zhu, and C.K. Law. Morphology and Burning rates of Expanding Spherical Flames in H2 /O2/Inert Mixtures up to 60 Atmospheres. *Proceedings of the Combustion Institute*, 28:1793–1800, 2000.

[107] S.R. Turns. *An Introduction to Combustion*. McGraw-Hill, New York, 2011.

[108] C.M. Vagelopoulos, F.N. Egolfopoulos, and C.K. Law. Further Considerations on the Determination of Laminar Flame Speeds with the Counterflow Twin-Flame Technique. *Proceedings of the Combustion Institute*, 25:1341–1347, 1994.

[109] A. Velikorodny, E. Studer, S. Kudriakov, and A. Beccantini. Combustion modeling in large scale volumes using EUROPLEXUS code. *Journal of Loss Prevention in the Process Industries*, 35:104–116, 2015.

[110] K. Vollmer. *Einfluss von Mischungsgradienten auf die Flammenbeschleunigung und die Detonation in Kanälen*. PhD Thesis, Technische Universität München, Garching, 2015.

[111] J. Warnatz, U. Maas, and R.W. Dibble. *Verbrennung*. Springer, Berlin, Heidelberg, New York, 2001.

[112] H.G. Weller, G. Tabor, H. Jasak, and C. Fureby. A tensorial approach to computational continuum mechanics using object-oriented techniques. *Computers in Physics*, 12(6):620–631, 1998.

[113] F.M. White and I. Corfield. *Viscous fluid flow*, volume 3. McGraw-Hill Higher Education Boston, 2006.

[114] C.K. Wu and C.K. Law. On the Determination of Laminar Flame Speeds from Stretched Flames. *Proceedings of the Combustion Institute*, 20:1941–1949, 1985.

[115] H. Xiao, D. Makarov, J. Sun, and V. Molkov. Experimental and numerical investigation of premixed flame propagation with distorted tulip shape in a closed duct. *Combustion and Flame*, 159(4): 1523 – 1538, 2012.

[116] V. Yakhot. Propagation Velocity of Premixed Turbulent Flames. *Combustion Science and Technology*, 60(1-3):191–214, 1988.

[117] IA.B. Zeldovich, G.I. Barenblatt, V.B. Librovich, and G.M. Makhviladze. *Mathematical theory of combustion and explosions*. Consultants Bureau, New York, 1985.

[118] V. Zimont, W. Polifke, M. Bettelini, and W. Weisenstein. An Efficient Computational Model for Premixed Turbulent Combustion at High Reynolds Numbers Based on a Turbulent Flame Speed Closure. *Transactions of the ASME*, 120:526–532, 1998.

[119] V.L. Zimont and A. Lipatnikov. A numerical model of premixed turbulent combustion of gases. *Chem. Phys. Reports*, 14(7):993–1025, 1995.